Dark matter

Giorgio Arcadi and Teresa Marrodán Undagoitia

Max-Planck-Institut für Kernphysik, Saupfercheckweg 1, 69117 Heidelberg, Germany

E-mail: giorgio.arcadi@mpi-hd.mpg.de and marrodan@mpi-hd.mpg.de

Abstract.

This document is a brief summary of the topics discussed during the the dark matter lecture held in the winter term of 2018 at the University of Heidelberg. The primary goal of the lecture is to review observational, theoretical and experimental developments related to the understanding of dark matter. The lectures cover some astrophysical and cosmological aspects which constrain the properties of dark matter. Other topics discussed are dark matter candidates including the Weakly Interacting Massive Particle (WIMP) but also axions or sterile neutrinos. Dark matter search strategies will be presented together with the discussion of the current results.

Contents

1 Dark matter indications **4**
- 1.1 Dispersion velocities of galaxies in clusters 4
- 1.2 Rotation curves 4
- 1.3 Gravitational lensing 4
- 1.4 Galaxy-cluster collisions 6
- 1.5 Large structure formation 6
- 1.6 Cosmic microwave background (CMB) 8

2 History of the Universe **10**
- 2.1 Basic concepts of the expanding Universe 10
- 2.2 Brief thermal history of the Universe 12

3 Explanations and particle candidates **13**
- 3.1 Explanations 13
  - 3.1.1 Modification of gravitational laws 13
  - 3.1.2 MACHOS and micro-lensing measurements 13
  - 3.1.3 Primordial black holes 14
- 3.2 Dark matter particle candidates 15
  - 3.2.1 Standard model particles and beyond 15
  - 3.2.2 WIMPs and their production mechanism 16
  - 3.2.3 WIMPs in Supersymmetry (SUSY) 17
  - 3.2.4 Superheavy WIMPs, Sterile neutrinos and axions 18

4 WIMP dark matter **19**
- 4.1 Thermodynamics of the Early Universe 19
- 4.2 Conditions for thermal equilibrium 19
- 4.3 Boltzmann's equation 20
- 4.4 WIMP solution of Boltzmann equation 20

5 Dark matter distribution **22**
- 5.1 Motivation 22
- 5.2 Objects of interest 23
- 5.3 Modelling dark matter halos 24
- 5.4 The standard halo model (SHM) 26

6 Direct detection **27**
- 6.1 Principles of direct detection 27
- 6.2 Backgrounds 32
- 6.3 Statistical treatment of data 35
- 6.4 Detector calibration 36
- 6.5 Experiments and results 37

7 WIMP models 44
7.1 General considerations . . . 44
7.2 Examples of realistic models . . . 45

8 Sterile Neutrinos as dark matter 48
8.1 Motivation . . . 48
8.2 Phenomenology of keV sterile neutrinos . . . 49

9 Axion dark matter 51
9.1 Motivation: the strong CP problem . . . 51
9.2 Production in the early Universe . . . 52
9.3 Axion couplings and axion-like particles . . . 53
9.4 Astrophysical constrains . . . 55
9.5 Axion search experiments . . . 55

10 Indirect detection 60
10.1 Locations of indirect signals . . . 60
10.2 Signal production . . . 60
10.3 Particle propagation and overview of technologies . . . 62
10.4 Detection of indirect signals . . . 63
10.4.1 Searches using neutrinos . . . 63
10.4.2 Gamma detection in Cherenkov telescopes . . . 64
10.4.3 Gamma detection by satellites . . . 66
10.4.4 X-rays signals . . . 67
10.4.5 Charged particles . . . 68

11 Dark matter searches at particle accelerators 71
11.1 Introduction . . . 71
11.2 Signatures and features . . . 71
11.3 Detection at colliders . . . 72
11.4 Searches at LEP . . . 72
11.5 Searches at LHC . . . 73
11.6 Comparison to direct/indirect detection results . . . 76

1. Dark matter indications

1.1. Dispersion velocities of galaxies in clusters

- Historically the first indication for dark matter
- Virial theorem: relation between kinetic and potential energy of a system by potential forces
- Derivation of Coma cluster mass following F. Zwicky paper (1933) [1].

1.2. Rotation curves

- Measurement of rotation velocity from the Doppler shift of the 21 cm hydrogen line
- Expectation: decreasing velocities for increasing distance to the galactic centre (outside the main visible mass distribution $\propto \sqrt{1/r}$)
- Measurement: rotation curves are approximately flat for large radii
- Early measurement in 1978 by V. Rubin [2] (see figure 1)

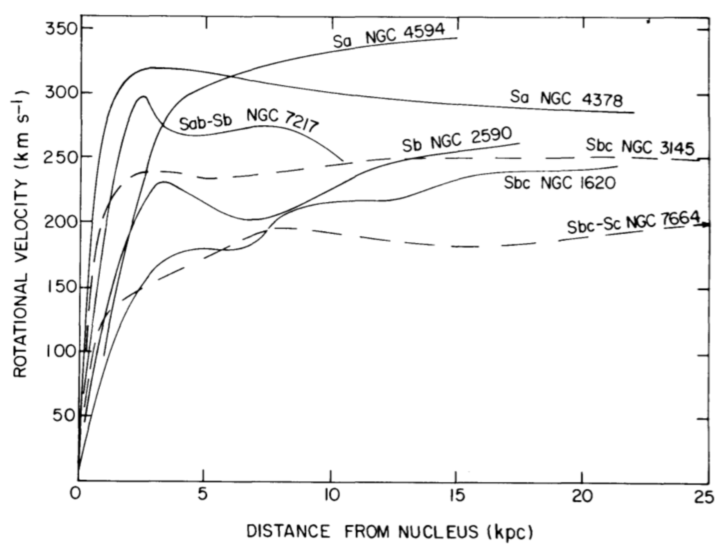

Figure 1. Examples of rotation curve measurements. Figure from V. Rubin *et al.*, 1978 [2].

1.3. Gravitational lensing

- Deflection of light by a massive object (the lens) as it travels from the source to the observer
- The analysis of the deflection patterns can be used to reconstruct the matter distribution of the lens
- Effect proposed by Einstein in 1936 [3]

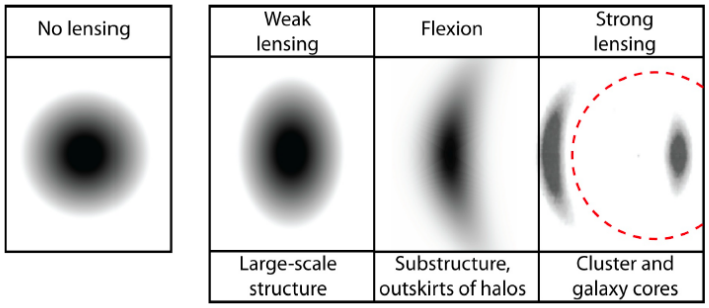

Figure 2. Gravitational lensing: various regimes of image distortion. A circular source is distorted into an ellipse by weak lensing being the typical resulting axis ratio $\sim 2\,\%$ (exaggerated for illustration). For most curved space-time (most massive objects), strong gravitational lensing produces multiple imaging and giant arcs. Figure from R. Massey *et al.* (2010), arXiv:1001.1739 [4].

- Types of lensing [4]: strong, flexion, weak and microlensing (see figure 2)
- Strong lensing appears for dense concentrations of mass. If the source is behind, Einstein rings appear, otherwise multiple images of the object, tangential around the lens, result (see figure 3 for observational examples)

Figure 3. (Left) Strong lensing: Einstein ring. Figure from ESA/Hubble & NASA. (Right) Weak lensing in Abell 2218. Figure from NASA.

- Weak lensing appears when the lines of sight pass through more extended objects. By analysing a large number of object behind the lens, a statistical analysis can be performed to extract a mass distribution map
- Flexion is an intermediate effect between strong and weak lensing
- Microlensing: small increase in observed luminosity when a small object crosses the line of sight of a star. Used to search for Jupiter-like objects, see also section 3.1.2

1.4. Galaxy-cluster collisions

- Galaxy clusters are composed by gas clouds, the stars in the constituent galaxies and dark matter
- Rare events: collision of galaxy clusters such (observable when the movement of the clusters is tangential to observers on Earth)
- X-ray measurements characterize the collision of the gas clouds which are the main visible-mass constituent of the galaxy cluster
- Telescopes measuring optical wavelengths determine the position of galaxies
- Weak gravitational lensing is used to determine the total mass distribution
- Few examples of such event are shown in figure 4, see also reference [5]. The reconstruction of the gravitational potential via lensing shows a displacement from the X-ray signal corresponding to the main visible mass.

.

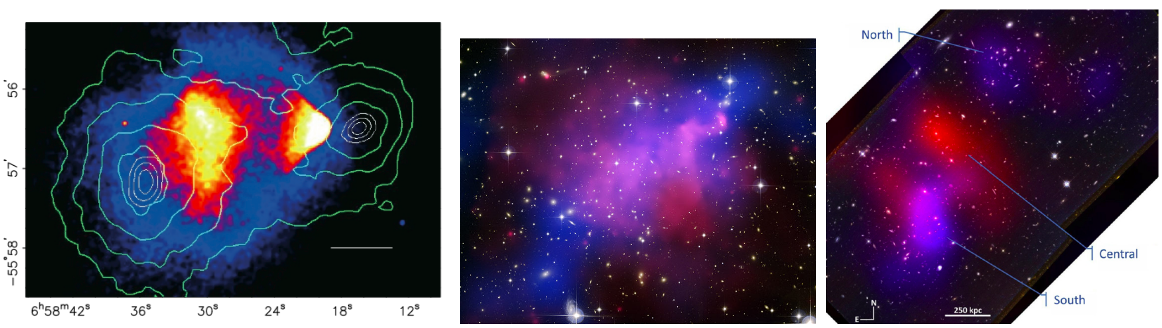

Figure 4. Galaxy-cluster collisions: bullet cluster, Abell 520 and DLSCL J0916.2+2951, respectively. Figures from astro-ph/0608407 [5], X-ray: NASA / CXC/ U. Victoria/ A. Mahdavi et al. and arXiv:1110.4391.

- Study of 72 cluster collisions [6] used to determine the average displacement of dark matter center to the baryonic matter centre, see figure 5
- Limits on the dark matter self-interaction can be placed [6]

1.5. Large structure formation

- Measurements of matter distribution from CMB maps, spectroscopic surveys, gravitational lensing and Lyman-α line of quasars
- Simulations provide the link from the distribution in the early Universe to the ones today, see figure 6 or an example from the Millennium simulation [7]
- Figure 6 shows dark matter on the left panels and the gas density (main visible matter constituent) on the right

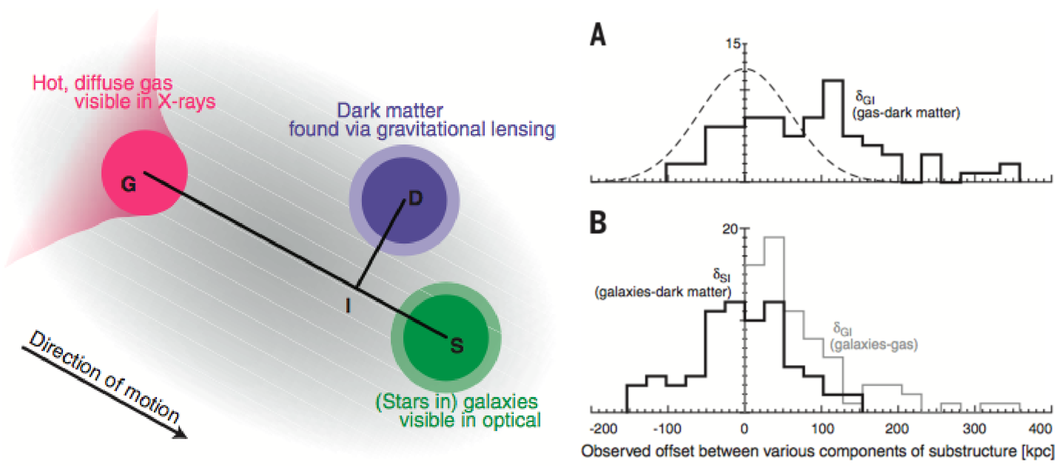

Figure 5. Galaxy-cluster collisions: (Right) Diagram of the displacement between gas (red), dark matter (blue) and the stars (green). (Left) Displacement results for 72 collisions. Figure from D. Harvey *et al.* Science 347 (2015) 1462, arXiv:1503.07675 [6].

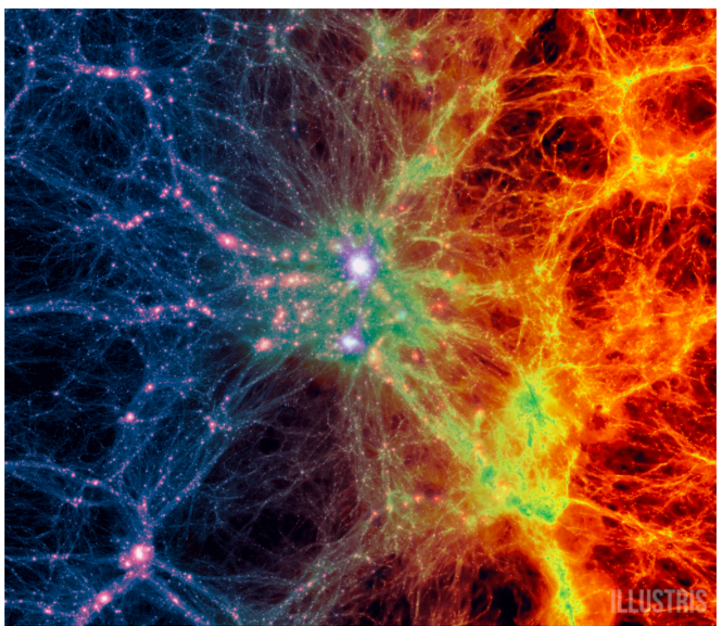

Figure 6. Large scale projection through the Illustris volume at z=0, centered on the most massive cluster, 15 Mpc/h deep. Shows dark matter density (left) transitioning to gas density (right). Figure from http://www.illustris-project.org.

- Spectroscopic galaxy survey data can be compared to simulations (see figure 7)
- Very good agreement between simulated distributions and measurements
- Dark matter is the seed to form the observed large structures in the Universe

- If dark matter is a particle and it is relativistic at the time of structure formations, the relative size of structures would be smeared out → dark matter can not be 'hot dark matter'

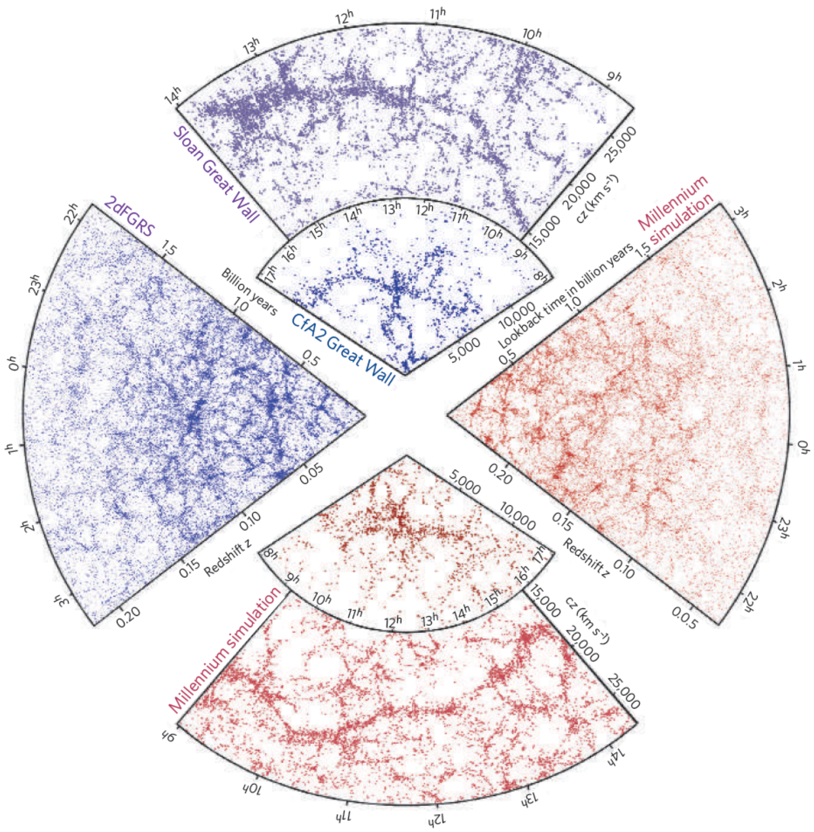

Figure 7. Comparison of clustering in observations of galaxy surveys (in blue) and in dark matter simulations (red). From Springel, Frenk & White, Nature **440** (2006) [7].

1.6. Cosmic microwave background (CMB)

- CMB: thermal photon radiation emitted at the end of recombination era
- Isotropic emission with a temperature of $T = 2.7\,\mathrm{K}$, predicted by Gamov ~ 1950
- First measurement by Penzias and Wilson, accidentally, in 1964 using horn antennas for telecommunications
- CMB anisotropies: fist measured by the COBE satellite in 1992. Also confirmed the black-body shape of the spectrum

- WMAP and Planck satellites measured the anisotropies ($10^{-5}\,\mathrm{K}$) in great detail. See figure 8 for a current map [8] (left) and the comparison of the resolutions (right)
- Most recent measurements by the Planck satellite operated from 2009 to 2013
- Two instruments (low and high frequency) to cover different frequency regions

- CMB power spectrum derived from the correlation of temperatures with respect to an angular scale
- Power spectrum as measured by Planck in figure 9

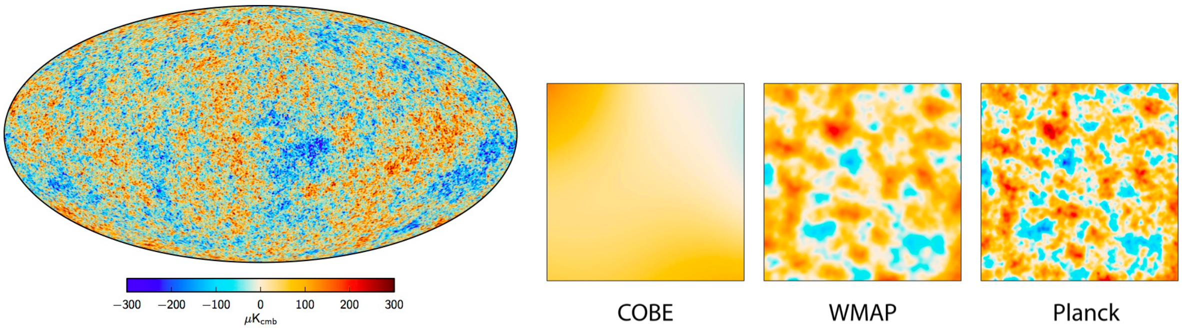

Figure 8. Cosmic microwave background maps. (left) Figure Planck Collaboration, arXiv:1507.02704 [8]. (Right) CMB resolution for different satellite measurements.

- Main spectral feature: ripples in the spectrum originating from baryon acoustic oscillations
- Position of the first peak determines the curvature of the Universe
- Other features in the spectrum are related to how photons were emitted and effects (like lensing) during the propagation
- Spectrum is fit with a 6 parameter model: ΛCDM (Λ cold dark matter) indicating that dark matter is a fundamental ingredient. The Λ refers to the cosmological constant necessary to explain the accelerated expansion of the Universe
- From CMB we know that 27% of the total energy content in the Universe is dark matter

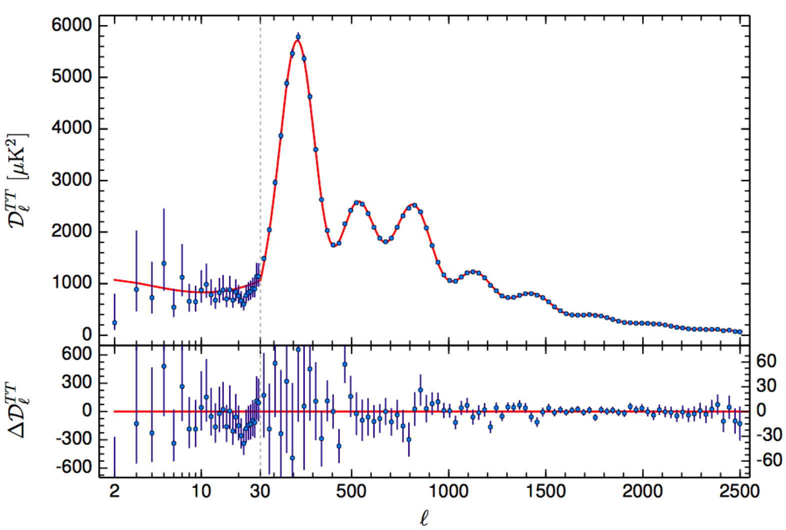

Figure 9. Temperature angular power spectrum of the primary CMB map by Planck. Figure Planck Collaboration, arXiv:1502.01589 [9].

A still qualitative but rather complete description of the spectrum of temperature fluctuations can be found in [10].

2. History of the Universe

2.1. Basic concepts of the expanding Universe

Observations:

- The Universe is homogeneous and isotropic at large distances.
- The Universe is expanding.

The evolution of the Universe is described by the Einstein's equation:

$$G_{\mu\nu} = 8\pi G T_{\mu\nu} + \Lambda g_{\mu\nu} \tag{1}$$

where G and Λ are, respectively, the Newton constant and the so-called cosmological constant. In view of the observations above the Einstein's equation is solved by adopting the following ansatz for the metric $g_{\mu\nu}$ and the Stress-Energy tensor $T_{\mu\nu}$:

$$ds^2 = g_{\mu\nu} dx^\mu dx^\nu = dt^2 - a(t)(dx^2 + dy^2 + dz^2) \tag{2}$$

$$T^{\mu\nu} = diag(\rho(t), -p(t), -p(t), -p(t)) \tag{3}$$

The metric is called Friedman-Robertson-Walker metric and a is called scale factor. The stress energy tensor describes a perfect fluid with energy density $\rho(t)$ and pressure $p(t)$. Energy and pressure are related by the so called equation of state:

$$p = \omega \rho \tag{4}$$

The conservation of the Stress-Energy, $\partial_\nu T^{\mu\nu} = 0$ gives:

$$d(\rho a^3) = -p d(a^3) \tag{5}$$

which combined with the equation of state:

$$\rho \propto a^{-3(1+\omega)} \tag{6}$$

Three main types of components enter in the stress energy tensor:

(i) **Radiation**, described by the equation of state $p = \frac{1}{3}\rho \to \rho \propto a^{-4}$;

(ii) **Matter**, described by the equation of state $p = 0 \to \rho \propto a^{-3}$;

(iii) The cosmological constant can be interpreted as a component of the energy tensor satisfying $p = -\rho \to \rho = \text{const}$. In many theories the Cosmological constant is replaced by a dynamical component, the so called Dark Energy.

From the 00 component of the Einstein's equation it is possible to write the so called Friedman's equation:

$$\left(\frac{1}{a}\frac{da}{dt}\right) = H^2 = \frac{8\pi G}{3}\left(\rho_R a^{-4} + \rho_M a^{-3} + \rho_\Lambda\right) \tag{7}$$

where H is the so called Hubble expansion parameter. Let's define then the so called critical density $\rho_c = \frac{3H^2}{8\pi G}$ and its present time value:

$$\rho_c^0 = \frac{3H_0^2}{8\pi G} = 5 \times 10^{-6}\,\mathrm{GeV}\,\mathrm{cm}^{-3} = 0.94 \times 10^{-29}\mathrm{g}\,\mathrm{cm}^3 \tag{8}$$

where H_0 is the present value of the Hubble expansion parameter which can be inferred from astronomical observations through the Hubble law:

$$v = H_0 d_p \tag{9}$$

Using the expressions above, we can normalize the equation for H as:

$$H^2 = H_0^2\left(\Omega_R a^{-4} + \Omega_M a^{-3} + \Omega_\Lambda\right) \tag{10}$$

At the time corresponding to the Big Bang $a = 0$ while, by convention one sets $a(t_0) = 1$ at the present time t_0. Observations tell that today the Universe is dominated by Ω_Λ. Because of the different scaling, it is straightforward to argue that going back in time the Universe undergo a phase a Matter domination and at even earlier times a phase of radiation domination.

Particles in the Early Universe are described by one particle distribution functions f which determine the probability distribution for the location and momenta of the particle. Because of homogeneity and isotropy $f = f(|\vec{p}|, t)$. In other words the distribution function depends only on the modulus of the three-momentum and on time.

The contribution from a given particle species to the components of $T^{\mu\nu}$ is represented by suitable integrals of its distribution function:

$$n = \frac{g}{(2\pi)^3}\int d^3p f(|\vec{p}|, t); \tag{11}$$

$$\rho = \frac{g}{(2\pi)^3}\int d^3 E p f(|\vec{p}|, t); \tag{12}$$

$$p = \frac{g}{(2\pi)^3}\int d^3p \frac{|\vec{p}|^2}{3E} f(|\vec{p}|, t); \tag{13}$$

where we have also defined the number density n. In the equations above $E = \sqrt{p^2 + m^2}$ while g are the internals degree of freedom (e.g. color number, particle-antiparticle number).

The ensemble of SM particles is, in the Early Universe, in thermal equilibrium. This means that the generic process:

$$a + b \leftrightarrow c + d \tag{14}$$

occurs in both directions with the same probability. In such a case the distribution function is known and it is:

$$f = \left[\exp\left(\frac{E - \mu}{T}\right) \pm 1\right]^{-1} \tag{15}$$

where (+) stands for the Fermi-Dirac distribution, which describes fermions, while (-) stands for Bose-Einstein distribution, which describes bosons. μ is the so called chemical potential. For the present discussion it can be assumed to be negligible. We distinguish two main cases:

(i) **Relativistic regime**: $m \ll T$. In such a case the integrals of the distribution functions give:

$$\rho = \begin{cases} \frac{\pi^2}{30} g T^4 & \text{Bose-Einstein} \\ \frac{7}{8}\frac{\pi^2}{30} g T^4 & \text{Fermi-Dirac} \end{cases} \tag{16}$$

$$\rho = \begin{cases} \frac{\xi(3)}{\pi} g T^3 & \text{Bose-Einstein} \\ \frac{3}{4}\frac{\xi(3)}{\pi^2} g T^3 & \text{Fermi-Dirac} \end{cases} \tag{17}$$

$$p = \frac{\rho}{3} \tag{18}$$

Relativistic species contribute as radiation to the Hubble expansion rate.

(ii) **Non relativistic regime**: $m \gg T$

$$n = g\left(\frac{mT}{2\pi}\right)^{3/2} \exp\left(-\frac{m}{T}\right) \tag{19}$$

$$\rho = mn \tag{20}$$

$$p = nT \ll \rho \tag{21}$$

Non relativistic species contribute as matter to the Hubble expansion rate.

In most of the particle scenarios DM is produced while the Universe is radiation dominated. In such a case the Hubble expansion parameter can be simply written as:

$$H^2 = \frac{8\pi G}{3}\frac{\pi^2}{30} g_{*\rho}(T) T^4 \tag{22}$$

where:

$$g_{*\rho} = \sum_{\text{bosons}} g_i + \frac{7}{8}\sum_{\text{fermions}} g_i \tag{23}$$

with the sum comprising all the species for which $m_i \ll T$ at a given T.

Determining the Dark Matter relic density means determining the unknown distribution function, $f_{\rm DM}$, of the Dark Matter and from it its energy and number density from which obtain the parameter $\Omega_{\rm DM}$. The theoretical prediction for $\Omega_{\rm DM}$ is then compared with the experimental determination from CMB measurements as performed, for example, by the PLANCK experiment.

2.2. Brief thermal history of the Universe

- $T = T_{\rm rh}$: After inflation the Universe thermalizes and starts the radiation domination era from the temperature $T_{\rm rh}$. Its value can be between order of the Planck scale ($\sim 10^{19}$ GeV) and few MeV.

- $T = 140\,\mathrm{GeV}$: EW phase transition.
- $T = 150\,\mathrm{MeV}$: QCD phase transition. Above this temperature the primordial thermal is composed by free quarks and gluons, below this temperature we have hadrons and mesons.
- $T \sim 5\,\mathrm{MeV}$: neutrinos decouple from the primordial thermal bath.
- $T \sim 1\,\mathrm{MeV}\,[t \sim 10^{-2} - 10^{2}\,\mathrm{s}]$: Big Bang Nucleosynthesis: free protons and neutrons combine to form light nuclei.
- $T \sim 0.1\,\mathrm{eV}[t \sim 10^{13}\,\mathrm{s}]$: CMB time. The Universe becomes transparent to photons. The photons emitted at this time are now observed as CMB.

3. Explanations and particle candidates

In this lecture, possible explanation to the various indications for dark matter discussed in the past lectures are presented. These include elementary particle candidates that will be discussed in deeper detail in future lectures.

3.1. Explanations

3.1.1. Modification of gravitational laws

- Modification of gravitational laws was proposed for the first time in 1983 (MOND [11]) to explain rotation curves (phenomenological approach)
- With this observation the rotation curve becomes asymptotically flat
- Observational support: Tully-Fisher correlation
- Fits of the MOND model to rotation curves data with only one free parameter (figure 10 (left))
- Problems: no explanation for lensing, cluster collision, CMB or structure formation
- Relativistic extension TeVeS [12]. Explains lensing but not structure formation and CMB description is not very satisfactory

3.1.2. MACHOS and micro-lensing measurements

- MACHOS (MAssive Compact Halo Objects): objects that produce very little to no light like. Examples for such objects would be black-holes, neutron stars, brown dwarfs ..
- Microlensing technique suggested by Paczynski in 1986 [14]: the observed brightness of an object increases when a MACHO is aligned with the observed object, i.e. on its line of sight
- A detection of an object using microlensing is a rare phenomena, surveys monitor typically $O(10^7)$ stars

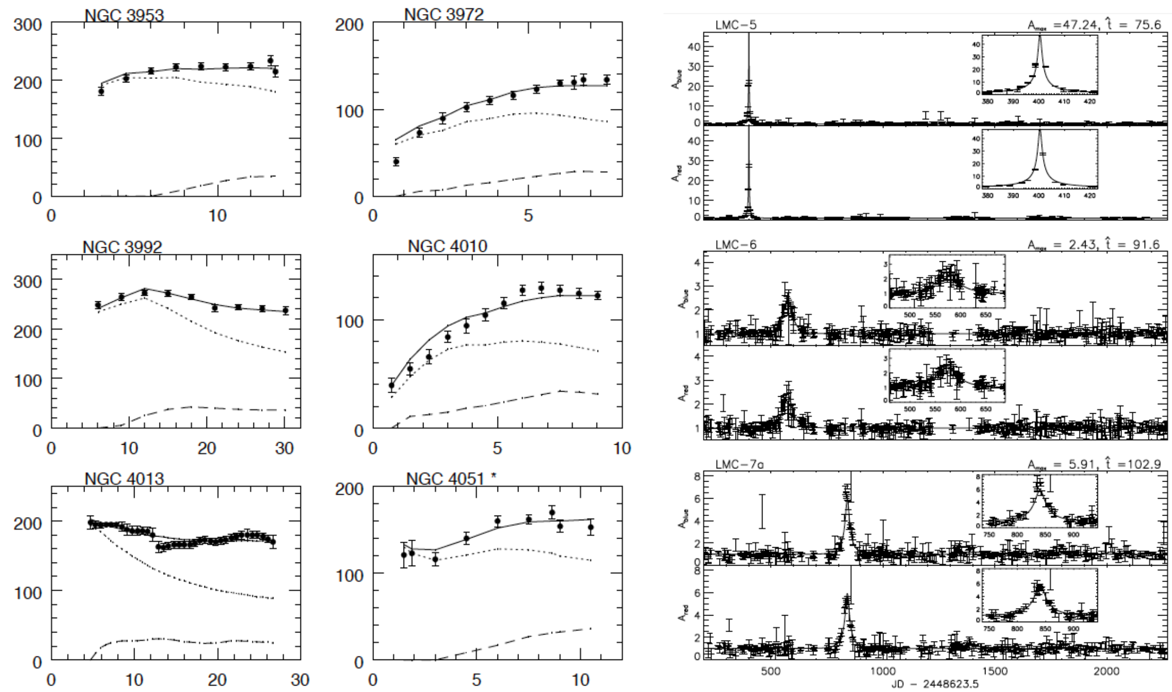

Figure 10. (Left) Fits of the MOND model (continuous line) to rotation curves data in Ursa Major galaxies. The dashed line represents the luminous disk and the dotted line the gaseous disk. Figure from Sanders & Verheijen, ApJ 503 (1998) 97. (Right) Examples of microlensing observations in the Large Magellanic Cloud. From C. Alcock *et al.* [MACHO Collaboration] Astrop. J. 542 (2000) 281 [13].

- The MACHO collaboration observed 12 million stars belonging to the Large Magellanic Cloud and detected $(13 - 17)$ microlensing events. Few examples from [13] can be seen in figure 10 (right)
- A 100% MACHO-composition of the Milky Way's dark matter content is ruled out at 95% C.L. [13]
- Big Bang nucleosynthesis (BBN) showed afterwards that dark matter cannot be baryonic excluding this hypothesis. This was learned by comparing the baryon density obtained from the BBN measurements (abundance of elements) and the one obtained by CMB

3.1.3. Primordial black holes

- Hypothetical black holes formed soon after the Big Bang [15]
- As they were formed before BBN, they behave as if they would be non-baryonic and constrains do not apply
- Formation: from the collapse of large over-densities in the early Universe
- Several constrains (see figure 11) on the fraction of mass that can be made up of black holes: evaporation, lensing, dynamical effects, CMB ...

- Most models predict that black holes are produced with some extended mass function (Not all PBH would have the same mass)

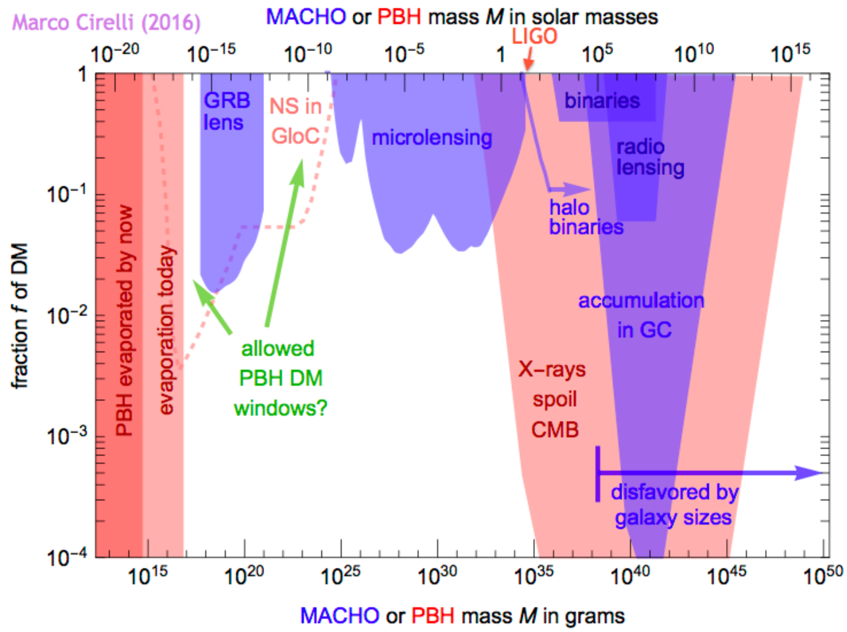

Figure 11. Constrains from different studies on the fraction of dark matter that is made up of black holes as a function of the black hole mass. Figure from M. Cirelli (2016).

3.2. Dark matter particle candidates

3.2.1. Standard model particles and beyond Under the hypothesis that dark matter is made out of elementary particles, we can summarize the properties that such particles would need to fulfill:

- Massive → gravitational effects observed in lensing, dispersion velocities, rotation curves ...
- Neutral particle → no electromagnetic interaction
- Stable or long-lived such that they didn't decay until today
- At most weak interaction → no strong interaction
- Cold or warm (Cold are particles moving non-relativistic at the time when galaxies started forming, hot particles would be moving relativistic at that time, and warm is in-between)
- Out of the standard model only the neutrino fulfills most of the properties above
- But it would be a hot dark matter candidate [16]
- Phase-space arguments: due to the fermionic character of neutrinos, their occupation number is constrained by the Fermi-Boltzmann distribution, thus, they can not account for the observed dark-matter density in halos [17]

The standard model is very successful in describing particles and their interactions but:

- Does not include neutrino masses
- No explanation for the matter-antimatter asymmetry in the Universe
- Has no explanation for the 3 generations of particles
- Has no unification of forces
- Does not include gravitation
- Does not explain the 'strong CP-problem'

Therefore, we need new models 'beyond the standard model' which ideally provide a new particle to account for dark matter

3.2.2. WIMPs and their production mechanism This is just a brief introduction to WIMPs for completeness, a more detailed discussion of this topic will take place in the next lecture.

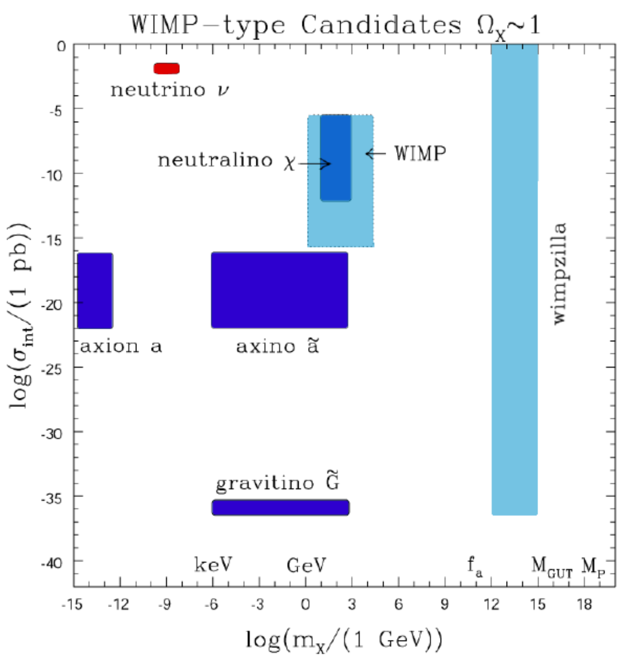

Figure 12. Dark matter particle candidates. Figure from L. Roszkowski arXiv:hep-ph/0404052 [18].

- WIMPs (weakly interacting massive particles) are favoured candidates because they naturally have the right abundance to account for the dark matter
- At high temperatures in the early Universe, WIMPs were in equilibrium with the thermal plasma

- When the Universe expanded, the temperature of the plasma decreased and the number density of created WIMPs also decreased. At a certain point, the comoving number density stays constant: freeze-out [19]
- The freezing out of the number density depends on the interaction cross-section $< \sigma_a v >$. For the typical strength of the weak interaction, the proper relic density results → remarkable coincidence!
- Figure 12 shows the WIMPs together with other particle candidates in the cross-section versus particle mass parameter space [18]

3.2.3. WIMPs in Supersymmetry (SUSY)

- SUSY [20] was proposed by Wess and Zumino in 1973
- Relates bosons (spin integer) to fermions (half-integer). Each particle of the SM has a super partner which differs in the spin by 1/2
- Motivation: unification of EM, weak and strong interaction (see figure 13) and solving the hierarchy problem

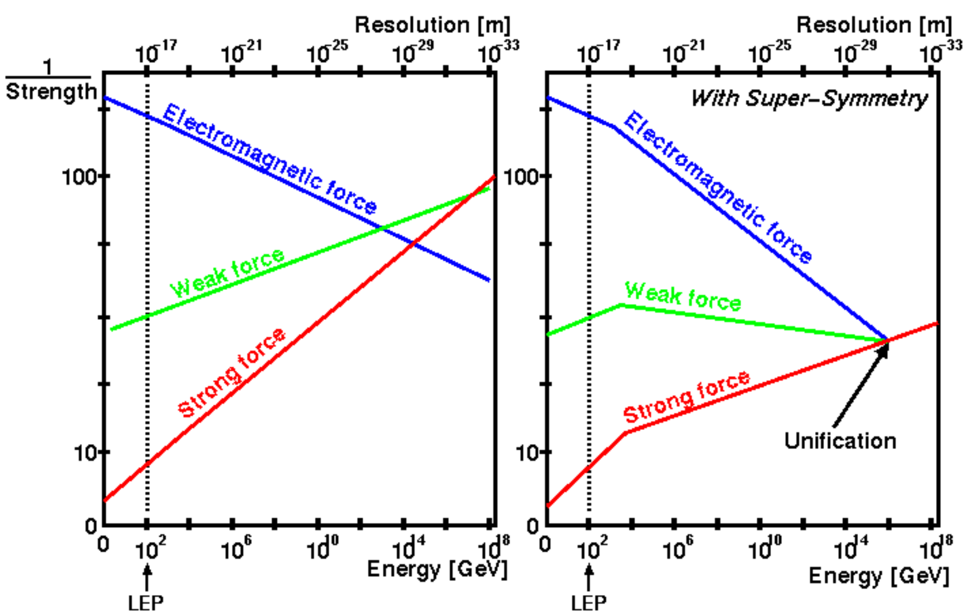

Figure 13. Unification of forces in Supersymmetry. Figure from CERN.

- R-parity is introduced to prevent the decay of the proton. At the same time, it makes the lightest SUSY particle (LSP) stable → ideal DM candidate
- Three possible DM candidates in this model: sneutrino, neutralino and gravitino
- Sneutrino ruled out long ago due to its coupling to Z, direct detection experiments would have measured it already

- Neutralino: a superposition of the partners of the gauge bosons. Several orders of magnitude for cross-section and mass allowed
- Gravitino appears in SUSY theories involving gravitation. Produced non-thermally in the early Universe via decay of another particle. No direct detection possible since it does not couple weakly

- There exist other WIMP candidates originating from different theories (i.e. extra dimensions, little Higgs ..)

3.2.4. Superheavy WIMPs, Sterile neutrinos and axions This section gives only a very brief motivation for superheavy WIMPs, sterile neutrinos and axions as dark matter particles. The latter two candidates will be discussed in detail in dedicated lectures.

- *Superheavy WIMPs*: candidates with dark matter masses $m \sim (10^{12} - 10^{16})$ GeV, see figure 12
- Motivation: observation of ultra-high energy cosmic rays with energies above 10^{19} eV. At this energy a cut-off on the spectrum is predicted (GZK cut-off [21]) due to the interaction of protons with the photons of the CMB

- *Sterile neutrinos*: neutral leptons with no ordinary interactions besides mixing (right-handed ν). Present in many extensions of the standard model. In principle, almost any mass is allowed
- Originally proposed to explain the smallness of neutrino masses (See-saw mechanism). It can also explain the matter-antimatter asymmetry in the Universe. Typical masses $m \sim (10^5 - 10^{12})$ GeV

- *Axions*: In QCD there is no reason to conserve CP but experimental bounds on the neutron electric dipole moment indicate very small CP violation
- In 1977 Peccei and Quinn postulated a new symmetry to solve this issue [22]
- The axion particle appears when the symmetry is spontaneously broken at the scale f_a, axion mass and couplings are: m_a, $g_{aii} \propto 1/f_a$

4. WIMP dark matter

The notions on the thermodynamic of the Early Universe are mostly based on the Kolb and Turner's book [23]. The derivation and solution of the Boltzmann's equation for WIMPs comes from [24]

4.1. Thermodynamics of the Early Universe

- Second law of thermodynamics in a comoving Universe:

$$TdS = d(\rho V) + pdV = d\left[(\rho + p)V\right] - V dp, \quad V = a^3 \tag{24}$$

  combined with the integrability condition:

$$dp = \frac{\rho + p}{T} dT \tag{25}$$

  we define the entropy:

$$dS = d\left[\frac{(\rho + p)V}{T} + \mathrm{const}\right] \tag{26}$$

  and the entropy density:

$$S = sa^3, \quad s = \frac{\rho + p}{T} \tag{27}$$

- From the first law of thermodynamics:

$$d\left[(\rho + p)V\right] = V dp \tag{28}$$

  follows:

$$d\left[\frac{\rho + p}{T} V\right] = 0 \tag{29}$$

  entropy density is conserved in thermal equilibrium:

$$\frac{ds}{dt} = -3Hs \tag{30}$$

- The entropy density can be determined from integrals of the distributions functions:

$$s = \frac{2\pi^2}{45} g_{*s} T^3 \tag{31}$$

4.2. Conditions for thermal equilibrium

A particle species is in thermal equilibrium whether its interactions with the other species in the primordial thermal bath are efficient enough. As a rule of thumb a particle species is in thermal equilibrium whether its interaction rate Γ exceed the Hubble expansion rate:

$$\frac{\Gamma}{H} > 1 \tag{32}$$

4.3. Boltzmann's equation

- The distribution of a particle species ψ, with interactions described by the generic process $\psi + a + b... \leftrightarrow i + j + ...$ is tracked by the Boltzmann's equation:

$$L[f_\psi] = C[f_\psi] \tag{33}$$

with:

$$L[f_\psi] \equiv \text{Liouville operator} = E\frac{\partial f_\psi}{\partial t} - H|\vec{p}|^2 \frac{\partial f_\psi}{\partial E} \tag{34}$$

$C =$ Collision operator.

- For most purposes one can stick on the integrated Boltzman equation:

$$\begin{aligned}
&\frac{g}{(2\pi)^3}\int L[f_\psi]\frac{d^3 p_\psi}{E} = \frac{dn_\psi}{dt} + 3Hn_\psi = \frac{g}{(2\pi)^3}\int C[f_\psi]\frac{d^3 p_\psi}{E} \\
&= -\int d\Pi_\psi d\Pi_a d\Pi_b ... d\Pi_i d\Pi_j ... (2\pi)^4 \delta^4 (p_\psi + p_a + p_b + ... - p_i - p_j - ...) \\
&\left[|M|^2_{\psi+a+b...\to i+j...} f_\psi f_a f_b ... (1 \pm f_i)(1 \pm f_j) ... - |M|^2_{i+j+...\to\psi+a+b} f_i f_j ... (1 \pm f_\psi)(1 \pm f_a)(1 \pm f_b) ...\right]
\end{aligned} \tag{35}$$

where:

$$\begin{aligned}
&(1 + f_i) \equiv \text{Bose enhancement factor (applies to Bosons} \\
&(1 - f_i) \equiv \text{Pauli blocking factor (applies to Fermions} \\
&d\Pi_i = \frac{g_i}{(2\pi)^3}\frac{d^3 p_i}{2E_i}
\end{aligned} \tag{36}$$

- Notice that once passing from the equation from the distribution function to the one for the number density one retains, in the collision term, only the amplitudes of the processes which change the number density of ψ particle.

4.4. WIMP solution of Boltzmann equation

- Consider the case of stable DM particle whose number is controlled by the pair annihilation processes $\psi\psi \to XX$ with X being a SM state.
- General assumptions:
  (i) CP invariance: $|M|^2_{\psi\psi\to XX} = |M|^2_{XX\to\psi\psi}$;
  (ii) Neglect Pauli Blocking and Bose enhancement;

$$\frac{dn_\psi}{dt} + 3Hn_\psi = -\int d\Pi_1 ... d\Pi_4 (2\pi)^4 \delta^4 (p_1 + p_2 - p_3 - p_4)|M|^2 \left[f_\psi(p_1, T) f_\psi(p_2, T) - f_X(p_3, T) f_X(p_4, T)\right] \tag{37}$$

- Specific assumptions for WIMPs:
  (i) SM in thermal equilibrium: $f_X(p_3, T) f_X(p_4, T) = f_X^{\text{eq}}(p_3, T) f_X^{\text{eq}}(p_4, T)$;
  (ii) Maxwell Boltzmann distribution adopted as thermal distribution: $f^{\text{eq}}(p, T) = \exp\left(-\frac{E}{T}\right)$;

(iii) Detailed balance: $f_X^{\rm eq}(p_3, T) f_X^{\rm eq}(p_4, T) = f_\psi^{\rm eq}(p_1, T) f_\psi^{\rm eq}(p_2, T)$;
(iv) Kinetic equilibrium: $f_\psi(p, T) = A(T) f_\psi^{\rm eq}(p, T)$

Under these assumptions the Boltzmann equation becomes:

$$\frac{dn_\psi}{dt} + 3Hn_\psi = -\langle\sigma v\rangle(n_\psi^2 - n_{\psi,eq}^2) \tag{38}$$

$$\begin{aligned}\langle\sigma v\rangle &= \frac{\int \sigma v f_\psi(p_1, T) f_\psi(p_2, T) d^3p_1 d^3p_2}{\int f_\psi(p_1, T) f_\psi(p_2, T) d^3p_1 d^3p_2} \\ &= \frac{1}{8m_\psi^4 T K_2(m_\psi/T)^2} \int_{4m_\psi^2}^\infty ds\sigma(s)\sqrt{s}(s - 4m_\psi^2) K_1\left(\frac{\sqrt{s}}{T}\right)\end{aligned} \tag{39}$$

- Change of variables: $n_\psi \to Y = \frac{n_\psi}{s}, t \to x = \frac{m_\psi}{T}$

$$\begin{aligned}\frac{x}{Y_{\rm eq}}\frac{dY_\psi}{dx} &= -\frac{\Gamma_A}{H}\left[\left(\frac{Y}{Y_{\rm eq}}\right)^2 - 1\right] \\ \Gamma_A &= n_{\psi,eq}\langle\sigma v\rangle\end{aligned} \tag{40}$$

Limit regimes:
(i) $\frac{\Gamma_A}{H} \gg 1 \to Y_\psi = Y_{\psi,eq}$;
(ii) $\frac{\Gamma_A}{H} \ll 1 \to Y_\psi \simeq$ const (decoupling/freeze-out);

- WIMPs are in thermal equilibrium until $x \sim 20 - 30$, hence they decouple in the **non-relativistic regime**. The relic density is approximately given by:

$$\begin{aligned}Y_0 = Y(x_0) &\sim \sqrt{\frac{45}{\pi}}\frac{1}{m_\psi M_{\rm Pl}}\left[\int_{x_f}^{x_0} g_*\langle\sigma v\rangle\right]^{-1} \\ \Omega &= \frac{m_\psi s_0 Y_0}{\rho_c}\end{aligned} \tag{41}$$

The DM relic density is determined solely by the **thermally averaged pair annihilation cross-section**.

- velocity expansion of the thermally averaged annihilation cross-section:

$$\begin{aligned}\langle\sigma v\rangle &\simeq a + \frac{3}{2}bx^{-1} = a + bv^2 \\ a &= \text{s-wave term} = \sigma(s = 4m_\psi^2)\end{aligned} \tag{42}$$

$$\Omega \propto \frac{x_f}{\bar{g}_{\rm eff}^{1/2}}\left[a + \frac{3}{4}\frac{b}{x_f}\right]^{-1} \tag{43}$$

- Simple numerical estimates.

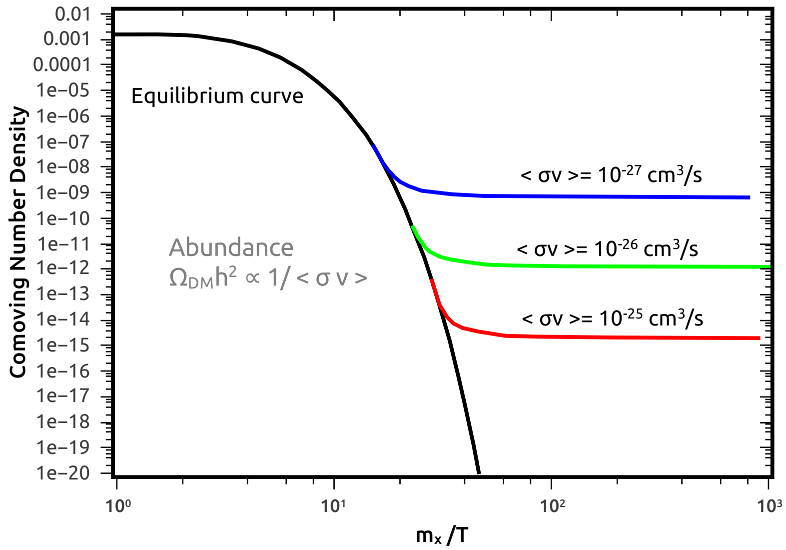

Figure 14. Evolution of the DM comoving abundance for different assignations of the thermally averaged annihilation $\langle \sigma v \rangle$. The figure is taken from [25].

5. Dark matter distribution

5.1. Motivation

- If dark matter (DM) is a particle, there are three main experimental strategies to confirm this hypothesis: indirect-, direct detection and production at accelerators
- For both direct and indirect detection, the morphology (density profile and velocity distribution) of the dark matter halo has an impact on the expected signature and rate

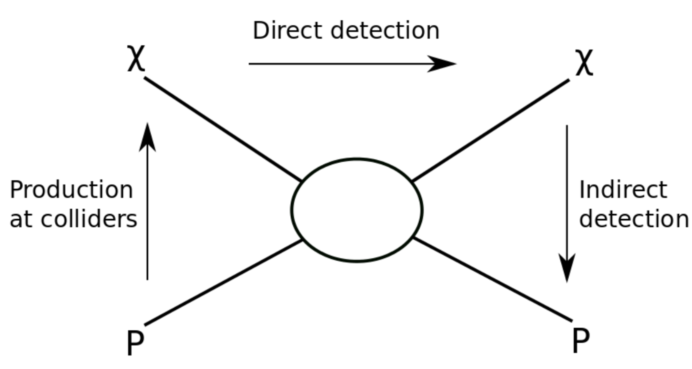

Figure 15. Representation of ways to test the hypothetical particle nature of dark matter. Figure from J. Phys. G: 43 (2016) 1 [26].

- Indirect detection: while the annihilation flux depends on the DM density squared (J-factor), for a particle-decay case the particle flux depends linearly on density

- Direct detection: the rate depends linearly on the DM density and contains the integral over the velocity distribution

5.2. Objects of interest

- Indirect detection: galactic center/halo, Milky Way satellite galaxies and close galaxies/ galaxy-clusters
- Direct detection: Milky Way at the position of the Sun, 8 kpc from the centre of our Galaxy
- Units: $1\,\mathrm{pc} \approx 2.06 \times 10^5\,\mathrm{AU} \approx 3.3\,$light years
- Origin of units: A parsec is the distance such that one astronomical unit subtends an angle of an arcsecond. An astronomical unit (AU) is the Earth-Sun

The Milky Way

- Complex system of stars, gas, dust and dark matter
- Best studied of all galaxies but the measurements challenging because observations are performed 'from inside'
- Recent precise data from the Gaia satellite
- Figure 16 shows an artist's impression of the Milky Way and its main components

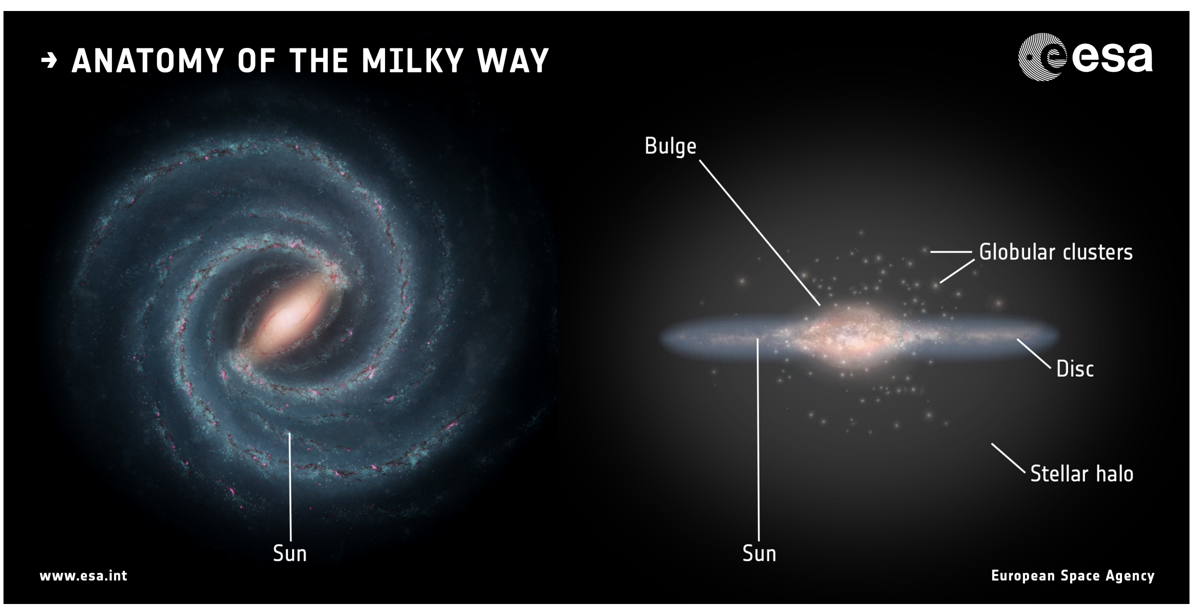

Figure 16. Anatomy of the Milky Way: an artist's impression of our Milky Way galaxy, a roughly 13 billon-year-old 'barred spiral galaxy' that is home to a few hundred billion stars. Figure from Left: NASA/JPL-Caltech; right: ESA; layout: ESA/ATG medialab.

Milky Way satellite galaxies (dwarf spheroidals)

- Galaxies orbiting in the Milky Way at $(15 - 250)$ kpc from the galactic centre
- Best known: large and small Magellanic clouds (discovered in 1591)
- Several objects discovered after 2005 with the Sloan Digital Sky Survey telescope
- Relevance for dark matter: very large mass-to-light ratios, 100 or greater. Therefore, it is unlikely that luminous components have altered the DM distribution in theses systems. These arguments make the dwarf spheroidals a very favoured target for dark matter searches

5.3. Modelling dark matter halos

- $\sim$ 1960: early simulations of the gravitational collapse of a collisionless system (formation of elliptical galaxies)
- 1996: Navarro, Frenk & White (NFW) simulated haloes with 4 orders of magnitude different in mass. A profile steeper than the isothermal is obtained in the central structure of the haloes (see figure 17). The profile is 'universal', i.e. same shape for all simulated halo masses [27].

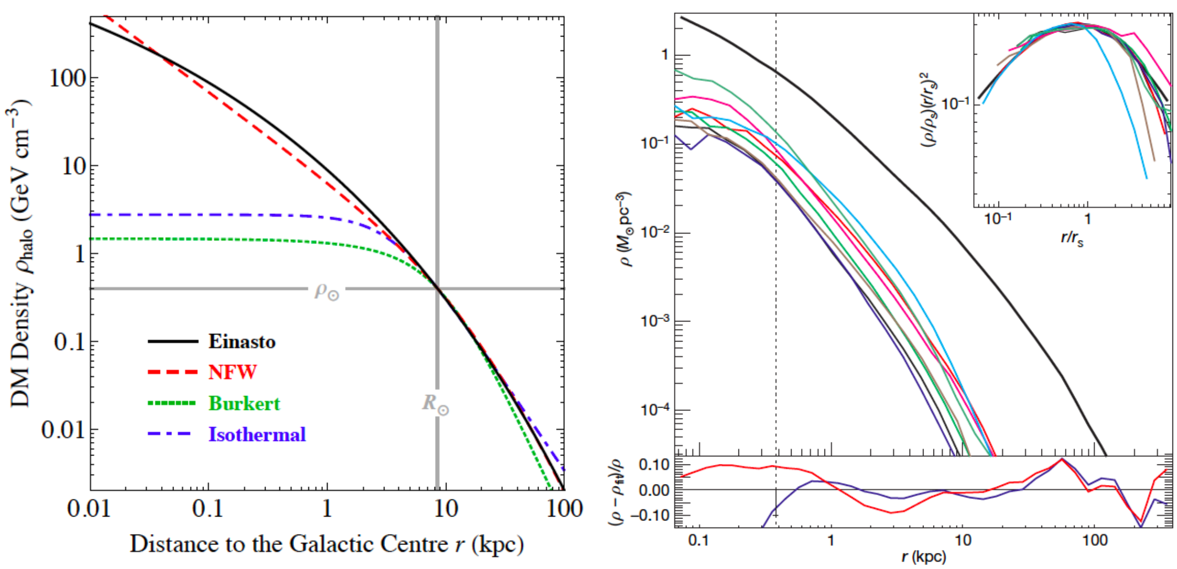

Figure 17. Left: comparison of different dark matter density profiles for the Galactic halo. Figure from A. Albert *et al.*, arXiv:1406.3430. Left: Via Lactea II, density profiles of main halo and subhaloes. Profile of a Milky Way-sized galaxy (black line) and eight large sub haloes (thin lines). Figures from J. Diemand *et* al. [28].

- $\sim$ 2006: Full cosmological simulations starting from CMB anisotropies (Millennium simulation [7]). These are dark-matter only simulations. Baryonic matter is added to subsamples of the simulation using semi-analytic techniques to study galaxy formation

- 2008: Detailed simulations of MW-like galaxies from parts of the cosmological simulations: Acquarius [29], GHALO [30] and Via Lactea [28]
- ∼ 2013: New simulations/studies show the effects of baryonic matter on the dark matter profile. For instance, the Illustris includes baryons in the simulation including cooling mechanisms, stellar evolution and feedback, chemical enrichment, supermassive black-hole growth and feedback from AGNs.

Density profile

- Dark matter simulations show universal profiles (figure 17) pointing to a fractal nature of dark matter clustering
- All dark matter only simulations favour steeper profiles (CUSP) while observations favour flatter ones (CORE). The so called 'CUSP/CORE problem' has been during long time seen as a challenge for the cold dark matter model. Recent simulations including baryonic matter show that baryonic matter could account for the profile differences

Velocity distribution

- Simulations find triaxial velocity distributions. Example from Aquarius [31] in fig 18
- High velocity tails have a large impact on direct detection experiments

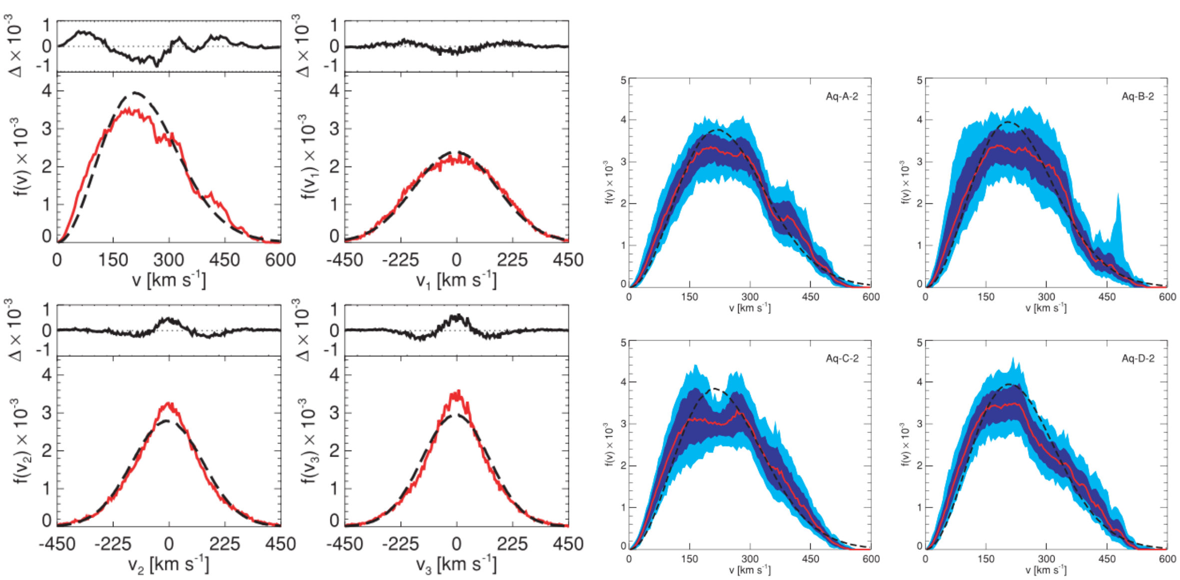

Figure 18. (Left) Velocity distributions for six haloes simulated with Aquarius in a 2 kpc box at a position similar to our Sun. v_1, v_2 and v_3 are the velocity components parallel to the major, intermediate and minor axes of the velocity ellipsoid. (Right) Velocity modulus distribution for four simulated haloes at high resolution. All distributions are smooth and show characteristic broad bumps which are present in all boxes for a given halo. Figures from M. Vogelsberger *et al.* [31].

Uncertainties in indirect detection

- J-Factors differ for the different DM profiles, specially in the center region of the haloes
- In addition, the amount of substructure considered lead to significant changes in sensitivity (see chapter 10)

5.4. The standard halo model (SHM)

- Employed in direct detection to derive results with a common local density and velocity distribution for all experiments
- SHM: isotropic and isothermal with $\rho \propto 1/r^2$
- The solution of the collision less Boltzmann equation is a Maxwellian velocity distribution. This function is usually truncated to be 0 at the escape velocity (for which particles are not bound in the gravitational potential anymore)
- Standard parameters of the Milky Way SHM [32]:
  - Local dark matter density: $0.3\,\mathrm{GeV/cm^3}$
  - Circular speed: $(220 \pm 20)\,\mathrm{km/s}$ and escape velocity: $544\,\mathrm{km/s}$
- Direct detection experiments use the SHM but the results are not astrophysics independent

Uncertainties in the determination of halo parameters

- Dark matter density: calculated via mass modelling of the Milky Way (simulations with cored or cusped profiles and models using equations). Standard value uses parameters in agreement with observational data. Depending on the profile model used for the halo, a density range from $(0.2-0.6)\,\mathrm{GeV/cm^3}$ can be derived (see [33])
- Circular velocity: velocities ranging from $(200 \pm 20)\,\mathrm{km/s}$ to $(279 \pm 33)\,\mathrm{km/s}$ are found [32] (also dependent on the Milky way profile used).
- Escape velocity: the commonly used value of $544\,\mathrm{km/s}$ is the likelihood median calculated using data from the RAVE survey [34]. The 90% confidence interval contains velocities from $498\,\mathrm{km/s}$ to $608\,\mathrm{km/s}$.

6. Direct detection

6.1. Principles of direct detection

- For a $\sim (10 - 1000)\,\text{GeV}/c^2$ WIMP mass with the velocities of the standard halo model, nuclear recoils with target nuclei in $\sim (1 - 100)\,\text{keV}$ result
- A nucleus moving through a medium can create ionisation, excitation and heat
- Separation of recoils from different particles (electronic and nuclear recoils) is possible by combining different signals. This is called 'discrimination'
- Due to the low cross section of particles being tested, only a single interaction is expected. The probability for multiple interactions is negligible
- WIMP interactions are expected to be homogeneously distributed in the detector volume while interactions due to several of the background processes are expected to occur at the outermost layers of the target material. By using the innermost volume of the data, the signal/noise ratio is improved (fiducialization)

Spectral shape

- exponentially falling spectrum. Differential rate can be written as

$$\frac{dR}{dE}(E,t) = \frac{\rho_0}{m_\chi \cdot m_A} \cdot \int v \cdot f(\mathbf{v},t) \cdot \frac{d\sigma}{dE}(E,v)\ \mathrm{d}^3 v \tag{44}$$

with σ and m_χ the dark matter cross-section and mass, respectively. ρ_0 is the local dark matter density and $f(\mathbf{v},t)$ the velocity distribution of the particles in the halo.
- This expression can be approximated by

$$\frac{dR}{dE}(E) \approx \left(\frac{dR}{dE}\right)_0 F^2(E) \exp\left(-\frac{E}{E_c}\right), \tag{45}$$

where $\left(\frac{dR}{dE}\right)_0$ denotes the event rate at zero momentum transfer and E_c is a constant parameterizing a characteristic energy scale which depends on the dark matter mass and target nucleus [35]. See figure 21
- The signal is dominated at low recoil energies by the exponential function. $F^2(E)$ is the form-factor correction which will be described later.

Annual modulation

- As a consequence of the Earth rotation around the Sun, the speed of the dark matter particles in the Milky Way halo relative to the Earth is largest around June 2nd and smallest in December. Consequently, the amount of particles able to produce nuclear recoils above the detectors' energy threshold is also largest in June [36].

The temporal variation of the differential event rate can be written as follows [37]:

$$\frac{dR}{dE}(E,t) \approx S_0(E) + S_m(E) \cdot \cos\left(\frac{2\pi(t-t_0)}{T}\right), \tag{46}$$

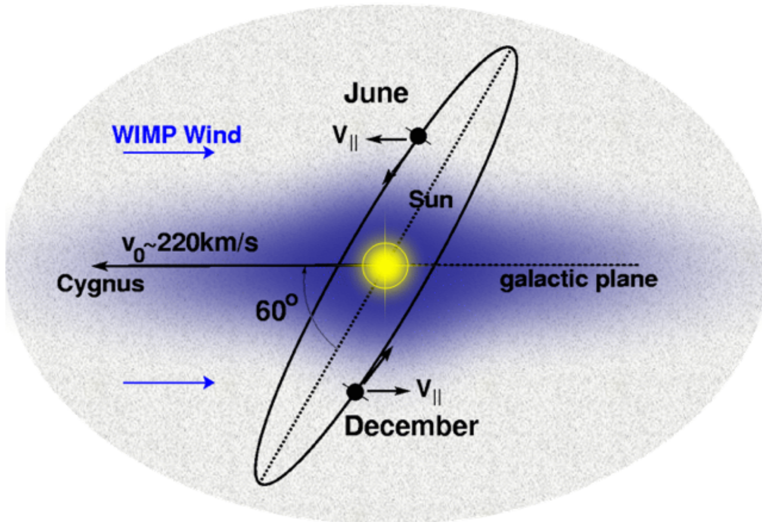

Figure 19. Scheme of the kinematic leading to an annual modulation of the dark matter event rate.

with t_0 the phase which is expected at about 150 days and T the period expected to be one year. The time-averaged event rate is denoted by S_0, whereas the modulation amplitude is given by S_m.

Directional dependence of the signal

- Strong angular dependence of the direction of the nuclear recoils resulting from WIMP interactions [38]. Dependence becomes clear in the differential rate equation when it is explicitly written as a function of the angle γ, between the direction of the nuclear recoil relative and the mean direction of the solar motion

$$\frac{dR}{dE\ d\cos\gamma} \propto \exp\left[\frac{-[(v_E + v_\odot)\cos\gamma - v_{min}]^2}{v_c^2}\right]. \tag{47}$$

  In equation 47, v_E represents the Earth's motion, $v_\odot$ the velocity of the Sun around the galactic centre, v_{min} the minimum WIMP velocity that can produce a nuclear recoil of an energy E and v_c the halo circular velocity $v_c = \sqrt{3/2}v_\odot$.
- The rate of events scattering in the forward direction will, therefore, exceed the rate for backwards scattering events.
- A detector able to determine the direction of the WIMP-induced nuclear recoil would provide a powerful tool to confirm the measurement of these particles.

Cross sections and form factors

- Typically two cases are considered. Spin-independent: assuming that the protons and neutrons contribute equally (isospin conservation). Spin-dependent: nuclei

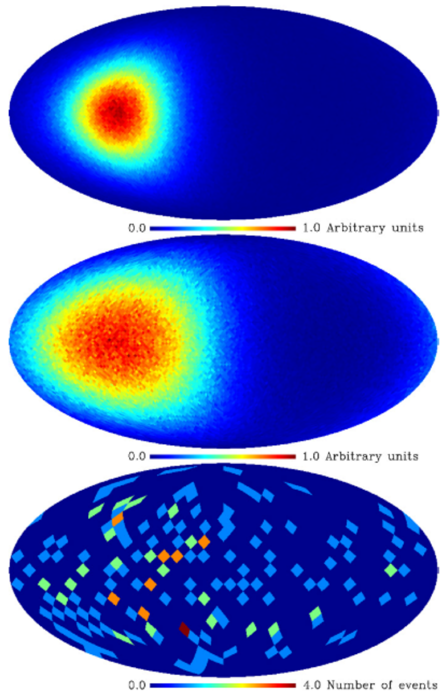

Figure 20. Directionality signature: (top) WIMP flux in the case of an isothermal spherical halo, (middle) WIMP-induced recoil distribution and (bottom) a typical simulated measurement: 100 WIMP recoils and 100 background events (low angular resolution). Figure from J. Billard et al. 2010.

with an odd number of protons/neutrons contribute. The cross section σ is related to the quark spin content of the nucleon

- For momentum transfer q, such that the wavelength is small compared to the nuclear radius, σ decreases with q. The form factor account for this effect:

$$\sigma \propto \sigma_0 \cdot F^2, \tag{48}$$

where σ_0 is the cross-section at zero momentum transfer. Figure 21 shows the effect of the form factor for different target nuclei. For heavy nuclei, the rate of nuclear recoils at large recoil energies is strongly suppressed.

- The differential WIMP-nucleus cross section, $d\sigma/dE$ shown in equation 44, can be written as the sum of a spin-independent (SI) contribution and a spin-dependent (SD) one,

$$\frac{d\sigma}{dE} = \frac{m_A}{2\mu_A^2 v^2} \cdot (\sigma_0^{\mathrm{SI}} \cdot F_{\mathrm{SI}}^2(E) + \sigma_0^{\mathrm{SD}} \cdot F_{\mathrm{SD}}^2(E)). \tag{49}$$

The WIMP-nucleus reduced mass is described by μ_A.

- For spin independent interactions, the cross-section at zero momentum transfer can be expressed as

$$\sigma_0^{\mathrm{SI}} = \sigma_p \cdot \frac{\mu_A^2}{\mu_p^2} \cdot [Z \cdot f^p + (A-Z) \cdot f^n]^2 \tag{50}$$

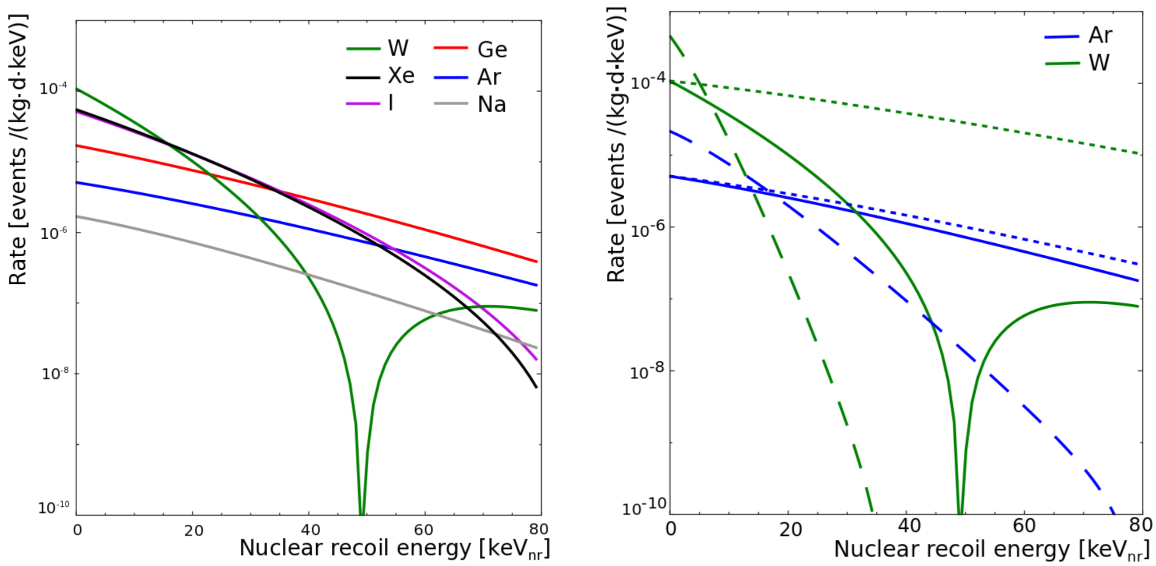

Figure 21. (Left) Event rates as function of nuclear recoil energy for different target materials assuming a $100\,\mathrm{GeV}/c^2$ WIMP mass and an interaction cross section of $10^{-45}\,\mathrm{cm}^2$ (solid lines). (Right) Event rates for argon and tungsten. Dotted line: no form factor correction. Dashed line: for a $25\,\mathrm{GeV}/c^2$ WIMP mass. Figures from [26].

where $f^{p,n}$ are the contributions of protons and neutrons to the total coupling strength, respectively, and μ_p is the WIMP-nucleon reduced mass. Usually, $f^p = f^n$ is assumed and the dependence of the cross-section with the number of nucleons A takes an A^2 form.

- F_{SI} is calculated assuming that the distribution of scattering centres is similar to the charge distribution obtained in electron scattering experiments. Helm form factor is typically used (see figure 22)
- In the dark matter field, it is common to display the spin dependent cross section with protons and with neutrons

$$\sigma_0^{\mathrm{SD}} = \frac{32}{\pi}\mu_A^2 \cdot G_F^2 \cdot [a_p \cdot \langle S^p \rangle + a_n \cdot \langle S^n \rangle]^2 \cdot \frac{J+1}{J} \tag{51}$$

with G_F^2 the Fermi coupling constant, J the total nuclear spin and $a_{p,n}$ the effective proton (neutron) couplings. The expectation value of the nuclear spin content due to the proton (neutron) group is denoted by $\langle S^{p,n} \rangle$.

Generic result of a direct dark matter experiment

- Outcome of an experiment is an event rate with a certain spectral shape. Results are then commonly displayed in a parameter space of the dark matter-nucleon cross-section and the dark matter mass.
- First question: is there statistical significance of signal over background?
- If answer YES: Signal contours at a certain confidence level ($2\,\sigma$ are typical)

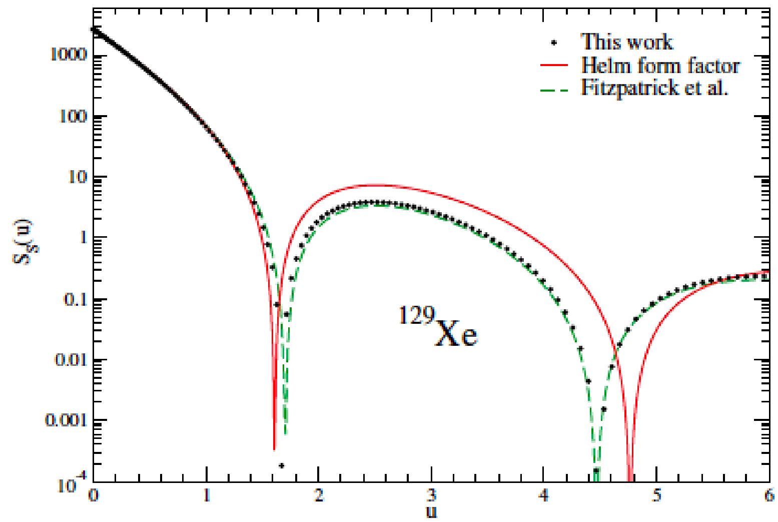

Figure 22. Structure factor $S_S(u)$ for ^{129}Xe (black dots) in comparison with the Helm form factor (red) and the Fitzpatrick structure factor. Figure from L. Vietze et al. PRD 91 (2015) 043520 and arXiv:1412.609.

- If answer NO: curve as the left plot in figure 23, generic limit (open black curve). At low WIMP masses the sensitivity is reduced mainly due to the low-energy threshold of the detector. Minimum of the exclusion curve given by the kinematics of the scattering process which depends on the target nucleus mass At larger WIMP masses, the event rate is overall suppressed by $1/m_\chi$

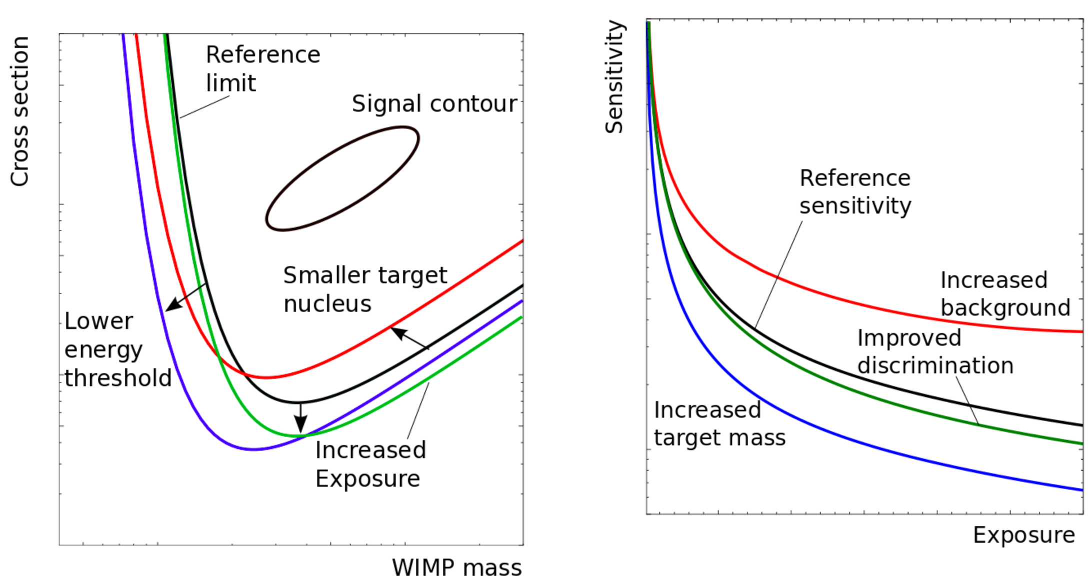

Figure 23. Sensitivity of direct detection experiments for different detector parameters. Figures from [26].

- Evolution of the sensitivity versus the exposure: figure 23 (rigth) illustrates the evolution of the sensitivity to the cross-section with respect to the exposure. For a given detector mass, the increase in exposure is caused by the accumulation of measuring time

6.2. Backgrounds

Gamma radiation

- Dominant radiation from gamma-decays originates from the decays in the natural uranium and thorium chains, as well as from decays of common isotopes e.g. ^{40}K, ^{60}Co and ^{137}Cs present in the surrounding materials. Energies from tens of keV up to 2.6 MeV (highest γ-energy from the thorium chain).
- The interactions of γ-rays with matter include the photoelectric effect, Compton scattering and $e^- e^+$ pair production [39]. In all these processes: emission of an electron (or electron and positron for the pair production) which can contribute to the experiment's background.
- Reduction by selecting materials with low radioactive traces. Gamma-spectroscopy using high-purity germanium detectors is a common technique to screen and select radio-pure materials. Other techniques: mass spectrometry or neutron activation analysis [40].
- Shielding γ's: by surrounding the detector by a material with a high atomic number and a high density, i.e. good stopping power, and low internal contamination. Lead is a common material (see figure 25) but also large water tanks are employed: homogeneous shielding and low background. See figure 25.

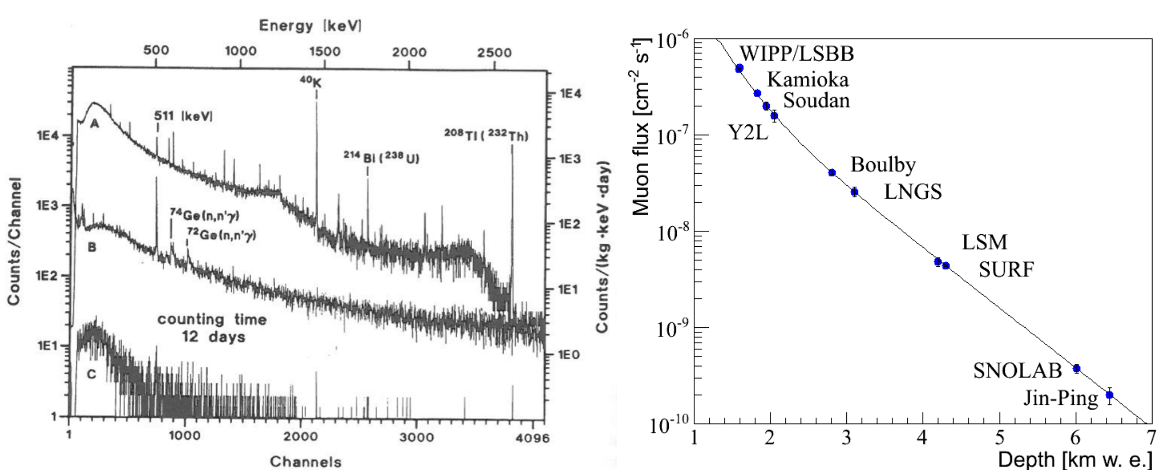

Figure 24. Left: Background spectra of a Ge detector without shield (top), with 15 cm lead shield (middle), and with shield and at 500 m.w.e. (bottom). Right: Total muon flux measured for the various underground sites as function of the equivalent vertical depth relative to flat overburden. Figure from arXiv:1509.0876.

Neutron radiation

- Neutrons can interact with nuclei via elastic scattering producing nuclear recoils. Dangerous background: identical signal to the one of the WIMPs.
- Cosmogenic neutrons: spallation reactions of muons on nuclei in the experimental setup or surrounding rock. Neutron energies up to several GeV [41] which are moderated to MeV energies $\rightarrow$ can produce nuclear recoils in the energy regime relevant for dark matter searches.
- Radiogenic neutrons: emitted in (α, n)- and spontaneous fission reactions from natural radioactivity (MeV energies)
- Shielding: experiments are typically placed at underground laboratories in order to minimise the contribution of muon-induced neutrons. The deeper the location, the lower the muon flux. Figure 25 (right) shows the muon flux as a function of depth (km water equivalent, has to multiplied by the density of the rock to obtain the value in km) for different underground laboratories.

Neutron background reduction:

- Material selection: low uranium and thorium content give lower α- and spontaneous fission rates.
- Neutron shielding: water or polyethylene layers installed around the detectors to moderate the neutrons effectively [42] (see figure 25). Active vetoes are designed to record interactions of muons. Plastic scintillator plates are, for example, used for this purpose. Also water Cherenkov detectors: higher muon tagging efficiency (full coverage), efficient in stopping neutrons and external gammas. To tag directly the interactions of neutrons, liquid scintillator shielding can be used.

Figure 25. Examples of detector shielding using layers of lead, copper and polyethylene: DAMA detector (left) and XENON100 detector (right).

Neutrino background

- With increasing target masses (hundreds of kilograms to tons) dark-matter detectors are sensitive to neutrino interactions → significant background contributing both to electronic and nuclear-recoils.
- Solar neutrinos: elastic scattering off electrons [43]. pp- and ^{7}Be-neutrinos (large fluxes) would be the first neutrinos which could be detected. The resulting signal is a recoiling electron. See figure 26, left side (green curve)
- Coherent neutrino-nucleus elastic scattering also possible producing nuclear recoils with energies up to few keV [44]. Process measured recently by the COHERENT collaboration [45]. Coherent scattering of solar neutrinos would limit the sensitivity of dark matter experiment for low WIMP masses (few GeV). For higher masses, atmospheric neutrinos would limit dark matter searches [46]. See figure 26 (right).

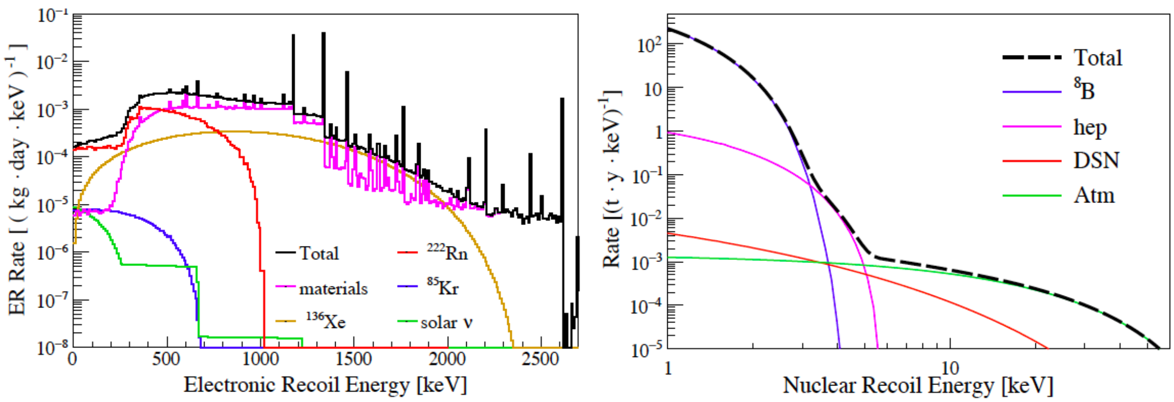

Figure 26. Neutrino background, example for liquid xenon detectors. (Left) Contribution of ER from solar neutrinos (green) in comparison with other backgrounds. (Right) Spectral shape of coherent neutrino scattering in xenon. Figures from XENON Coll., arXiv:1512.07501.

Internal and surface backgrounds

- **Crystalline detectors:** contamination of the crystal matrix negligible: targets grown from high purity powders or melts.
- Most important are surface contaminations. Either α-, β-decays or the nuclear recoils associated to the latter can enter the crystal depositing part of its energy.
- Cosmic activation of the target or detector surrounding materials: spallation of nuclei by high energy protons and neutrons producing long-lived isotopes. Precautions: minimising time at surface and avoiding transportation via airplane

- **Noble gas detectors:** internal background originating from cosmogenic-activated radioactive isotopes contained in the target nuclei.
- Argon: ^{39}Ar with an endpoint energy at 565 keV at a level of 1 Bq/kg in natural argon. Reduction by using underground argon.

- Xenon: cosmic activation produces rather short-lived isotopes. Xenon also contains a double beta decaying isotope: ^{136}Xe. Its lifetime is so large, 2.2×10^{21} y [47], that it doesn't contribute to the background for detectors up to few tons mass.
- Contamination of the target with krypton and the radon emanation from the detector materials. ^{85}Kr: β-decaying isotope produced in nuclear fission. It is released to the atmosphere by nuclear-fuel reprocessing plants and in nuclear weapons tests. Krypton can be removed from xenon either by cryogenic distillation or using chromatographic separation.
- Radon is emanated from all detector materials containing traces of uranium or thorium and it is dissolved in the liquid target. An approach to reduce radon is to use materials with low radon emanation. Furthermore, distillation or adsorption can be employed to continuously remove the emanated radon.

6.3. Statistical treatment of data

- Result of a dark matter experiment: (eventually) a small number of signal events + a number of background events
- Question: is there statistical significance of a signal over the expected background?
- Counting method: Need to take into account signal, background and their corresponding fluctuations. Feldman and Cousins method [48] is used to derive both two-sided confidence intervals and upper confidence limits.

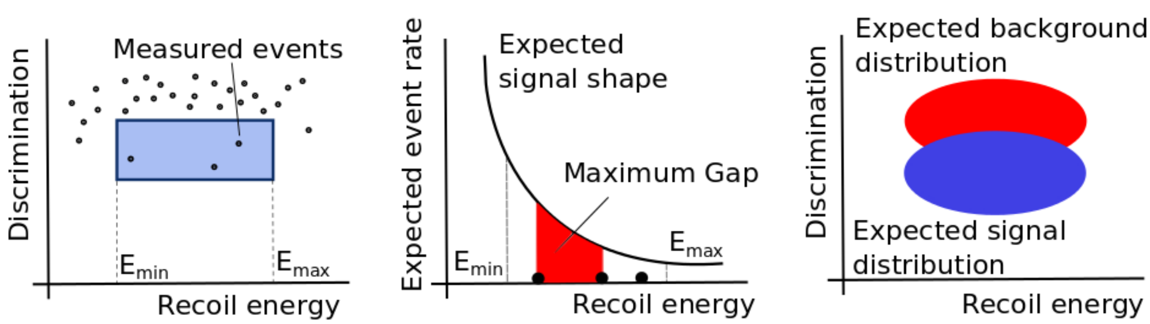

Figure 27. Illustration of different statistical methods used to derive results from direct detection experiments. Figure from [26].

- Maximum gap or optimum interval method (also called Yellin's method [49]): takes into account the shape of the expected signal but does not make any assumption on the background. It is used when there is no knowledge (or poor knowledge) about the background. Disadvantage: can be used only to set upper limits.
- Maximum likelihood methods: used when it is possible to determine the probability density function (pdf) of both signal and background
- Two hypotheses tested: background only and background + signal hypothesis

- For non-discriminating experiments: 1-dimensional pdf (energy dependence) of signal and background. For experiments that can separate electronic recoils (background) from nuclear recoil (signal), a 2-dimensional pdf (energy and discrimination parameters) are considered.

6.4. Detector calibration

- Goals: characterise the energy scale, determine signal and background regions and monitor the response and stability of the detector.

Calibration of recoil energies

- Conversion from phonons, photons or charge to a recoil energy (keV$_{nr}$)
- Methods to determine the conversion to recoil energy: neutron scattering experiments, MC/data comparisons and modelling of underlying processes

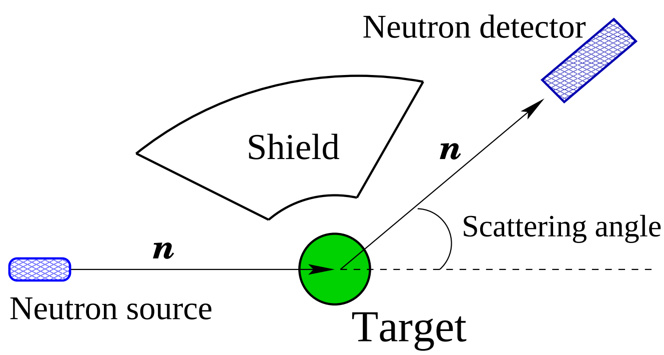

Figure 28. Schematic of a neutron scattering experiment. From [26].

- Neutron scattering experiments: use mono a energetic neutron source, a detector with the medium of interest and a coincidence detector. For fixed kinematics, the nuclear recoil energy is also fixed.

Determination of signal and background regions

- The signal and background regions are typically defined via dedicated calibration campaigns in between the science data taking.
- The distribution of nuclear recoils (signal region) can be studied selecting interactions of neutron sources such as ^{241}AmBe or ^{252}Cf.
- Most of the background is due to electronic recoils from γ-interactions in the target. Commonly, radioactive sources like ^{133}Ba, ^{137}Cs, ^{60}Co or ^{232}Th are used. For liquid noble-gas detectors also internal backgrounds need to be characterised. Internal sources such as tritium or ^{220}Rn are used.
- Figure 29 shows schematically how signal (in blue) and background (in red) events are distributed for some detector technologies

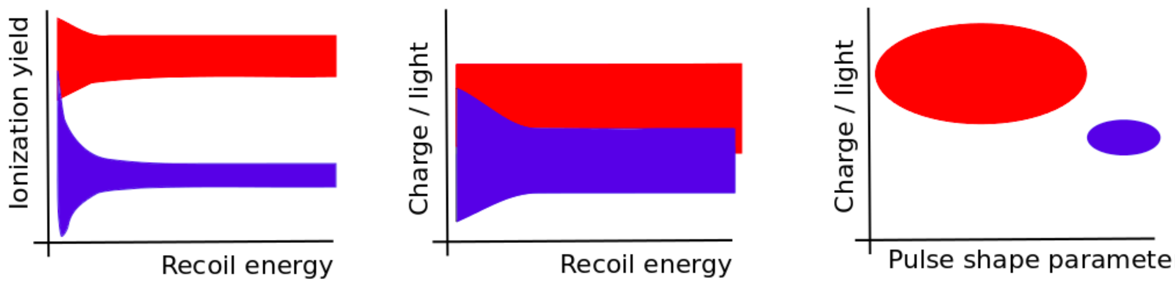

Figure 29. Schematic representation of signal (blue) and background (red) regions for a bolometer like a germanium detector (left), a liquid xenon TPC (middle) and a liquid argon TPC (right).

6.5. Experiments and results

The energy deposition from a WIMP-induced interaction can results in a measurable signal which depends on the technology used. Phonons are produced in crystals, photons in scintillators and charges in ionization detectors. While one of these signals can be employed to reconstruct the energy of the recoil, the addition of another signal allows to distinguish between different types of particles. This section described most of the technologies that can be used for direct detection of dark matter.

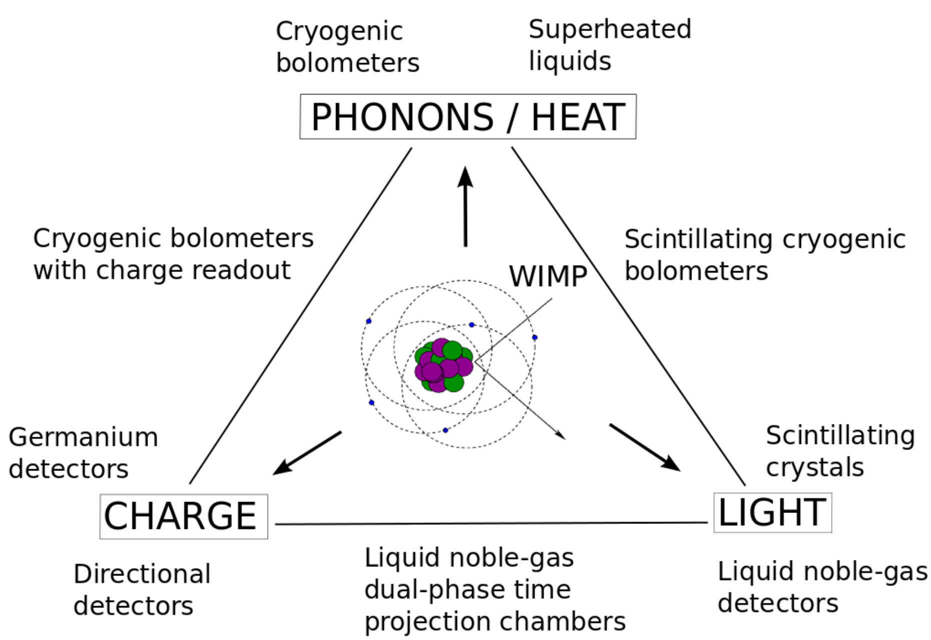

Figure 30. Schematic of signals in different detection technologies. From [26]

.

Scintillator crystals at room temperature

- Scintillation: energy deposition by particles produce excitation of the medium which de-excites via photon emission
- Mostly NaI (Tl) and CsI (Tl) are used in DM searches. Advantages are the high density and large light output.
- It is a 'simple' technology (good for long term stability), low backgrounds can be achieved (very pure crystals)
- Disadvantages: crystals of several cm^3 $\rightarrow$ arrays of crystals are necessary to achieve large target masses. Most important: no electronic/nuclear recoil discrimination.
- Annual modulation signature is used

- **DAMA experiment** at LNGS laboratory in Italy
- Annual modulating signal present in the data (20 annual cycles), $\sim$ $13\,\sigma$ significance, exposure of 2.46 ton.y [50]

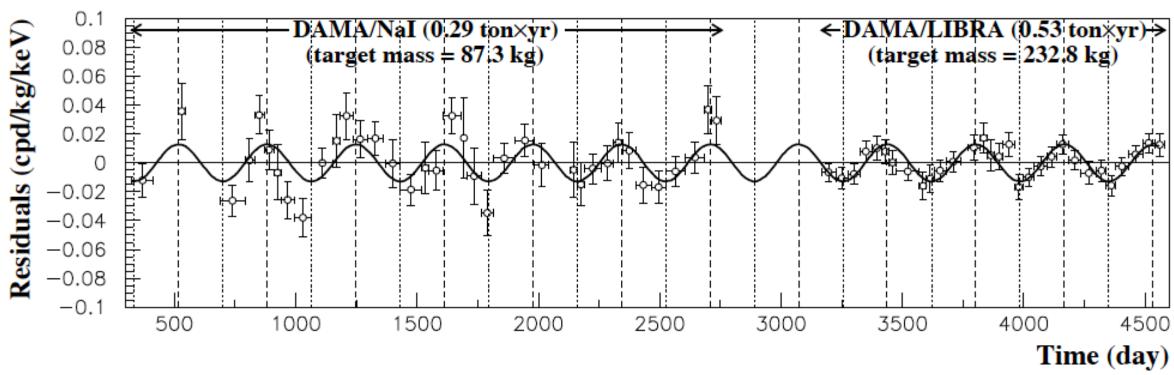

Figure 31. Residual rate of single-hit scintillation events by the DAMA/LIBRA experiment in the $(2-6)$ keV energy region as a function of time. A sinusoidal function fitting the data is also shown. Figure from EPJC 56 (2008) 333[51].

- Signal in the $(1-6)$ keV energy range with maximum compatible with expectation within $2\,\sigma$. Figure 31 shows the data as released in 2008 (with a threshold of 2 keV)

- But many other experiments cannot confirm (i.e. have excluded) most of the dark matter interpretations of the DAMA signal. Therefore the origin of the signal remains unclear/controversial
- Other non-dark matter related explanations of the DAMA signal: atmospheric muons (annually modulated due to temperature variations in the stratosphere [52]), combinations of muons and modulated neutrinos (caused by the varying Sun-Earth distance [53]) or varying rates of background neutrons have been considered [54]

Cryogenic bolometers

- Advantages: very good energy resolution and threshold, and separation of signal and background by combining phonon/charge and phonon/light signals
- Disadvantages: scalability ($\sim 1\,\mathrm{kg}$ crystals in mK temperature cryostats)
- Working principle: an energy deposition by a charged particle recoil is dissipated via collisions with the nuclei and electrons in the crystal lattice. Phonons are produced in this process.
- A bolometer measures an increase of temperature which is related to the heat capacity of the crystal. The signal has an exponential decay shape related to the thermal conductance of the thermal link (see figure 32 left)

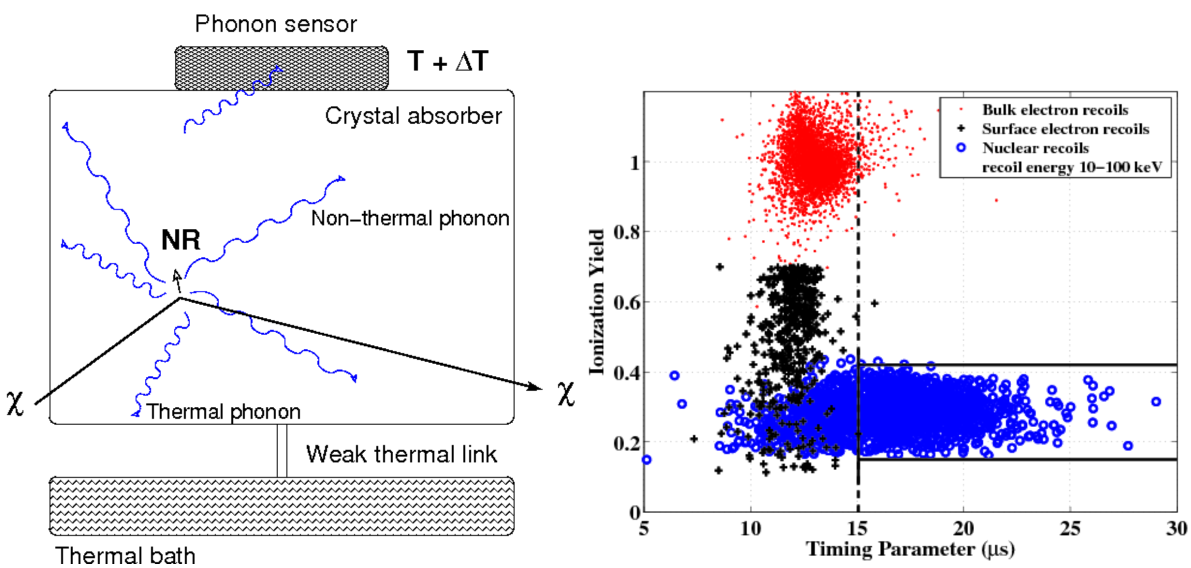

Figure 32. Left: Schematic of a cryogenic phonon detector: an energy deposition E from a nuclear recoil (NR) in an absorber of capacity C(T) produces a temperature rise T which is measured by a thermal sensor. Right: Ionisation yield and timing parameter for electronic recoils, nuclear recoils and surface events. Figure from CDMS Coll., PRL 102 (2009) 011301.

- The thermal bath is typically at $(10-100)\,\mathrm{mK}$. Example: for a germanium detector at $20\,\mathrm{mK}$, few keV_{nr} would procude approx. $1\,\mu\mathrm{K}$ temperature difference

- Phonon and charge read-out: in germanium or silicon detectors. Very good particle separation (see figure 32 right). SuperCDMS [55] and Edelweiss [56] are examples of such detectors
- Phonon and light detection: using scintillating bolometers (for example $CaWO_4$). CRESST is an example of an experiment using this technology. Experiment with sensitivity to the lowest WIMP masses [57] (see figure 36)

Liquid noble-gas detectors

- Advantages: large masses and homogeneous targets can be built. Events can be reconstructed in 3D
- Working principle: the energy deposition from a nuclear recoil excites (R^*) and ionizes (R^+) the medium

  Scintillation: $R^* + R \rightarrow R_2^*$ followed by $R_2^* \rightarrow 2R + h\nu$. The scintillation light $h\nu$ appears with two time constants: $5\,\text{ns}/1.6\,\mu\text{s}$ and $3\,\text{ns}/30\,\text{ns}$ for argon and xenon, respectively. Ionization: creation of electrons and ions in the medium
- Without electric field: all charges recombine giving additional scintillation light
- With an electric field applied: part of the charges (e^-) are extracted and cannot recombine (less light) but an additional signal can be read out
- Two detector versions: single and double-phase. In both cases the innermost volume can be selected for analysis

- **Single phase**
- Liquid volume surrounded by photosensors. Very good light collection (4π). Particle separation possible through pulse shape

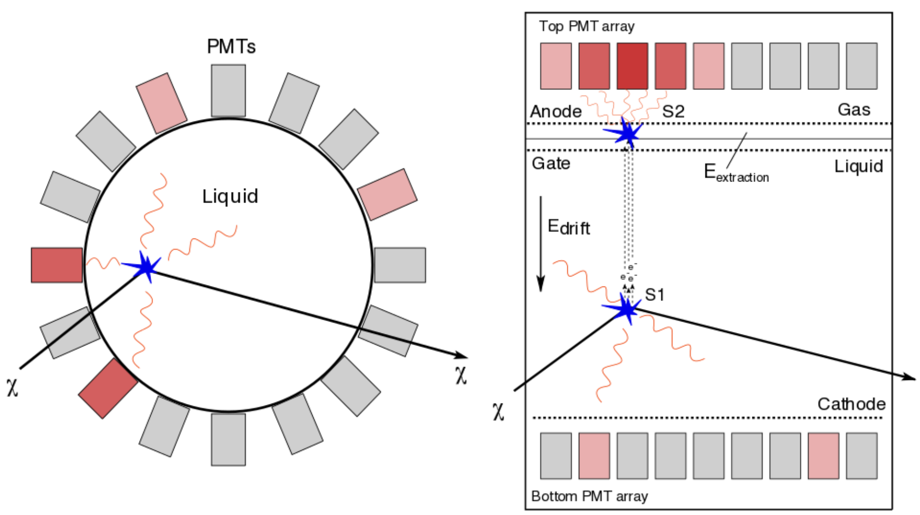

Figure 33. Schematic of single-phase (left) and double-phase (right) liquid noble-gas detectors.

- DEAP [58] (LAr) at SNOLAB in Canada and XMASS [59] (LXe) at Kamioka in Japan are example of single-phase liquid noble gas detectors

- **Double-phase TPC**
- Both light and charge signals are recorded. Charges are extracted from the interaction point with an electric drift field. These charges are amplified and converted to light in the gas phase.

- XENON [60] at LNGS in Italy, PandaX at Jin-Ping in China [61] and LUX at Sanford in the US [62] are examples of LXe TPCs. Dark-Side is an example of a LAr TPC [63]
- As shown in figure 36 liquid xenon TPCs have most sensitive constrains on the cross section to ordinary matter for WIMP masses above $\sim 5\,\mathrm{GeV}/c^2$

Superheated fluids

- Bubble chambers and droplet detectors
- Working principle: superheated liquid below the boiling point. Charged particles create ionization/heat that result into bubble formation (see figure 34). when the bubbles grow, the can be photographed with CCD cameras

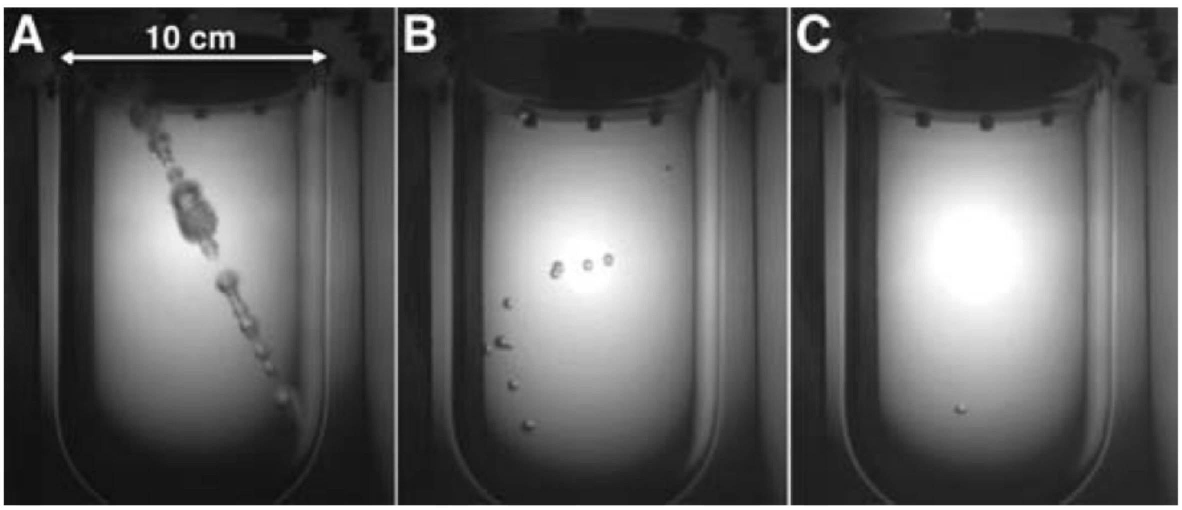

Figure 34. Events in a superheated-liquid bubble chamber (1.5 kg of CF_3I). A: muon track, B: nuclear recoils from neutrons, C: expected signature of a WIMP interaction, a single nuclear recoil bubble. Figure from E. Behnke et al., Science 319 (2008) 933. [64]

- Advantages: Low background: the detector can be tuned to be sensitive only to high dE/dx particles → no background from e^-, γ, β and muons. In addition, very good sensitivity to spin-dependent interactions. Fluorine is used in the target and has a particular large expectation value for the proton spin content which enhances the sensitivity for spin dependent interactions to protons
- Disadvantages: Deadtime after the bubble formation because the medium needs to be recompressed. Background from α-particles, which can however be reduced using the acoustic signal (the sound of an alpha particle is different from the sound of a nuclear recoil!)
- Best results on spin-dependent proton coupling from the PICO experiment [65]

Directional searches

- Very clear signature: strong direcctional dependence of the signal
- Range of s WIMP-induced nuclear recoil in solids/liquids $< 100\,\mathrm{nm}$ for $\mathrm{E}_{th} <$ 200keV
- Low pressure gas TPCs are employed ($< 130\,\mathrm{mbar}$)
- A $100\,\mathrm{GeV}/c^2$ WIMP mass with $220\,\mathrm{km/s}$ velocity can produce a recoil track of 1-2 mm
- Disadvantage: low pressure means low density and this implies a low target mass. 'Huge' detectors are necessary to be competitive. Another difficulty is the diffusion of the charges when they drift through the medium

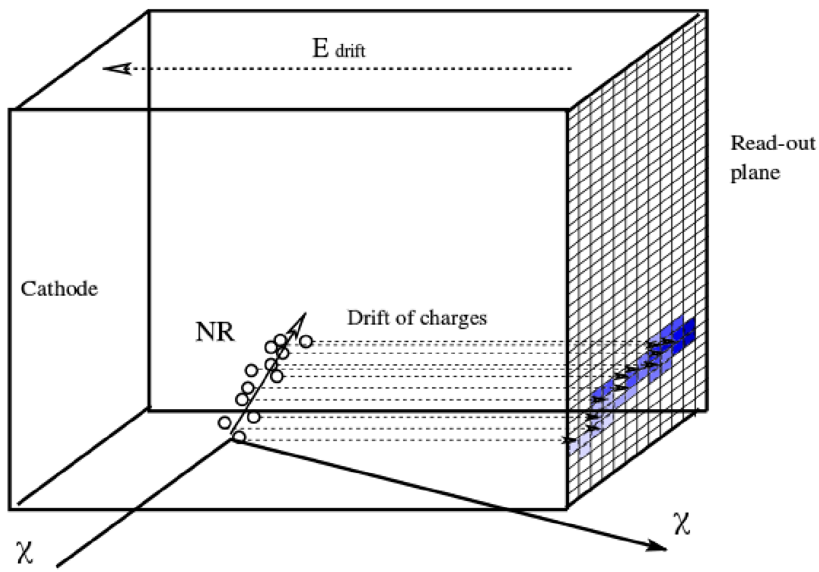

Figure 35. Schematic of a track reconstruction in a directional low-pressure gaseous time-projection chamber (TPC).

- The DRIFT-II experiment [66] running at the Boulby mine in the UK is an example of a low pressure directional detector
- Other directional searches are summarized here [26]

Summary

Figure 36 shows an overview of direct detection results for spin-independent WIMP-nucleon cross sections. The shaded green region represents the region in parameter space which is excluded by current experiments. The orange shaded region represent the

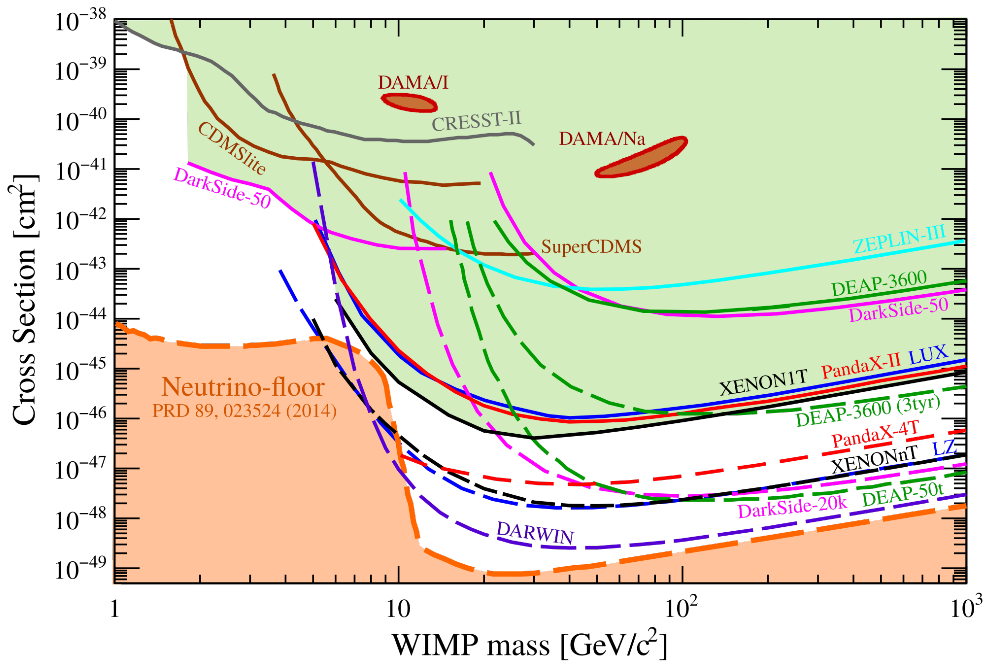

Figure 36. Spin-independent direct detection results: solid curves represent published results while dashed lines are projections for the future. Figure from C. Hasterok.

neutrino floor: the cross sections at which coherent neutrino scattering is an irreducible background.

Figure 37 is a summary of the spin-dependent (neutron coupling on the left and proton coupling on the right) interpretation of the experiments results.

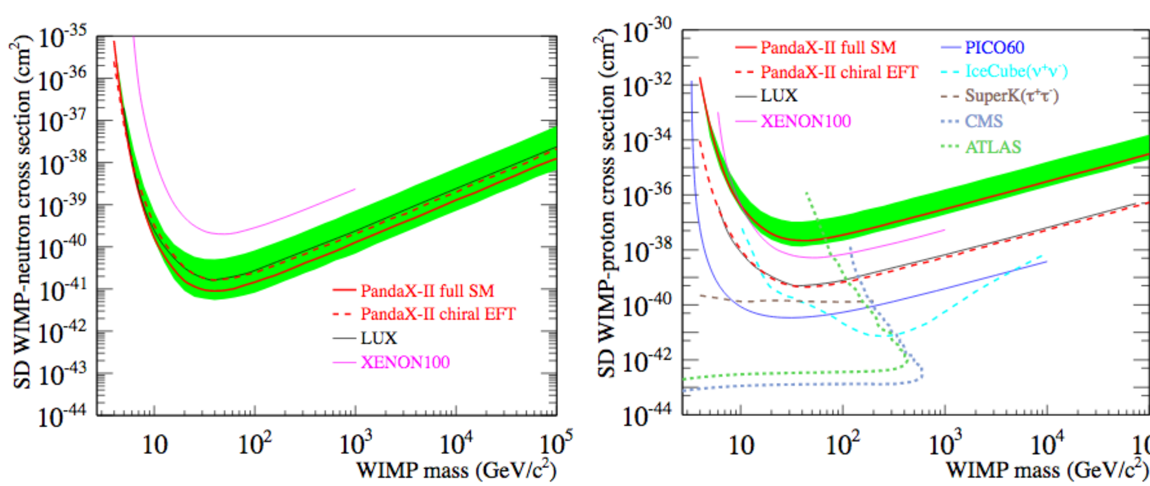

Figure 37. Spin-dependent direct detection results. Neutron coupling is displayed on the left and proton coupling on the right. Figure from PandaX, arXiv:1807.01936.

7. WIMP models

7.1. General considerations

The minimal requirements for building a WIMP model are:

- Ensure DM stability imposing a symmetry which forbids decay of the Dark Matter, i.e. ensure that the presence of only processes involving a even number of DM particles
- Allow for interaction of the DM with SM states.

The WIMP paradigm can be realized in different scenario with different degrees of refinement, from effective field theory, passing through the so-called “simplified models”, through realistic models like the MSSM. See carton in fig. 38.

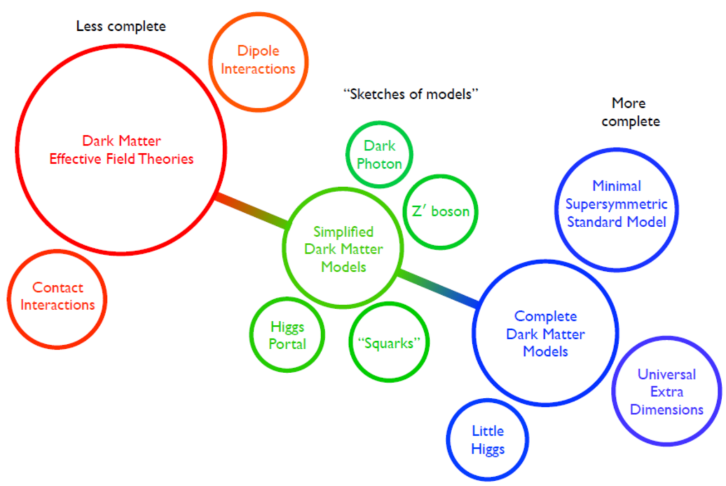

Figure 38. Simple cartoon for possible DM models taken from [67].

Effective field theory is at the moment not so popular since do no provide a reliable description of collider phenomenology (will be discussed in more detail in case of collider searches).

Prototype for WIMP models:

- Minimal Dark Matter [68, 69]: DM is a neutral state of a $SU(2)$ multiplet. It annihilates mostly in gauge bosons (**Notice that a correct assessment of the correct relic density requires considering additional effects, like the so-called Sommerfeld enhancement. These won’t be discussed in the course.)**
- s-channel portals [25]: the DM is a SM singlet and annihilates typically into SM fermions through s-channel exchange of an electrically neutral mediator.
- t-channel portals [25]: the DM annihilates into SM fermions through the t-channel exchange of a mediator

In simple models, the DM relic density can be reliable estimated by the velocity expansion of the thermally averaged annihilation cross-section:

$$\langle\sigma v\rangle \simeq a + \frac{3}{2} b x^{-1} = a + b v^2$$
$$a = \text{s-wave term} = \sigma(s = 4m_\psi^2) \tag{52}$$

$$\Omega \propto \frac{x_f}{\bar{g}_{\rm eff}^{1/2}} \left[a + \frac{3}{4} \frac{b}{x_f} \right]^{-1} \tag{53}$$

Exceptions for the validity of velocity expansion [70]:

- s-channel resonances;
- opening thresold of new annihilaton channels;
- coannihilations;

7.2. Examples of realistic models

Moving to realistic models, equation for a system of particles

In realistic models the DM is part of a new particle sector generally dubbed as "dark" or "hidden" sector. In general one should write a Boltzmann equation for each state of the dark sector of the form:

$$\begin{aligned}
\frac{dn_i}{dt} &= -3Hn_i - \sum_{j=1}^{N} \langle\sigma_{ij} v_{ij}\rangle (n_i n_j - n_i^{\rm eq} n_j^{\rm eq}) \\
&- \sum_{j\neq i} \left[\langle\sigma'_{Xij} v_{ij} \left(n_i n_X - n_i^{\rm eq} n_X^{\rm eq}\right) - \sigma'_{Xji} v_{ij} \left(n_j n_X - n_j^{\rm eq} n_X^{\rm eq}\right) \right] \\
&- \sum_{j\neq i} \left[\Gamma_{ij}(n_i - n_i^{\rm eq}) - \Gamma_{ji}(n_j - n_j^{\rm eq}) \right]
\end{aligned} \tag{54}$$

where $x \in$ SM and:

$$\begin{aligned}
\sigma_{ij} &= \sum_X \sigma(\chi_i \chi_j \to X) \\
\sigma'_{Xij} &= \sum_{X,Y} \sigma(\chi_i X \to \chi_j Y) \\
\Gamma_{ij} &= \sum_X \Gamma(\chi_i \to \chi_j X)
\end{aligned} \tag{55}$$

The symmetry which guarantees the stability of the DM ensures that all the particles of the hidden sector decay into the DM. By further assuming that the decay rates are fast one can solve a single Boltzmann equation for $n = \sum n_i$:

$$\frac{dn}{dt} = -3Hn - \sum_{i,j=1}^{N} \langle\sigma_{ij} v_{ij}\rangle (n_i n_j - n_i^{\rm eq} n_j^{\rm eq}) \tag{56}$$

The scattering of the dark sector states over thermal bath states ensures kinetic equilibrium:

$$\frac{dn}{dt} = -3Hn - \langle \sigma_{\text{eff}} v \rangle (n^2 - n_{\text{eq}}^2) \tag{57}$$

The Boltzmann equation is again reformulated to its simplest version. The annihilation cross-section is, however, now an effective cross-section encoding the interactions of all particles of the Dark Sector. The effective annihilation cross-section is nevertheless dominated by the pair annihilations of the Dark Matter unless some state is very close in mass to the DM. This regime is dubbed coannihilation regime.

Case of study: MSSM

According Supersymmetry each fermion (boson) of the SM has a superpartner which is a boson (fermion). The MSSM is the minimal realization of this idea.

SM field	superpartner	superpartner name
B	$\tilde{B}$	Bino
W	$\tilde{W}$	Wino
g	$\tilde{G}$	Gluino
$\text{H}_{u,d}$	$\tilde{H}_{u,d}$	Higgsino
q	$\tilde{q}$	squark
l	$\tilde{l}$	slepton

Table 1. Summary table with MSSM states.

In order to forbid the decay of the proton one has to impose a discrete symmetry called R-parity [71], under which the SM states are even while the superpartners are odd. This has the consequence that the superpartners can interact only in even number and, more important, the lightest of them (LSP) is stable. The MSSM provides hence a DM candidate if the LSP is an electrically neutral state.

The MSSM provides two WIMP dark matter candidates:

- Sneutrino, superpartner of neutrino;
- Neutralino, combination of Bino, Wino, Higgsino.

The sneutrino is largely excluded by direct detection (see below).

Neutralino:

The MSSM features 4 neutralinos. These are Majorana states:

$$\chi_i = N_{i1}\tilde{B} + N_{i2}\tilde{W} + N_{i3}\tilde{H}_u + N_{14}\tilde{H}_d \tag{58}$$

where N_{ii} are the elements of a suitably defined mixing matrix. Notice the different quantum numbers under $SU(2)$, Bino is a singlet, Higgsinos are doublet, Wino is triplet.

- Bino-like DM: annihilates mostly into fermion pairs through t-channel exchange of sfermions.

- Wino-Higgsino DM: annihilates mostly into W^+W^- through t-channel exchange of charginos (mixture of the charged superpartners of the Higgs and of the W boson).

Connection between DM and Direct Detection

Consider a simple model in which the DM annihilates into a s-channel mediator into quark pairs. Let's further assume that the mass m_ϕ of the mediator is much greater than the DM mass m_χ. The annihilation cross-section can be schematically written as:

$$\langle \sigma v \rangle \simeq \frac{\lambda^2_{\chi\chi\phi}\lambda^2_{qq\phi}m^2_\chi}{m^4_\phi}(a+bv^2) \tag{59}$$

Conversely the scattering cross-section of the DM over nucleons can be schematically expressed as:

$$\sigma^{\mathrm{SI}}_{\chi N} \simeq \frac{\mu^2_{\chi p}\lambda^2_{\chi\chi\phi}}{\pi m^4_\phi}F(\lambda_{qq\phi}) \tag{60}$$

- Requirement of the correct relic density implies a prediction for the Direct Detection signal.
- Absence of signal in Direct Detection puts an upper bound on the DM annihilation cross-section and can eventually rule-out the WIMP paradigm (**Notice this is an oversimplified statement**).

Simple example: Higgs and Z-portal

The correlation between Direct Detection and relic density for WIMPs is shown in some of the simplest models, scalar DM interacting with the Higgs boson or the Z-boson, in fig. 39. The MSSM sneutrinos have direct detection cross-section analogous to the scalar Z-portal and, as evident, is already largely excluded.

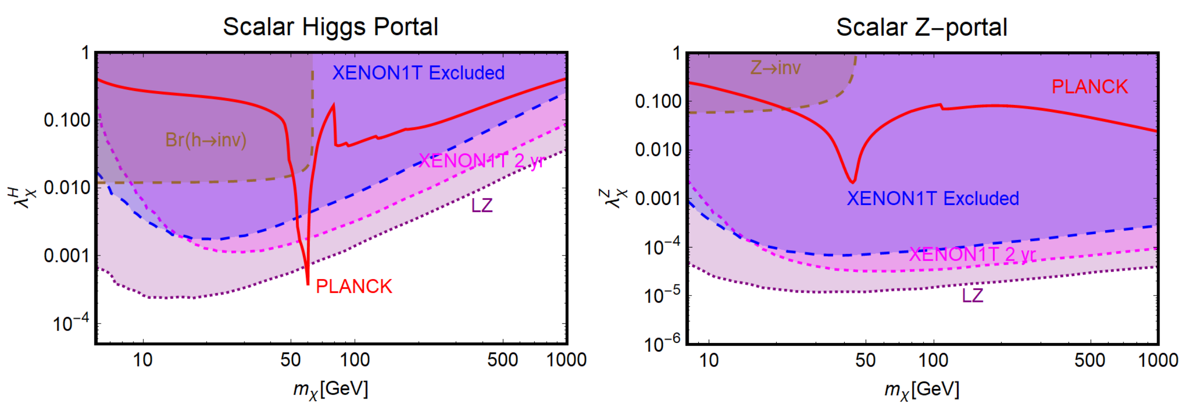

Figure 39. Correct relic density (red contours) against current and future limits from some next future experiments. The figures are taken from [25].

8. Sterile Neutrinos as dark matter

8.1. Motivation

The SM model in its original formulation features only left handed and massless neutrinos. The existence of non zero masses, demonstrated by the observation of neutrino oscillations requires an extension of the SM.

The simplest extension of the SM consists into adding right-handed neutrinos

$$\mathcal{L} = -\frac{1}{2}\overline{\nu}^c_R m_R \nu_R - y_\nu \bar{l}\tilde{H}\nu_R + h.c = -\frac{1}{2}\overline{\nu}^c_R m_R \nu_R - m_D(\bar{\nu}_L\nu_R + \bar{\nu}_R\nu_L) \tag{61}$$

Right-handed neutrinos are SM singlets, hence they can have Majorana mass terms. Simple one flavor example:

$$\mathcal{L} = -\frac{1}{2}\left(\bar{\nu}_L\,\bar{\nu}^c_R\right)\begin{pmatrix} 0 & m_D \\ m_D & m_R \end{pmatrix}\begin{pmatrix} \nu^c_L \\ \nu_R \end{pmatrix} \tag{62}$$

- $m_R = 0$: ν_L and ν_R form a unique dirac state;
- $m_D = 0$: the left and right-handed neutrinos do not mix; we have a massless SM neutrino and a pure sterile neutrino with mass m_R;
- $m_R \ll m_D$: the two states form a pseudo-dirac pair with masses:

$$m_{1,2} \sim m_D \pm \frac{m_R}{2} \tag{63}$$

- $m_D \ll m_R$ (type-I see saw): the mass eigenstates are an almost left-handed neutrino with mass $m_\nu \sim \frac{m_D^2}{m_R}$, identified as the SM neutrino, and an almost right-handed neutrino with mass m_R and coupling with the SM states suppressed by an angle $\theta \sim \frac{m_D}{m_R}$.

Sterile neutrino DM is an extra neutrino state with couplings with the SM suppressed by an extremely small mixing, so that it is stable on cosmological scales. The mixing is nevertheless not set exactly to zero in order to ensure the possibility of experimental tests. Most of models for sterile neutrino DM consider DM masses between few KeV and few tens of KeV:

- Heavier neutrinos would have a fastly increasing decay rate; it would be very difficult to accommodate the stability of DM.
- Lighter neutrinos cannot be DM because of the **Tremaine-Gunn bound** [17]: for fermionic DM, an average phase space density in any DM dominated system (e.g. Dwarf Galaxies) cannot exceed the density given by the Pauli exclusion principle. The Tremaine-Gunn bound imposes that fermionic DM cannot be lighter than 0.3 keV.

8.2. Phenomenology of keV sterile neutrinos

See e.g. [72] for a review.

- Relic density:
  - (i) Dodelson-Widrow Mechanism [73]: DM is produced through oscillations with the SM (active) neutrinos. An approximation of the relic density reads:
  $$\Omega_{\rm DM}h^2 \approx 0.3\left(\frac{\sin^2 2\theta}{10^{-8}}\right)\left(\frac{m_R}{10\,\mathrm{keV}}\right)^2 \tag{64}$$
  where θ is the mixing angle between the DM and the active neutrinos.
  - (ii) Shi-Fuller Mechanism [74]: The Shi-Fuller mechanism is a variant of the Dodelson-Widrow production. DM-active neutrino oscillations are enhanced in presence of a lepton asymmetry (it behaves like the matter potential in the MSW effect) so that the the correct relic density is matched for lower values of the angle. No simple analytic approximation available.
  - (iii) Other more exotic possibilities, e.g. decay of heavier states.

- Bounds from structure formation:
  Brief digression: As already pointed DM plays a relevant role in structure formation. In this context a relevant characteristic of a DM candidate is the so called free streaming length λ_S. During structure formation all the structures which typical length scale below λ_S were erased. DM candidates can be classified according their free-streaming length:
  - Hot Dark Matter (HDM): λ_S much greater that the typical size of the observed structures. The visible Universe would have formed from fragmentation of bigger structures. This possibility is ruled-out by N-body simulations. HDM is experimentally ruled out.
  - Warm Dark Matter (WDM): λ_S of the order of the smallest visible structures (Dwarf galaxies). Very debated and strongly constrained but not ruled out.
  - Cold Dark Matter (CDM): λ_S very small, below the size of the planets. The visible Universe would form from accretion of smaller structures. Possibility preferred by N-body simulations (there are still some puzzles though).

  In the case of thermal relics, i.e. particles which were in thermal equilibrium at Early times, there is a one-to-one correspondence between the DM mass and λ_S:
  - Particles lighter the 0.1-1 keV are HDM;
  - Particles with masses between order of 0.1 and order of 10 KeV are WDM.
  - Heavier particles are CDM.

  If the DM is not a thermal relic (like most models of sterile neutrinos) λ_S depends on the DM distribution function and, hence, on its production mechanism. Dodelson Widrow and Shi-Fuller mechanisms give WDM candidates:
  - Limit from phase space density of Dwarf Galaxies (refinement of the Tremaine-Gunn bound) $m_R \gtrsim 2\,\mathrm{keV}$;

  - Limits from the count of Milky Way satellites;
  - Limits from Ly-α forest [75].

- Experimental searches: keV DM can decay into 3 DM neutrinos or a SM neutrino and a photon. The rate of the latter process is:

$$\Gamma_{\nu_R \to \gamma\nu} = \frac{9\alpha G_F^2}{1024\pi^4} \sin^2(2\theta) m_R^5 \tag{65}$$

  This decay rate gives as signature X-ray lines which are searched for experimentally. There is a non confirmed hint for the detection a line that could be interpreted as the decay of a sterile neutrino with mass 7 keV [76, 77] (**Notice that the DM interpretation is very controversial**). Otherwise one should consider limits expressed in terms of the mass of the DM and the mixing angle θ.

  Examples of the combined constraints on sterile neutrino DM are given if fig. 40.

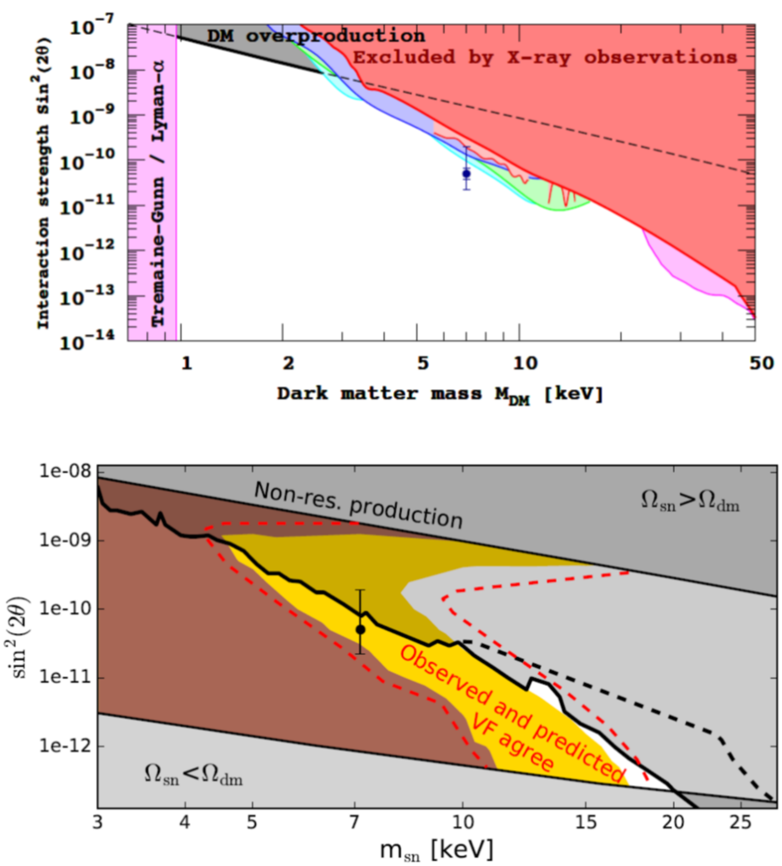

Figure 40. Upper panel: combined constraints on sterile neutrino DM assuming only Dodelson-Widrow production of dark matter. The blue point represents the fit of the 3.5 keV signal. Very conservative limits from structure formation are assumed. Lower panel: analgous plot for the Shi-Fuller production (black contour). Very aggressive limits from structure formation are assumed. Figures from [72] and [78], respectively.

9. Axion dark matter

9.1. Motivation: the strong CP problem

The symmetry of the standard model allows for an additional term:

$$\mathcal{L} = \theta \frac{\alpha_s}{8\pi} G_a^{\mu\nu} \tilde{G}_{a\mu\nu} \tag{66}$$

The origin of this term is connected to the vacuum structure of the QCD. This terms violates CP. If $\theta \neq 0$ electromagnetic moment of the axion is induced. The absence of experimental evidence imposes the constraint:

$$|\theta| \leq 10^{-10} \tag{67}$$

How one can achieve a small possibly vanishing θ parameter?

Introduction of a $U(1)_{\mathrm{PG}}$ global symmetry spontaneously broken. The axion a is the Nambu-Goldstone boson associated to the breaking and transforms as:

$$a \to a + \alpha f_a \tag{68}$$

The SM Lagrangian is hence augmented as:

$$\mathcal{L}_{\mathrm{tot}} = \mathcal{L}_{\mathrm{SM}} + \theta \frac{\alpha_s}{8\pi} G_a^{\mu\nu} \tilde{G}_{a\mu\nu} - \frac{1}{2}\partial_\mu a \partial^\mu a + \mathcal{L}_{\mathrm{int}} + \frac{a}{f_a}\frac{\alpha_s}{8\pi} G_a^{\mu\nu} \tilde{G}_{a\mu\nu} \tag{69}$$

where $\mathcal{L}_{\mathrm{int}}$ is a interaction lagrangian between the axion and SM fields which depends on the UV completion. The axion field forms with the θ term an effective dynamical θ parameter $\theta_{\mathrm{eff}} = \theta + \frac{a}{f_a}$. The QCD potential is such that its minimum is at $\theta_{\mathrm{eff}} = 0$. The coupling term with the gluon generates a mass term for the axion. Recent computation give [79]:

$$m_a = 57 \left(\frac{10^{11}\,\mathrm{GeV}}{f_a} \right) \mu\mathrm{eV} \tag{70}$$

The coupling with the gluon is dimension-5, hence is an effective coupling. There are different possible UV implementations. The more popular are the KSVZ (most minimal realization) and the DFSZ. The axion is part of a complex field:

$$\sigma = (v_{\mathrm{PQ}} + \rho) \exp\left[\frac{a}{f_a}\right] \tag{71}$$

where v_{PQ} is the vev which breaks the PQ symmetry. The different UV models differs from the ways in which the coupling with the gluons is realized. In general an additional coupling between the axions and the photons of the form:

$$\mathcal{L}_{a\gamma\gamma} = \frac{c_{a\gamma\gamma}}{f_a} a F^{\mu\nu} \tilde{F}_{\mu\nu} \tag{72}$$

More model dependent couplings with the SM fermions are induced as well.

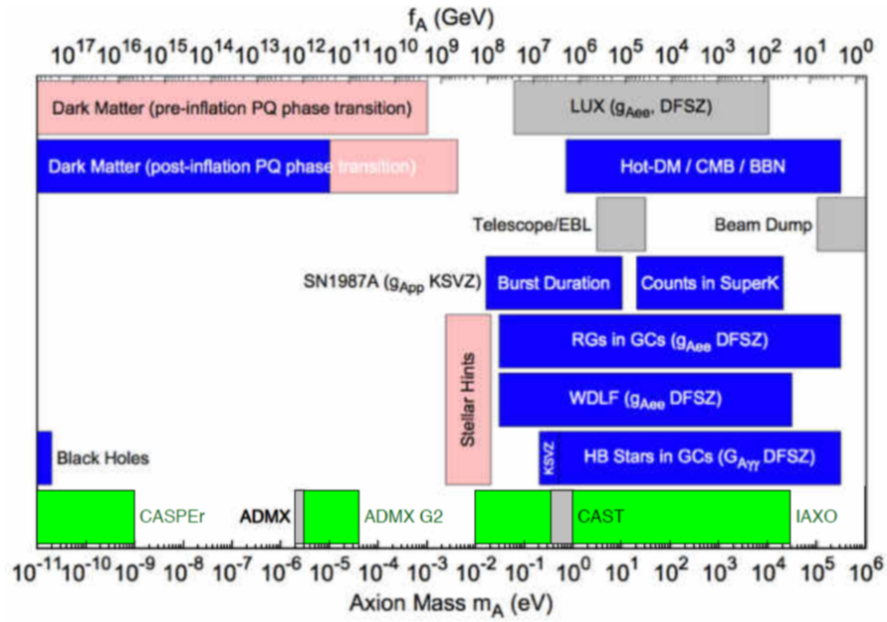

Figure 41. Overview, taken from [80] of axion parameter space. The boxes represent regions in which the axion can be DM with the correct relic density, region excluded by astroparticle constraints as well as region which can be probed bw some current and future planned experiments.

An overview of the parameter space of QCD axion models, including some constraints as well as the projected experimental sensitivity (see next subsections) is shown in fig. 14.

All the interactions of the QCD axions with SM fields are suppressed by the parameter f_a. If f_a is big enough the axion becomes stable on cosmological scales and hence a potential DM candidate.

9.2. Production in the early Universe

Axion DM is very light and with very suppressed couplings with the SM. Several mechanisms have been proposed for its production in the Early Universe. The most popular is the so called misalignment mechanism. The axion is treated as a classical field described by the following equation:

$$\frac{d^2\theta}{dt^2} + 3H\frac{d\theta}{dt} - \frac{1}{a^2(t)}\nabla\theta = -\frac{1}{f_a^2}\frac{\partial}{\partial\theta}V \tag{73}$$

V is the potential of the axion:

$$V = \chi(T)(1 - \cos\theta) \tag{74}$$

The axion has a time dependent mass term $m_a(T) = \frac{\sqrt{\chi(T)}}{f_a}$. At Early times the PQ symmetry is unbroken. At later times spontaneous breaking occurs. The mass term

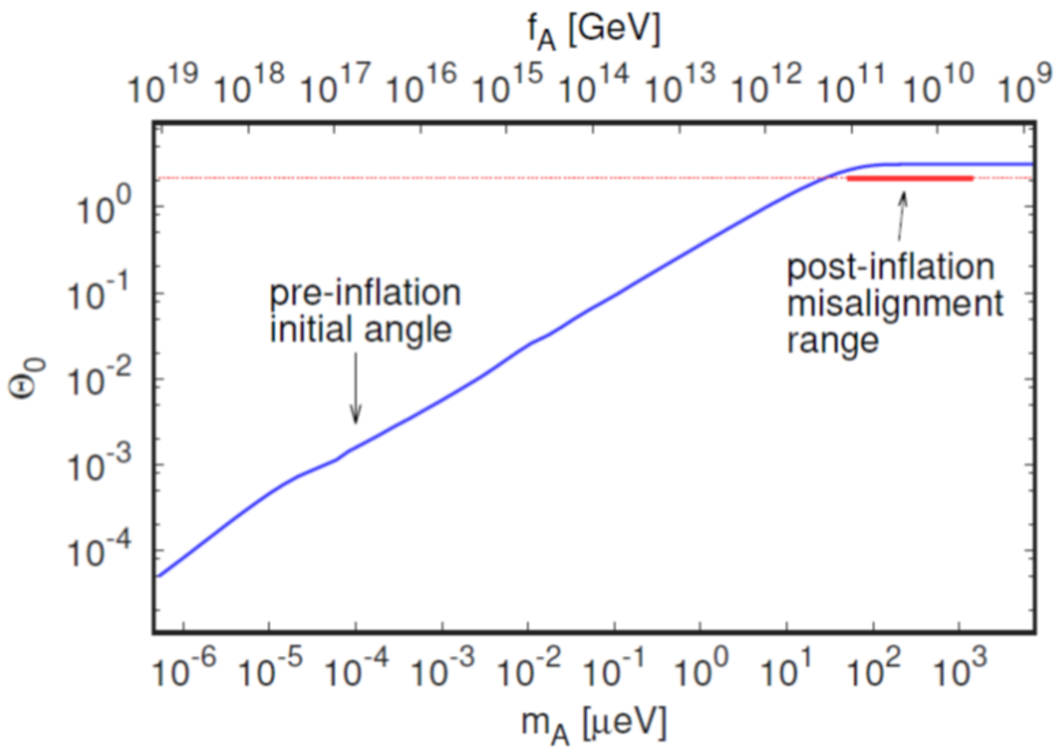

Figure 42. Parameter space corresponding to the correct DM relic density according to the misalignment mechanims. The figure is taken from [81].

(r.h.s of the equation) is negligible and the axion field is frozen at an initial configuration θ_0. When the time dependent mass term overcome the Hubble expansion parameter, i.e. $m_a(T) \simeq 3H(T)$ the axion field oscillate around the minimum of the effective potential. It is possible to show that the oscillation classical axion field is equivalent to a coherent state of many non relativistic axions. Even if very light, axion behaves as CDM. Its relic density depends on f_a, θ_0 and whether the breaking of the PQ symmetry occurs before or after inflation. The parameter space corresponding to the correct DM relic density is shown in fig. 42.

9.3. Axion couplings and axion-like particles

- Reminder: In QCD there is no reason to conserve CP but experimental bounds on the neutron electric dipole moment indicate very small CP violation. In 1977 Peccei and Quinn postulated a new symmetry to solve this issue
- The axion particle appears when the symmetry is spontaneously broken at the scale f_a, axion mass and couplings are: m_a, $g_{aii} \propto 1/f_a$
- Couplings of axions to matter: g_{aNN}, $g_{a\gamma\gamma}$ and g_{aee} represent the coupling of axions to nucleons, photons and electrons, respectively, in processes like Compton, Primakoff and Bremstrahlung

- All processes have in common the coupling strength: $g_{aii} \sim m_a \sim 1/f_a$
- Originally it was thought that the scale of breaking lies close to the electroweak scale ($\sim$ 250 GeV). Early constrains from accelerator experiments ruled out this hypothesis $\rightarrow$ 'invisible axion'
- **Axion-like particles**: Particles described by an analogous lagrangian as the QCD axion. They do not solve the strong CP-problem though. In their case m_a and f_a are independent parameters.

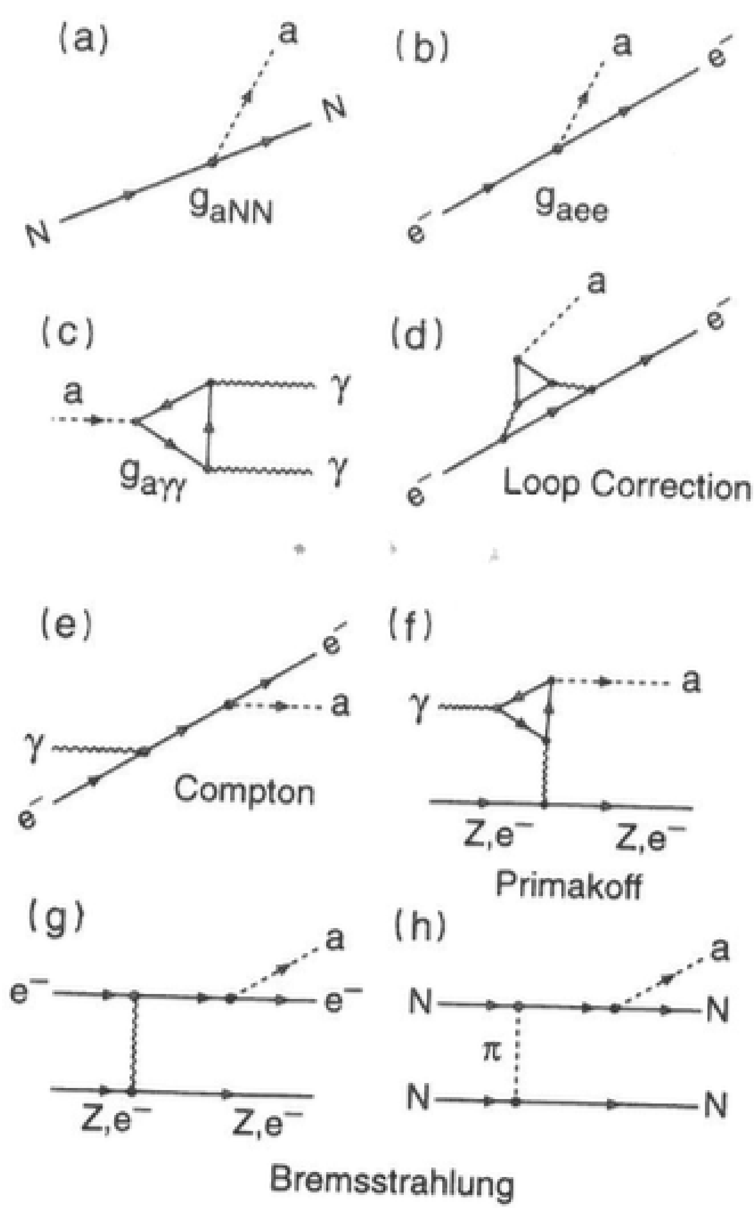

Figure 43. Feynman diagrams for the coupling of axions to normal matter, as well as the dominant axion emission processes in stars. Figure from 'Particle astrophysics' book.

9.4. Astrophysical constrains

- Due to the small coupling with normal matter, axions can significantly influence the evolution of stars
- Astrophysics constrains use an energy-loss argument: properties of stars would change if they lose too much energy via axion production [82]
- Constrains from solar age, globular cluster stars, SN 1987A and telescopes
- Figure 44 shows atrophysical constrains. The lighter the regions, the more model dependent are the constrains. Regions uncovered by bars are still allowed axion masses.

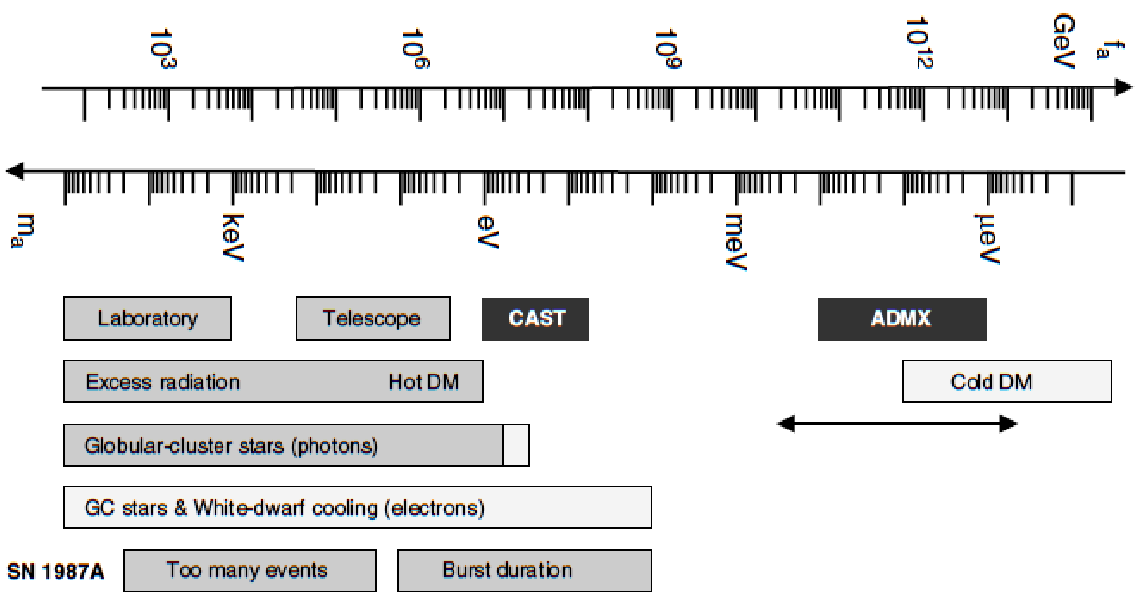

Figure 44. Summary of astrophysical and cosmological axion limits. The black sensitivity bars indicate the search ranges of the CAST solar axion search and the ADMX search for galactic dark matter axions. Light-grey exclusion bars are very model dependent. Figure from G. Raffelt, *Astrophysical axion bounds*, Lect. Notes Phys. 741 (2008) 51 [82].

- Telescope limits → from absence of signal of axion decay $a \to \gamma\gamma$, see also figure 49
- Experimental constrains are described later in this chapter

9.5. Axion search experiments

'Laboratory' constrains

- Search for rare decays like $\pi^+ \to a e^+ \nu_e$ ruled out $m_a > 1\,\mathrm{MeV}$

- Search for axion production in reactions like $p + N \to a + X$ or $e^- + N \to a + X$ ruled out $m_a > 50\,\mathrm{keV}$

Axion haloscopes: measurement of axions from the Milky Way

- These axions cannot be detected via their decay because the lifetime is very large $\tau_a \sim 10^{42}\,\mathrm{y}$
- Detection method: conversion via a strong magnetic field
- The apparatus would be a microwave cavity. In this type of experiment the instantaneous total energy (mass and kinetic energy) of the axion is recorded as signal
- The detection efficiency is related for instance to the strength of the magnetic field but also to properties of the cavity, its volume and the fraction of the power that it is coupled to the antenna
- **ADMX**: Axion Dark Matter eXperiment [83] is a device of this type based in the US. It has a magnet of 8 T for a cavity keep at 1.5 K to minimize the noise. The sensitivity of the experiment is at $\sim 2\,\mu\mathrm{eV}$
- Figure 45 shows results from 2018 by the ADMX experiment

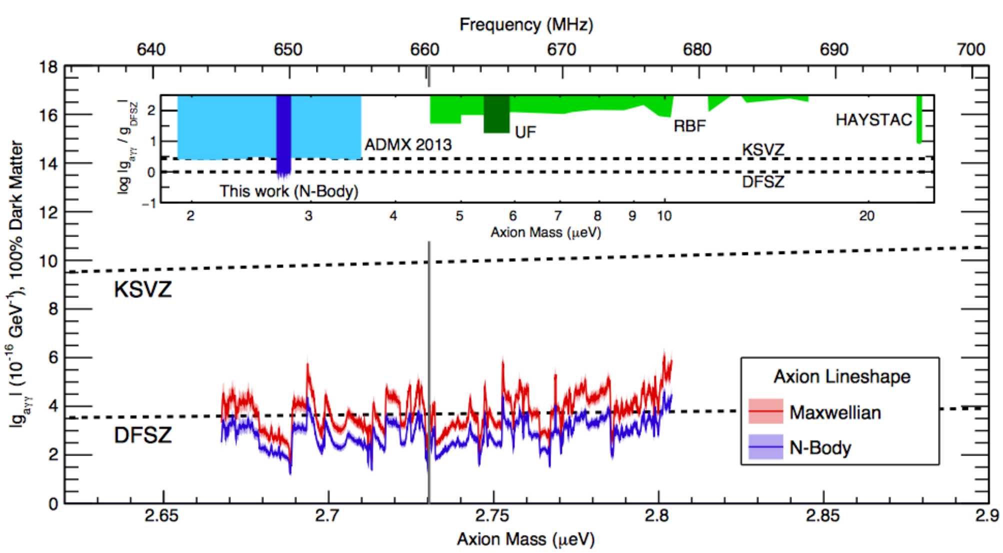

Figure 45. Exclusion limit (90% CL) for axion mass and axion coupling $g_{a\gamma\gamma}$ for two different halo models. Figure from ADMX Collaboration, PRL. 120 (2018) 151301 [83].

Axion detection via axio-electric effect:

- Effect similar to the photoelectric effect
- Underground WIMP detectors are used to search for mono-energetic lines in their background spectrum

- Note that these axions would have energies on keV scale and are ALPs → they do not solve the CP problem necessarily
- Figure 46 shows current upper limits on the coupling of ALPs to electrons g_{Aee}

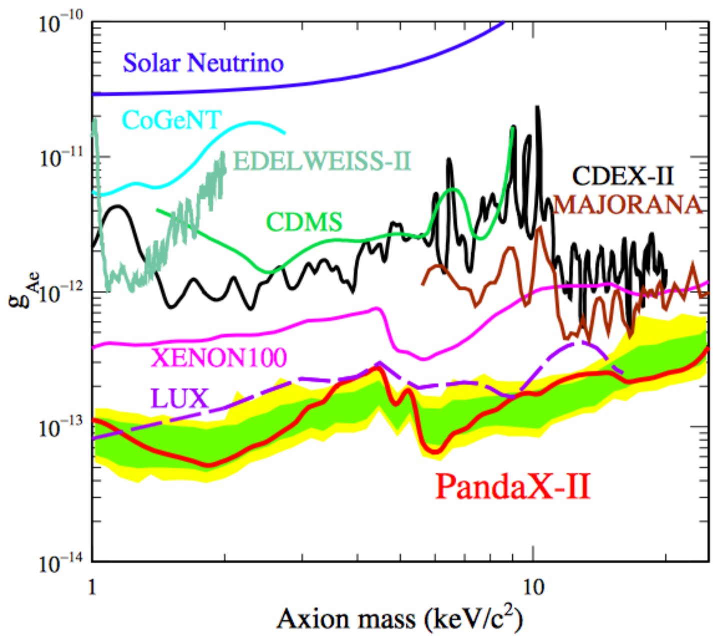

Figure 46. Constrains (90% CL) on axion mass and axion coupling g_{aee} from the PandaX experiment (red line) compared to other existing experimental results. Figure PandaX Collaboration, PRL 119 (2017) 181806 [84]

Solar axions

- Axions could be produced inside the Sun via Primakov conversion.
- Typical energies are in the $(1-10)$ keV regime, corresponding to the temperatures inside the Sun
- These axions can stream out and can be detected in Earth-based instruments
- Crystalline underground detectors can use the characteristic Bragg pattern signature to search for these axions

Axion helioscopes

- Conversion of solar axions into low-energy X-rays as they pass through a magnetic field
- A magnet pointing to the Sun is used to convert the axions and an X-ray detector would record the corresponding signal
- Conversion probability related to the magnetic field and the length of the magnet, see figure 47 for a scheme of this type of detectors. There is an additional form factor F that takes into account the coherence of the conversion process

- There have been several experiments of this type. An example is CAST located at CERN. It uses an LHC dipole prototype magnet of 9 T and 9.3 m length. Micromegas detectors are used for the X-ray detection. The result of this experiment can be seen in figure 49. Most recent results (2017) are published here [85]
- IAXO is a planned future experiment (see the proposed design on the right side of figure 47. The envisioned magnet will have 25 m length and 2.5 T

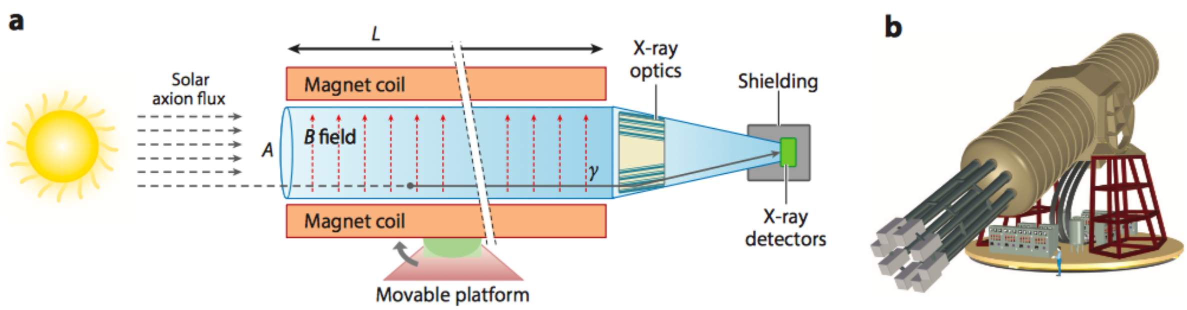

Figure 47. A) Scheme of a axion helioscope with X-ray focusing. b) Proposed design for the future IAXO experiment. Figures from Graham *et al.*, Ann. Rev. Nucl. Part. Sci. 65 (2015) 485 [86]

'Light shinning through the wall' experiments:

- These type of experiments look for WISPs
- WISPs: general name for Weakly Interacting Slim Particles which include ALPs but also other particles like hidden photons
- A very strong light source from a laser is used as source. In order to enhance the conversion probability from the photons to the WISP, the light is inside a Fabry-Perot cavity
- Behind a light-blocking barrier, a second cavity is used for the reconversion of the WISP to photons
- Both cavities are inside magnets
- The probability for $\gamma \to \phi \to \gamma$ oscillation is related to the effective WISP coupling and to the power-build-up factors of both the production and the regeneration cavities [86]
- ALPS II is an important example of this type of experiment. It is located inside the HERA tunnel at DESY (Germany) and uses the HERA magnets for WISP production and regeneration [87]

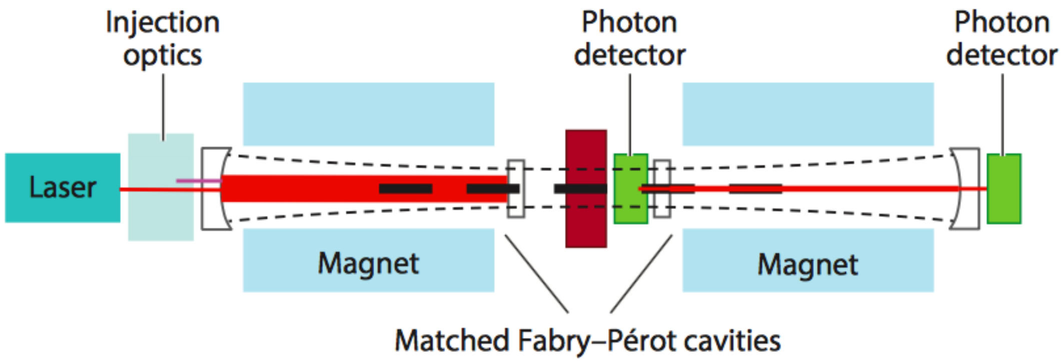

Figure 48. Principle of 'light shining through walls' experiments. Figure from Graham *et al.*, Ann. Rev. Nucl. Part. Sci. 65 (2015) 485 [86]

- Figure 49 summarizes the results of several experiments in the parameter space of axion mass and coupling to photons $g_{a\gamma\gamma}$ [86]. Note that this summary figure is from 2015 and some more sensitive results have been released meanwhile

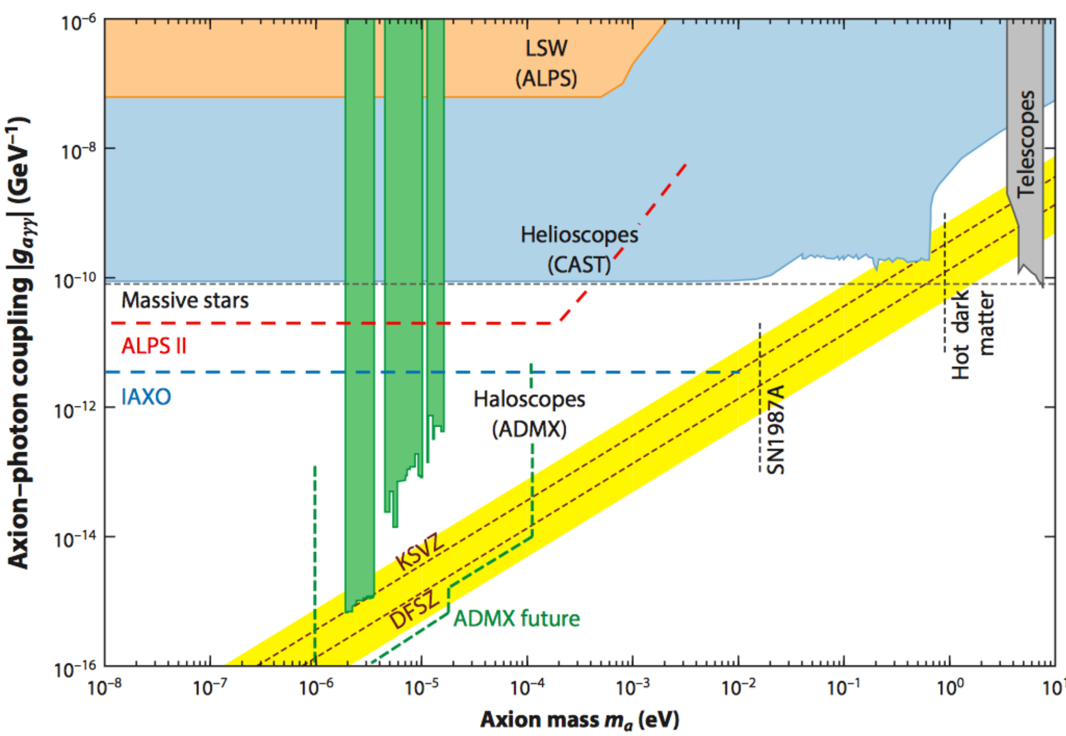

Figure 49. Constrains of axion/axion-like particles (ALPs) coupling to photons and the projected sensitivity of future deveices as function of their mass. Figure from Graham *et al.*, Ann. Rev. Nucl. Part. Sci. 65 (2015) 485 [86]

10. Indirect detection

This section is mostly based on the following references:[88, 89].

Indirect detection relies on the searches of the products of DM annihilation or decays occurring at present times. The main observable is represented by the flux $\frac{d\Phi_i}{dE_i}$ of the i-th product. This flux depends on the DM annihilation cross-section $\langle\sigma v\rangle$ or decay rate $\Gamma_{\rm DM}$ and suitable astrophysical inputs. This flux should be compared with a background, represented either by secondary products of interaction of cosmic rays or by astrophysical sources like pulsars. A DM event would be represented by an excess of events with respect to the prediction of the background. In absence of such an excess one can put limits on the DM annihilation or decay rate into the channel leading to the products looked for in experiments.

Three main kind of products are currently searched:

- Photons: γ-rays or X-rays;
- Antimatter: mostly positrons and antiprotons.
- Neutrinos;

10.1. Locations of indirect signals

DM Indirect signals can be looked for in different locations. No location is ideal, each has pro and contra. Combination of different searches potential solution.

Notable locations:

Galactic Center (GC):
PRO: very strong signal; CONTRA: strong on poorly know background;
CONTRA: not complete knowledge of the DM distribution at the GC.

Dwarfs Spheroidal Galaxies (DSph):
PRO: DM dominated objects; optimal signal/background;
CONTRA: weaker signal as the GC;
CONTRA: Astrophysical uncertainties;

Neutrinos can be looked in a special location; i.e. the SUN.

10.2. Signal production

Photons: Photons can be prompt, i.e. photon signal coming directly from the DM source, or can come from Inverse Compton or synchrotron energy loss processes. We will not discuss the latter in detail.

We have to distinguish photons coming from our Galaxy and from extra Galactic sources. For photons from galactic sources the flux at source practically corresponds with the one at Earth. The expression is particularly simple:

$$\frac{d\Phi_\gamma}{dEd\Omega} = \begin{cases} \frac{\langle \sigma v \rangle}{8\pi m_{\rm DM}^2} \sum_f Br_f \frac{dN_\gamma^f}{dE} \int \rho(r)^2 dr & \text{Annihilations} \\ \frac{\Gamma}{4\pi m_{\rm DM}^2} \sum_f Br_f \frac{dN_\gamma^f}{dE} \int \rho(r) dr & \text{decays} \end{cases} \tag{75}$$

the sums run over the allowed annihilation final state/decay channels. $\frac{dN_\gamma^f}{dE}$ represent the number of photons produced in a single annihilation/decay process in the state f.

Prompt photon signals can be of two types: continuum and lines. Continuous signal arises for example from hadronization processes following the DM annihilation into pairs of SM quarks or gauge bosons, dN_γ^f/dE is a complicated function which can be determined through specialized numerical codes. Photon lines are arise when the DM can annihilate/decay directly into photons, e.g. decay of the sterile neutrino $\nu_s \to \nu\gamma$. In this case:

$$\frac{dN_\gamma^f}{dE} = \begin{cases} \delta(E - m_{\rm DM}) & \text{Annihilation} \\ \delta(E - m_{\rm DM}/2) & \text{Decay} \end{cases} \tag{76}$$

In the case of extragalactic photons the expressions above should be corrected taking into account eventual absorption of photons and their redshift z:

$$\frac{d\Phi}{dE} = c\frac{1}{E_\gamma} \int dz' \frac{1}{H(z')(1+z')^4} J_{\rm EG} \exp\left(-\tau(E_\gamma, z')\right) \tag{77}$$

with H being the Hubble expansion parameter and τ the optical depth.

$$J_{\rm EG} = E_\gamma(1+z') \begin{cases} \frac{1}{2}\left(\frac{\rho(z')}{M_{\rm DM}}\right)^2 \sum_f \langle \sigma v \rangle \frac{dN_\gamma^f}{dE} & \text{Annihilation} \\ \frac{\rho(z')}{M_{\rm DM}} \sum_f \langle \sigma v \rangle \frac{dN_\gamma^f}{dE} & \text{Decay} \end{cases} \tag{78}$$

Positrons: Contrary to photons the fluxes of positrons at source and at Earth are sensibly different. Positrons interact with the (irregular) galactic fields. Moreover they lose energy through inverse compton and synctroton radiation. The propagation of positrons can be described as a diffusion processes occurring withing a cilinder of heigh $2L$ and radius R which approximately describes our Galaxy. The corresponding equation can be written as:

$$\frac{df}{dt} - \nabla(K(E,x)\nabla f) - \frac{\partial}{\partial E}(b(E,x)f) = Q(E,x) \tag{79}$$

where $\frac{d\Phi_e}{dE} = \frac{v_e}{4\pi} f$. The terms in the equation represent:

$$b = \text{Energy loss}$$

$$K = \text{Diffusion} = K_0 \left(\frac{E}{\text{GeV}}\right)^\delta$$

$$Q = \text{Source} = \begin{cases} \frac{1}{2}\left(\frac{\rho}{M_{\rm DM}}\right)^2 \langle \sigma v \rangle \sum_f Br_f \frac{dN_e^f}{dE} & \text{Annihilation} \\ \frac{\rho}{M_{\rm DM}} \Gamma \sum Br_f \frac{dN_e^f}{dE} & \text{Decay} \end{cases} \tag{80}$$

Antiprotons: Antiprotons are similarly described by a diffusion equations. There are additional terms:

$$\frac{\partial f}{\partial t} - K\nabla^2 f + \frac{\partial}{\partial z}(\text{sign}(z) f V_{\text{conv}}) = Q - 2L\delta(z)(\Gamma_{\text{ann}} + \Gamma_{\text{non-ann}}) \tag{81}$$

where $\frac{d\Phi}{dk} = \frac{v_p}{4\pi} f, k = E - m_p$. In the case of antiprotons besides diffusion, we have convection, which tends to wipe-away antiprotons with velocity V_{conv}, and interactions between the antiprotons and the galactic medium. These are distinguished into interactions which annihilate antiprotons, with rate Γ_{ann}, or cause only energy loss, $\Gamma_{\text{non-ann}}$.

Neutrinos from the Sun:

DM can be trapped, because of scattering with its elements, and accumulate in the Sun getting a sizable annihilation rate. Among the production only neutrinos can escape from the Sun.

The capture rate of the DM in the Sun can be written as:

$$C = \sum_i \int_V dV \int_0^{u_{\max}} du \frac{f(u)}{u} w \Omega_i(\omega) \tag{82}$$

where the sum runs over the elements. $\omega = \sqrt{u^2 + v^2}$ with v being the escape velocity at the interaction point. Ω is the capture probability and depends on the DM scattering rate on the i-th element. The number of trapped of DM particles is described by the following equation:

$$\frac{dN}{dt} = C - C_A N^2 \tag{83}$$

with C_A related to the DM annihilation rate by $\Gamma_A = \frac{1}{2} C_A N^2$. In most of case one can assume that a present times the annihilation and capture rates are in equilibrium, then $dN/dt = 0$ so $\Gamma_A = \frac{1}{2} C$. The flux of neutrinos from the Sun is given by:

$$\frac{d\Phi_\nu}{dE} = \frac{\Gamma}{4\pi d^2} \sum_f Br_f \frac{dN_\nu^f}{dE} \tag{84}$$

with d being the Earth-Sun distance. In the case of equiblibrium between annihilation and capture rate the flux of neutrinos can be expressed in terms of the DM scattering cross-section.

10.3. Particle propagation and overview of technologies

- Neutral particles point to the source where they were produced $\rightarrow$ pointing. While neutrinos have a negligible absorption during propagation, for gammas the propagation has to be considered only for very high energies or very large distances
- Charged particles ($e^-, e^+, p, \overline{p}$) are deflected in interstellar magnetic fields
- Detector technologies:
  - High energy neutrinos (from $\sim$GeV to 100 TeV) $\rightarrow$ large ν-detectors

  – High energy ($E_\gamma > 100\,\mathrm{GeV}$) gamma-rays → Cherenkov imaging telescopes
  – Low energy ($20\,\mathrm{MeV} < E_\gamma < 100\,\mathrm{GeV}$) → ballon or satellites, e.g. Fermi
  – X-rays → X-ray satellites as XMM-Newton or Chandra
  – Charged particles → at satellites, e.g. Pamela, Fermi, AMS

10.4. Detection of indirect signals

10.4.1. Searches using neutrinos

- Target and detection medium are the same (water or ice)
- Neutrino interactions with target particles/nuclei
- Cherenkov photons emitted by the movement of charged particles are recorded with large-area photosensors
- **Ice-Cube detector** at the south pole (see figure 50 left), $E_\nu \sim (0.1 - 100)\,\mathrm{TeV}$

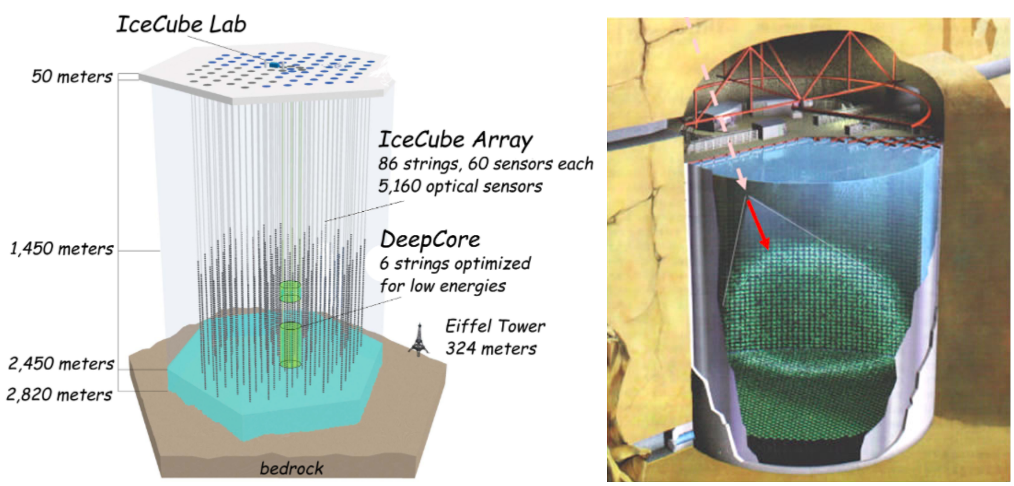

Figure 50. (Right) Schematics of the IceCube detector. Figure from *Into the Ice: Completing the IceCube Neutrino Observatory*, Berkeley Lab. (Left) Schematics of the SuperKamiokande detector. Figure from SuperKamiokande homepage.

- Main background sources: Muons, which are suppressed by looking at particle traces 'from below', and atmospheric neutrinos, irreducible but their spectrum is well known and decreases with increasing energy
- Experimental uncertainty mainly from optical-modules efficiency and photon propagation in ice
- Example of results from PRD 88 (2013) 122001: upper limits on thermally averaged cross section for searches at dwarf spheroidals, Andromeda and galaxy clusters
- Figure 51 shows the results of this publication, showing explicitly the dependence on the source, the annihilation channel, the astrophysical uncertainties and the effect of considering boost factors due to substructures, i.e. sub-haloes.

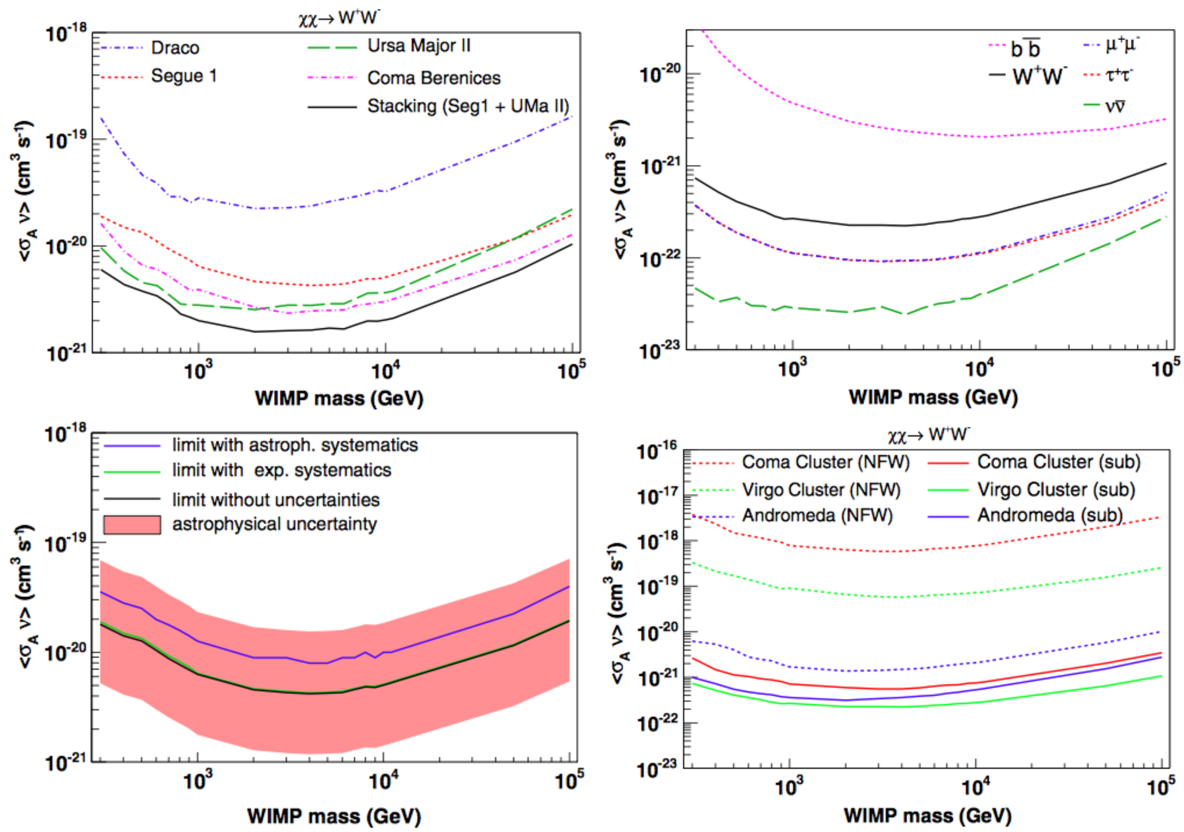

Figure 51. IceCube searches for self-annihilating dark matter. Top left: upper limits for annihilation into W^+W^- in dwarf galaxies. Top right: upper limits for the Virgo cluster for annihilation into $b\bar{b}$, W^+W^-, $\tau^+\tau^-$, $\mu^+\mu^-$, and $\nu\bar{\nu}$. Bottom left: upper limit for Segue 1 for annihilation into W^+W^-. Bottom right: upper limits (W^+W^- annihilation) assuming a pure NFW profile (dashed) and taking into account substructures within halos (solid). Figures from IceCube collaboration, Phys. Rev. **88** (2013) 122001 [90].

- Note that there are also searches for DM annihilation producing neutrinos after the capture of the DM particles in the Sun.
- The Super-Kamiokande detector [91] has, for instance, carried out such searches. The upper limit on the neutrino flux from the Sun can be converted into a limit on a WIMP-nucleon cross-section

10.4.2. Gamma detection in Cherenkov telescopes

- Detection of high energy gamma-rays with energies $\sim (0.05 - 50)$ TeV
- The atmosphere is the target and calorimeter at the same time
- Cherenkov light from particle-showers (figure 53)
- Imaging technique: image reconstructed in the camera (see examples in figure 52). A muon-like event is a ring, a hadron-like shower is an irregular bump and a gamma-like shower is a 'more regular' ellipse.

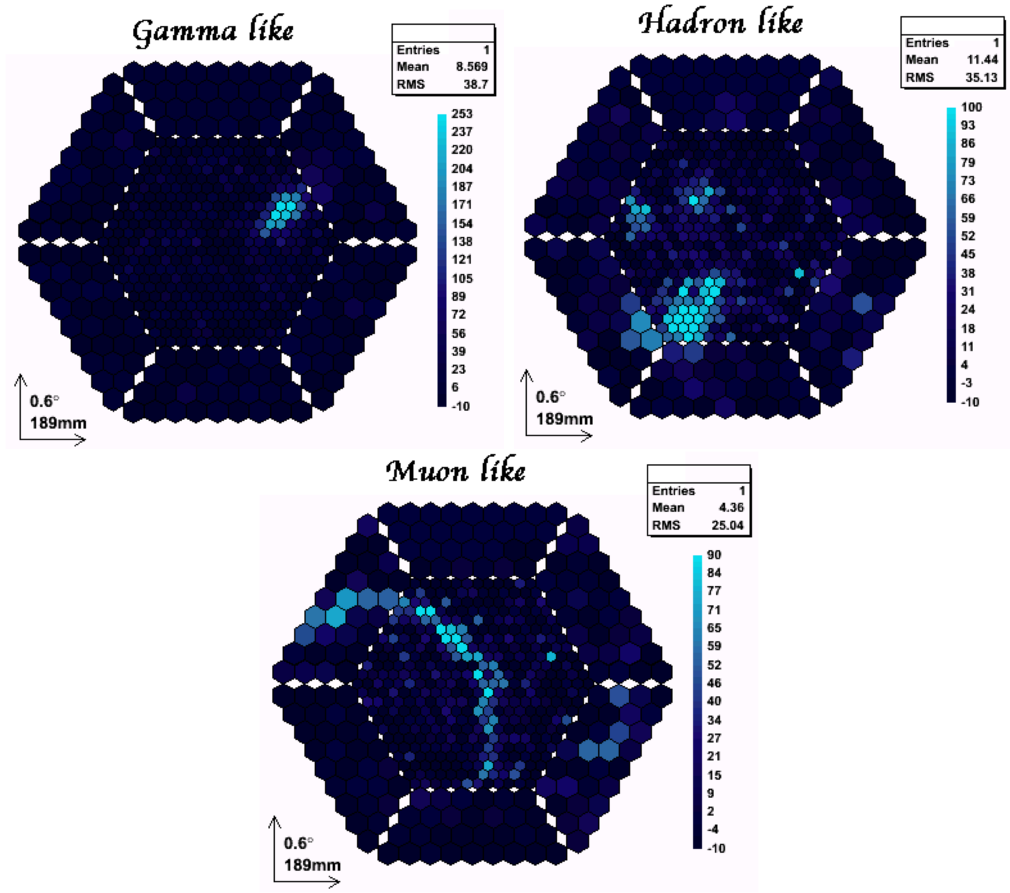

Figure 52. Examples of signals in one of the MAGIC Chrenkov telescopes. Figures from the MAGIC Collaboration (homepage).

- Background is mainly from protons. 99% of the cosmic rays are protons. The shower shape is used to reduce this background
- Electrons from cosmic rays make $\sim 10\%$ of the gamma-like events $\rightarrow$ irreducible
- Direct signal production $\chi\chi \rightarrow \gamma\gamma$, γZ, Bremsstrahlung of charged particles and decay of hadrons, Bremsstrahlung of one of the internal particles in the annihilation diagram and decay (for example $\chi \rightarrow \gamma X$)
- Secondary radiation by e^-e^+ produced in the annihilation: Inverse Compton scattering onto CMB, star light and Infrared light, Bremsstrahlung and synchrotron emission
- Instruments:
  - Veritas in southern Arizona (US), 4×12 m optical reflectors, 2 600 m above see
  - MAGIC in La Palma (Spain), 2×17 m reflectors, 2 400 m above see
  - HESS in Namibia, 4×13 m and one 28 m reflectors, 1 800 m above see

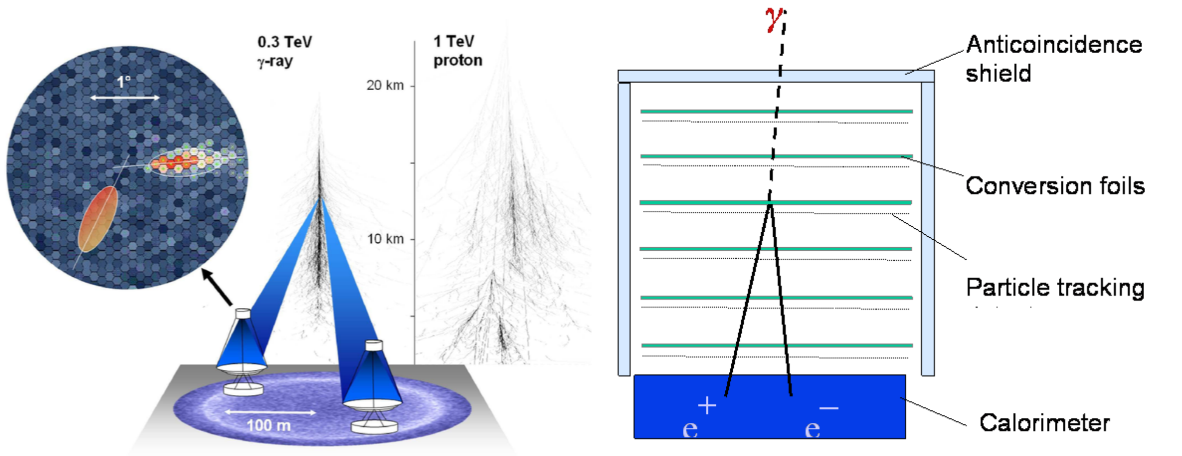

Figure 53. (Left) Schematics of a imaging Cherenkov telescope. Figure from Hinton & Hofmann, Annu. Rev. Astroohys. 47 (2009) 523. (Right) Scheme of the the FermiLAT instrument. Figure from Fermi homepage.

10.4.3. Gamma detection by satellites

- The measurement of gamma rays at satellites is sensitive to lower γ-energies that are not absorbed by the atmosphere. However, in general those detectors have an smaller volume and therefore are also limited on measuring high γ-ray energies.
- **Fermi-LAT detector** (see figure 53, right), an imaging high-energy γ-telescope in orbit since 2008 (1 orbit in 96 min)
- The energy range covers from $E_\gamma \sim (10\,\text{MeV} - 300\,\text{GeV})$

- Detector construction:
  - Anticoincidence detector (to select neutral particles)
  - Tungsten conversion foil (target for γs)
  - Silicon strips (for tracking)
  - CsI calorimeter (measurement of energy)
- The device measures both energy and direction of the γ-ray particle
- Volume of $0.72\,\text{m} \times 1.8\,\text{m}^2$, 2.8 tons and 650 W power consumption
- Needs to be calibrated at particle beams (CERN, SLAC and GSI)

- Fermi collaboration has set limits on $< \sigma_A v >$ from searches in the galactic halo (continuum and line-like), galaxy clusters and dwarf spheroidals. The latter are the most constraining results so far.
- Galactic center signal indication:
  - First seen in 2011: Hooper & Goodenough PLB 697 (2011) 412. Excess around the galactic centre ($\sim 10°$) at $(1 - 10)\,\text{GeV}$
  - Reanalysis (Fermi-LAT 2017 and Bartels et al. 2018) conclude that the signal is likely not originating from dark matter annihilations

- Other explanations: Protons from supernova remnants, electrons or ms pulsars

- In PRL 115 (2015) 231301, Fermi searches for dark matter at dwarf spheroidals $\rightarrow$ limits on $< \sigma_A v >$. Recent results from the galactic center (Fermi-LAT, Astrophys.J. 840 (2017) 43) have a sensitivity almost as good as the search in dwarf spheroidals

10.4.4. X-rays signals

- Goals of X-ray satellites: study star-forming regions, formation and evolution of galaxy clusters, study of supermassive black holes & searches for dark matter
- Detection energy range $\sim (0.1 - 10)\,\text{keV}$
- Measurements at satellites because the atmosphere would absorb this radiation
- Instruments: XMM-Newton, Chandra
- Detection principle: Wolter grazing mirrors (lenses or parabolic mirrors do not work to focus X-rays). The focussing happens only if the incident angle is very small (up to 2 degrees). Designed by Wolter in 1952, see figure 54.

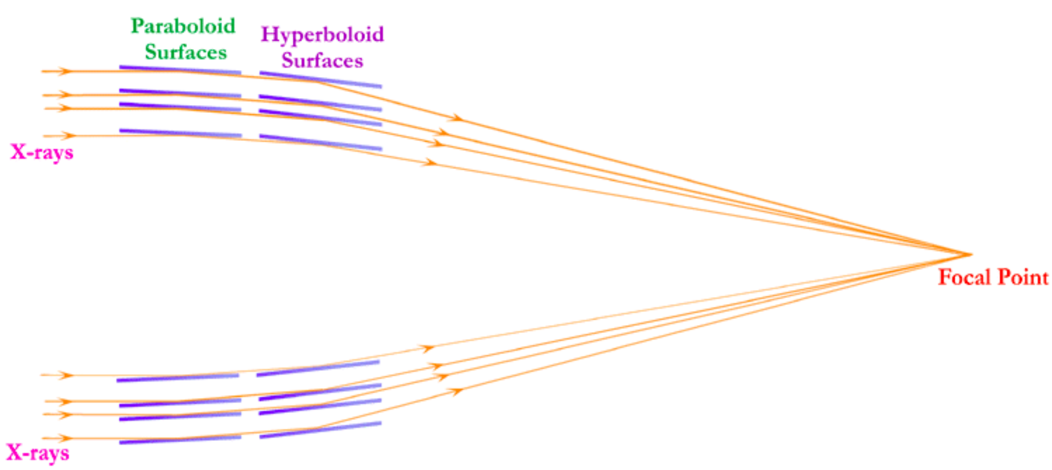

Figure 54. Schematic of grazing X-ray telescope. This cross section through four nested pairs of mirrors illustrating the principle of grazing incidence reflection and focussing of X-rays. Figure from Chandra homepage.

- Wolter telescopes can be used to search for DM signals in the $\sim$keV energy range
- Background from 'known' plasma emission lines (Al, Si, Fe, Ca, Ar, ..)

- The 3.5 keV line:
  - 2014: weak unidentified emission line at $\sim 3.5\,\text{keV}$ in the XMM-Newton and Chandra data of galaxy clusters (independently by E. Bulbul et al. 2014 and A. Boyarsky et al. 2014), see figure 55 (left)

   – Explanations: unknown plasma emission line (Jeltema & Profumo 2014 and arXiv:1511.06557), sterile neutrino decay or axion decay

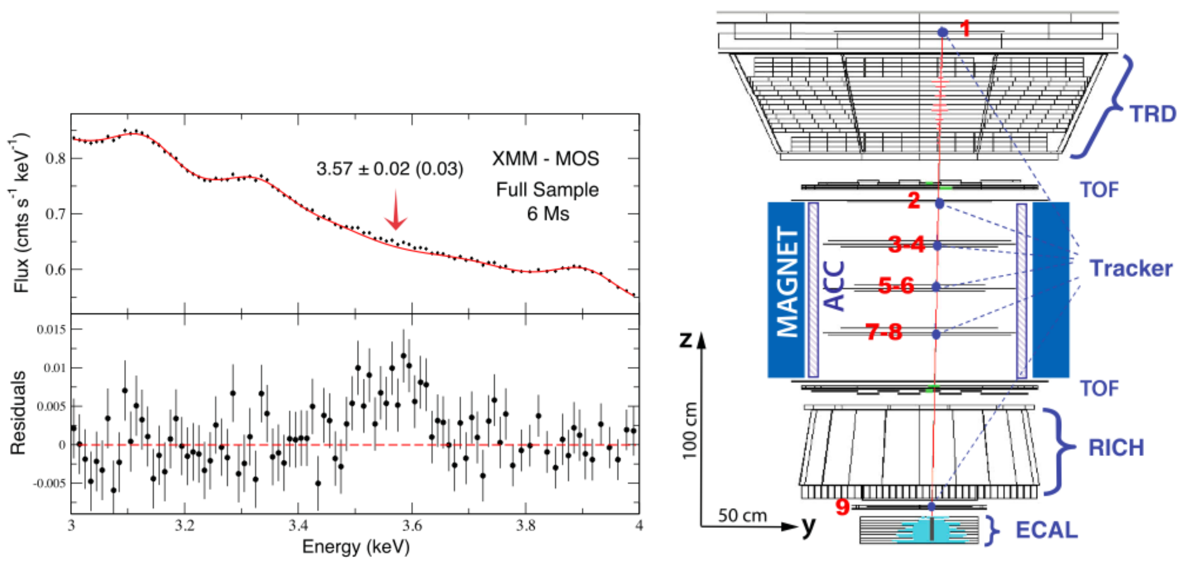

Figure 55. (Left) XMM-Newton data in the region $(3-4)$ keV stacking several galaxy clusters. Spectrum rebind to make the excess at ~ 3.57 keV more apparent. Figure from E. Bulbul *et al.*, ApJ **789** (2014) 13. (Right) Schematics of the AMS detector. Figure from the homepage.

10.4.5. Charged particles

- Mainly measuring e^-/e^+ and $p/\bar{p}$. No directionality because charged particles are deflected in magnetic fields
- Instruments: satellites as HEAT, CAPRICE, PAMELA, Fermi, AMS
- Since 2008, "positive results" in few experiments pointing to an excess at $\sim$TeV scale in the positron fraction $e^+/(e^+ + e^-)$

- **AMS detector** (see figure 55): Alpha Magnetic Spectrometer
- At the international space station (ISS) since 2011 with 8.5 tons 2 500 W power consumption
- Scientific goals: measurement of antimatter & dark matter

- Detector design: HE-physics type of detector (tested at CERN)
   – silicon tracker (9 planes)
   – transition radiation detector (particle identification)
   – Time of flight (4 planes)
   – Magnet

- Anticoincidence counter (to reject particles entering from the sides)
- Cherenkov detector
- Electromagnetic calorimeter (energy measurement)

- AMS has provided measurements of charged particles in the range
  - $(10-290)\,\mathrm{GeV}/c$ for e^+e^-
  - $(180-400)\,\mathrm{GeV}/c$ for protons
- It provides the most precise measurements of the positron fraction (see figure 56 (left))

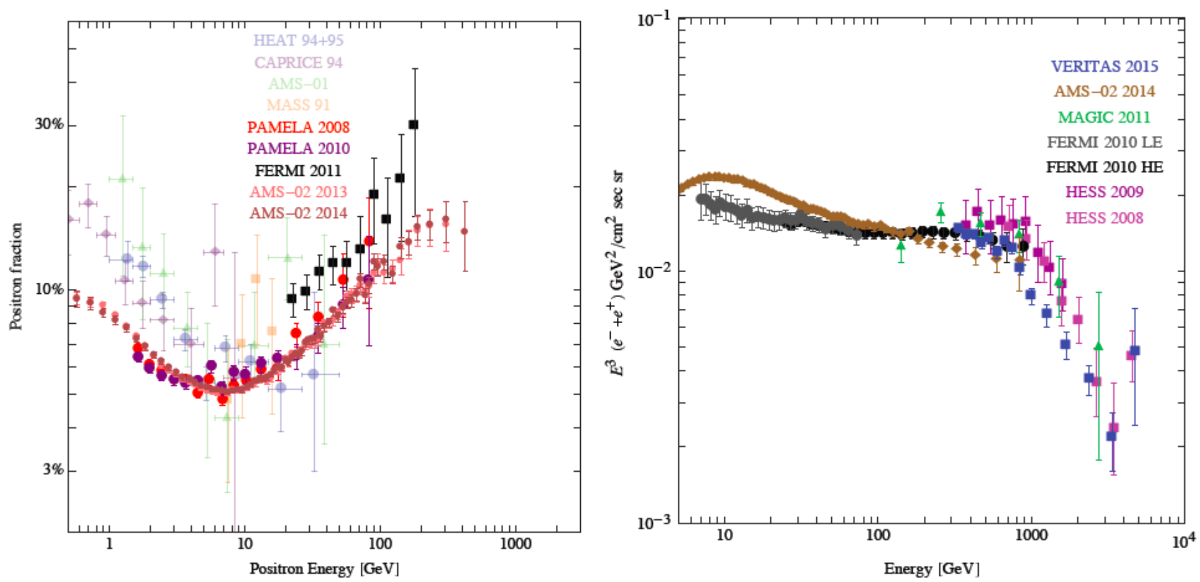

Figure 56. Compilation of data in charged cosmic rays: positron fraction (left) and sum of electrons and positrons (right). Figure from M. Cirelli (2015) arXiv:1511.02031.

- AMS, PRL 113 (2014) 121101: Below 8 GeV, the positron fraction decreases with increasing energy. This is expected from the diffuse production of positrons.
- Above 8 GeV, the fraction increases and this measurement is consistent with the observations of other experiments (besides normalization). This fraction is isotropic in the arrival direction.
- Explanations:
  - Astrophysical: e^+ from pulsers $\rightarrow$ would show a slow decrease of the rate with increasing energies and a dipole asisotropy
  - DM annihilation: should show a rapid decreasing of the rate with increasing energy (the steepness depends however on the annihilation channel). This DM hypothesis requires, however, a large annihilation rate into leptonic final channels. Constrains from the non-observation of other signals.

- Figure 57 shows a summary of the current (summer 2015) most stringent bounds on dark matter annihilation in different channels and from different searches.

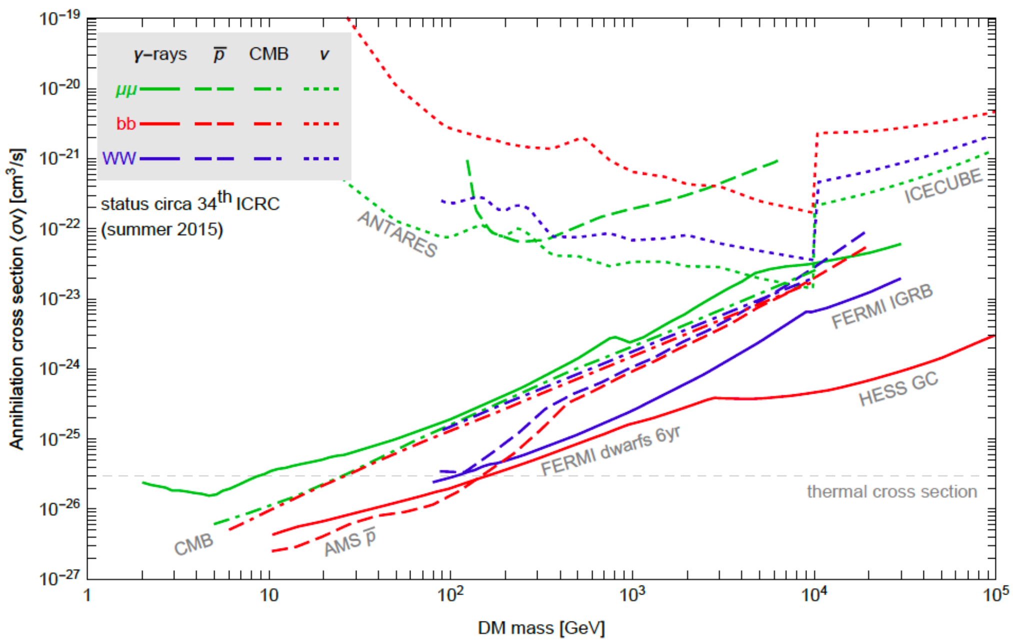

Figure 57. Summary figure of the current most stringent bounds on dark matter annihilation in different channels and from different searches. The data originates from AMS-02, Fermi, CMB, HESS, ANTARES and IceCube. Figure from M. Cirelli (2015) arXiv:1511.02031.

11. Dark matter searches at particle accelerators

11.1. Introduction

- From direct detection searches we learn about the dark matter particle mass and its cross section to ordinary matter
- From indirect detection we can learn also about the particle mass and its annihilation cross section
- To learn other particle properties or something about the theory behind, the production of dark matter particles at accelerators is the best method

11.2. Signatures and features

- Dark matter is neutral $\rightarrow$ after its production, it passes through the detector without being 'registered'
- Main feature: dark matter is reconstructed from missing energy in the events
- **Direct production**: in the collission pairs of dark matter particles are produced accompanied by a so-called mono-X signature: $pp \rightarrow \chi\overline{\chi} + x$ (see also [92])
- Mono-X could be a mono-γ, a monojet or mono- b,t,W,Z. In such events a hadronic jet (or a photon or a leptonically decaying Z or W boson ...) are produced with a large missing momentum
- Usually the direction transverse to the beam is taken as the total traverse momentum has to be balanced

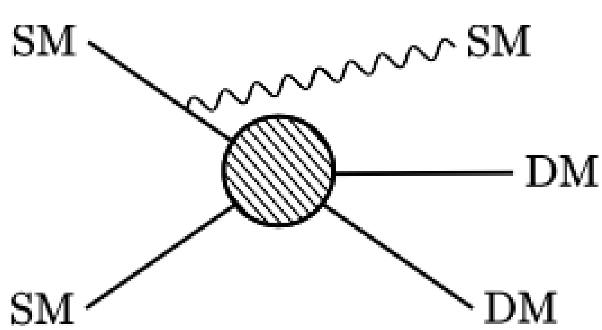

Figure 58. Illustration of the direct production of dark matter at LHC. Figure from [92]

- **Cascade events**: new particles are created in the collision and within the cascade decay of such particles, the DM particles are created. As direct production is significantly more clear signature, mainly this is consider in the analysis

- Example: SUSY search for R-parity conserving models. In these models the lightest particle is stable (LSP) and the event topology is a high jet multiplicity accompaniend by a large missing E_T
- **Z-decay width**: measurement at LEP, see next section and [93]

11.3. Detection at colliders

- Lepton (electron) colliders as LEP at CERN with clear collissions and no background from QCD
- Hadron colliders as Tevatron at Fermilab or LHC at CERN reaching to higher energies
- In all cases the detectors have 'onion-shaped' structure: several layers of different detectors in order to identify all produced particles and reconstruct their energies (see examples in figure 59)
- From the inside to the outside: inner tracker (often out of silicon pixel detectors), magnet systems of few Tesla strength, electromagnetic calorimeters, hadronic calorimeters, and in the outermost layer muon detectors
- All sub-detectors are calibrated separately in order to implements their response and efficiency in the detector Monte-Carlo simulation

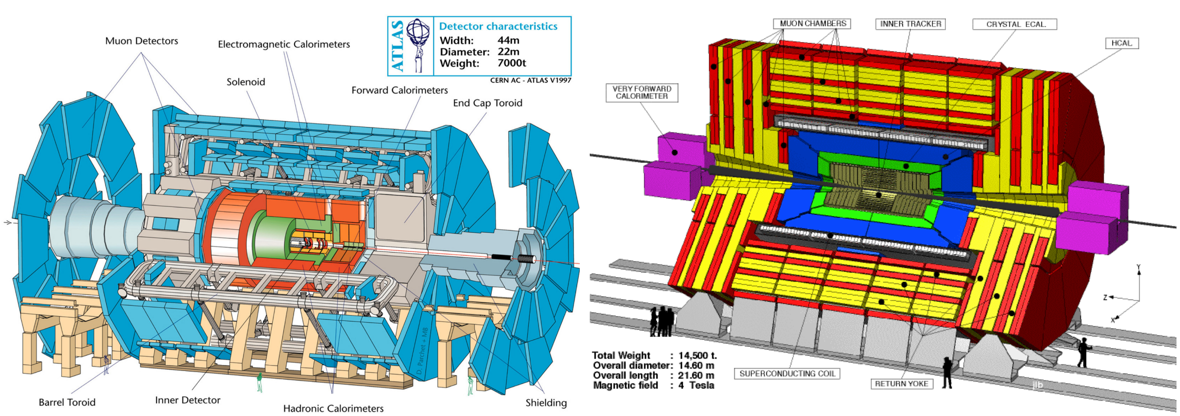

Figure 59. Schematic view of the Atlas (left) and the CMS (right) detectors. Figures from collaboration homepages.

11.4. Searches at LEP

- LEP → Lepton collider @ CERN from 1989 - 2000
- Detectors: Aleph, Delphi, L3 and OPAL
- The Z decay to invisible channels was studied, e.g. $Z \to \nu\overline{\nu}$, with $\Gamma_{invisible} = N_\nu \cdot \Gamma_\nu$

- The existence of further neutrinos or other particles coupling to Z would affect the width, see figure 60. The observed width favors $N_\nu = 3$

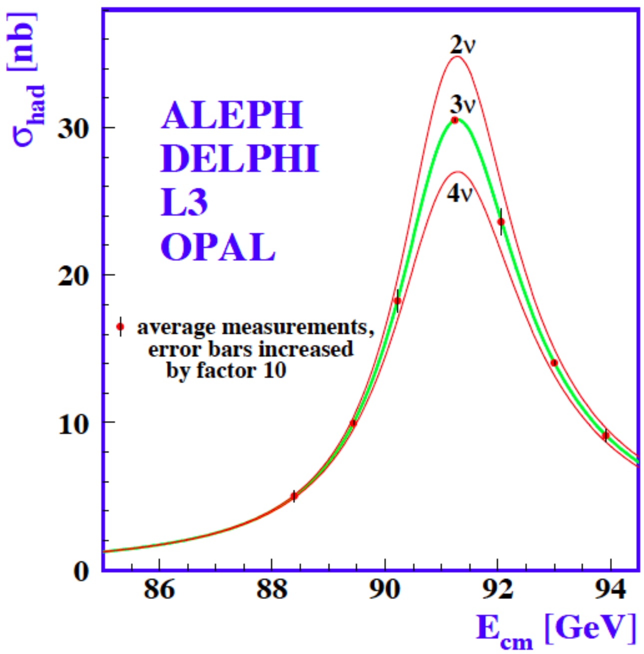

Figure 60. Measurements of the hadron production cross-section around the Z resonance. The lines represent the predicted cross-section for two, three and four neutrino species with SM coupling and negligible masses. Figure from ALEPH, DELPHI, L3 and SLD Collaborations, Phys. Rept. 427 (2006) 257 and arXiv:hep-ex/0509008 [93].

- LEP experiments also constrained the coupling of dark matter to electrons
- Additional assumptions are needed to set limits on DM-nucleon scattering (very model dependent)

11.5. Searches at LHC

- Golden search channel: mono-signatures. Other topologies are also searched for
- Recent result 'Search for new phenomena in final states with an energetic jet and large missing transverse momentum in pp collisions at $\sqrt{s} = 13\,\text{TeV}$ using the ATLAS detector, ATLAS Collaboration, PRD 94, 032005, 2016 or arXiv:1604.07773' is discussed
- New phenomena: models with extra spatial dimensions, Supersymmetry and WIMPs
- Signal signature: at least one jet with $p_T > 250\,\text{GeV}$ and no leptons involved. Events with leptons are used as control samples

- Background: dominated by $Z(\rightarrow \nu\nu)+$jets, $W+$jets and a small contribution from $Z(\rightarrow \ell^+\ell^-)+$jets (see figure 61)

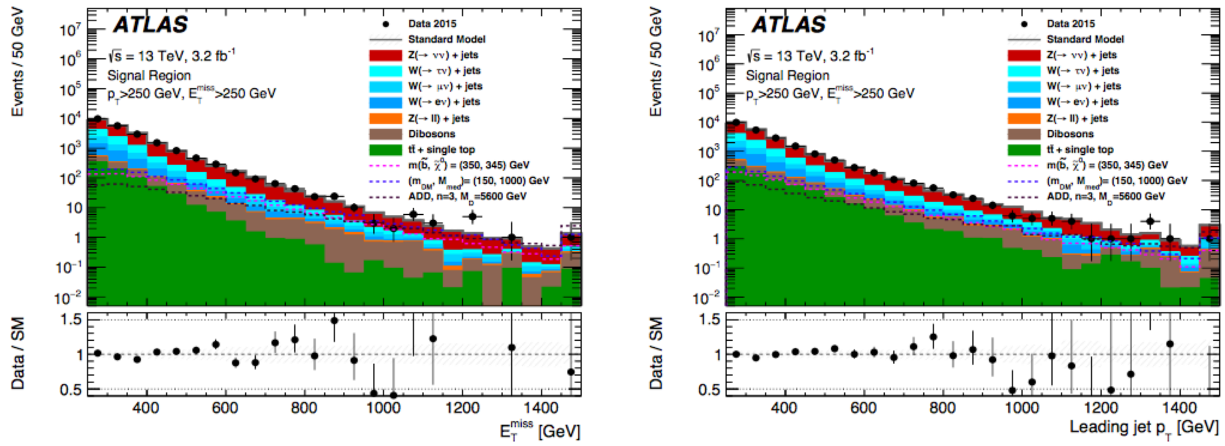

Figure 61. Measured distributions of E_T^{miss} and leading jet p_T for the lowest energy range considered in the analysis compared to the standard model expectations (coloured regions). For illustration, the distributions for different DM scenarios: extra dimensions, SUSY and WIMP, are also included (dashed lines). Figures from [94]

- Outgoing particles are propagated thought the full Geant4 detector simulation with includes efficiencies and geometrical effects. Control samples are used to verify the simulation on data
- Several uncertainties have to be consider for both background prediction and signal model
- Result: good agreement of the data with the standard model prediction $\rightarrow$ upper limits on the existence of new phenomena.
- The mapping of these results into the parameter space of direct (or indirect) detection is model dependent!
- Figure 62 shows on the left the result in the $\mathrm{m}_\chi - \mathrm{m}_A$ parameter space (axial-vector mediator assumed). The solid (dashed) curve shows the median of the observed (expected) limits while the band indicate the $\pm 1\sigma$ uncertainty.
- The right side of figure 62 shows the comparison to direct detection results for spin-dependent WIMP-proton scattering. The comparison is model dependent and solely valid in the context of this model, assuming minimal mediator width and the coupling values $\mathrm{g}_q = 1/4$ and $\mathrm{g}_\chi = 1$. For spin-dependent interactions the LHC results are most constraining for WIMP masses below $\sim 250\,\mathrm{GeV}$

- The comparison can be also made for spin independent interactions.
- Figure 63 shows a result from the CMS collaboration [95] for a vector mediator in comparison to direct detection results for the spin independent case.

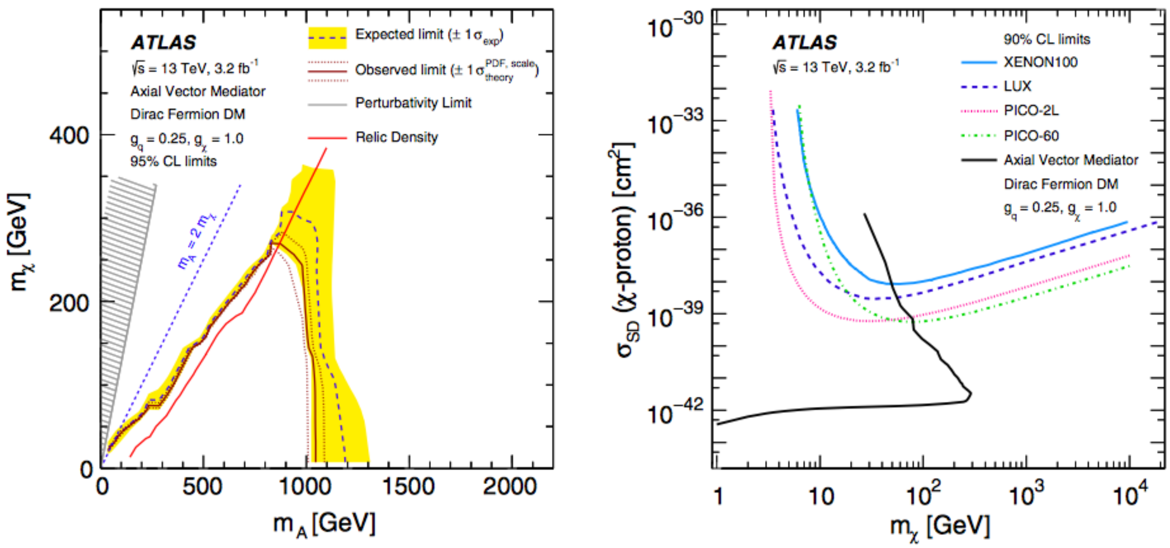

Figure 62. Left: Inferred 95% C.L. contours in the $m_\chi - m_A$ parameter plane. Right: a comparison of the inferred limits (at 90% C.L.) to the constraints from direct detection experiments on the spin-dependent WIMP-proton scattering cross section in the context of a simplified model with axial-vector couplings. Figures from ATLAS Collaboration, PRD 94, 032005, 2016 or arXiv:1604.07773 [94]

- In this case the collider results have most constraining results only below few GeV dark matter mass

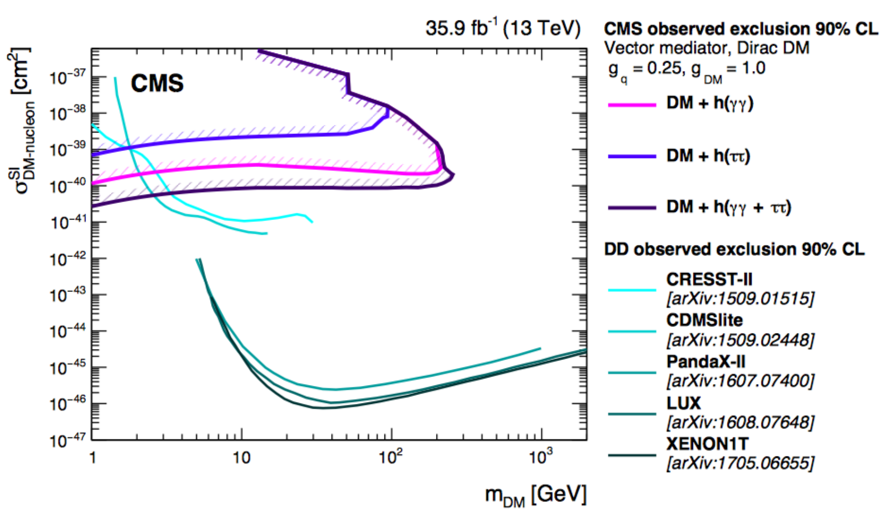

Figure 63. The 90% CL exclusion limits on the DM-nucleon SI scattering cross section as a function of m_{DM}. Results obtained in this analysis are compared with those from a selection of direct detection experiments. The latter exclude the regions above the curves. Figure from CMS [95]

11.6. Comparison to direct/indirect detection results

- Tevatron and LHC Run1 used contact interaction operators in EFTs to interpret their data. This is valid however only when the mass of the mediator is rather large (see also about the EFT validity here [92])
- In LHC Run2 instead simplified models (see [96] for instance) to interpret results

References

[1] F. Zwicky, "Die Rotverschiebung von extragalaktischen Nebeln," *Helvetica Physica Acta* **6** (1933) 110.

[2] V. C. Rubin, N. Thonnard, and J. Ford, W. K., "Extended rotation curves of high-luminosity spiral galaxies.," *Astrophys. J* **225** (1978) L107.

[3] A. Einstein, "Lens-Like Action of a Star by the Deviation of Light in the Gravitational Field," *Science* **84** (1936) 506.

[4] R. Massey, T. Kitching, and J. Richard, "The dark matter of gravitational lensing," *Rept. Prog. Phys.* **73** (2010) 086901, arXiv:1001.1739.

[5] D. Clowe, M. Bradac, A. H. Gonzalez, M. Markevitch, S. W. Randall, *et al.*, "A direct empirical proof of the existence of dark matter," *Astrophys. J.* **648** (2006) L109, arXiv:astro-ph/0608407.

[6] D. Harvey, R. Massey, T. Kitching, A. Taylor, and E. Tittley, "The non-gravitational interactions of dark matter in colliding galaxy clusters," *Science* **347** (2015) 1462, arXiv:1503.07675.

[7] V. Springel, C. S. Frenk, and S. D. White, "The large-scale structure of the Universe," *Nature* **440** (2006) 1137, arXiv:astro-ph/0604561.

[8] **Planck** Collaboration, N. Aghanim *et al.*, "Planck 2015 results. XI. CMB power spectra, likelihoods, and robustness of parameters," arXiv:1507.02704.

[9] **Planck** Collaboration, P. A. R. Ade *et al.*, "Planck 2015 results. XIII. Cosmological parameters," arXiv:1502.01589.

[10] J. Lesgourgues, "Cosmological Perturbations," in *Proceedings, Theoretical Advanced Study Institute in Elementary Particle Physics: Searching for New Physics at Small and Large Scales (TASI 2012): Boulder, Colorado, June 4-29, 2012*, pp. 29–97. 2013. arXiv:1302.4640.

[11] M. Milgrom, "A Modification of the Newtonian dynamics as a possible alternative to the hidden mass hypothesis," *Astrophys. J.* **270** (1983) 365.

[12] J. D. Bekenstein, "Relativistic gravitation theory for the MOND paradigm," *Phys. Rev.* **D70** (2004) 083509, arXiv:astro-ph/0403694.

[13] **MACHO** Collaboration, C. Alcock *et al.*, "The MACHO project: Microlensing results from 5.7 years of LMC observations," *Astrophys. J.* **542** (2000) 281, arXiv:astro-ph/0001272.

[14] B. Paczynski, "Gravitational microlensing by the galactic halo," *Astrophys. J.* **304** (1986) 1.

[15] B. Carr, F. Kuhnel, and M. Sandstad, "Primordial Black Holes as Dark Matter," *Phys. Rev.* **D94** no. 8, (2016) 083504, arXiv:1607.06077.

[16] S. D. White, C. Frenk, and M. Davis, "Clustering in a Neutrino Dominated Universe," *Astrophys. J.* **274** (1983) L1.

[17] S. Tremaine and J. E. Gunn, "Dynamical role of light neutral leptons in cosmology," *Phys. Rev. Lett.* **42** (1979) 407.

[18] L. Roszkowski, "Particle dark matter: A Theorist's perspective," *Pramana* **62** (2004) 389, arXiv:hep-ph/0404052.

[19] G. Gelmini and P. Gondolo, "DM Production Mechanisms," arXiv:1009.3690.

[20] G. Jungman, M. Kamionkowski, and K. Griest, "Supersymmetric dark matter," *Phys. Rept.* **267** (1996) 195, arXiv:hep-ph/9506380.

[21] V. Kuzmin and I. Tkachev, "Ultrahigh-energy cosmic rays, superheavy long living particles, and matter creation after inflation," *JETP Lett.* **68** (1998) 271, arXiv:hep-ph/9802304.
[22] R. Peccei and H. R. Quinn, "CP Conservation in the Presence of Instantons," *Phys. Rev. Lett.* **38** (1977) 1440.
[23] E. W. Kolb and M. S. Turner, "The Early Universe," *Front. Phys.* **69** (1990) 1.
[24] P. Gondolo and G. Gelmini, "Cosmic abundances of stable particles: Improved analysis," *Nucl. Phys.* **B360** (1991) 145.
[25] G. Arcadi, M. Dutra, P. Ghosh, M. Lindner, Y. Mambrini, M. Pierre, S. Profumo, and F. S. Queiroz, "The waning of the WIMP? A review of models, searches, and constraints," *Eur. Phys. J.* **C78** no. 3, (2018) 203, arXiv:1703.07364.
[26] T. Marrodán Undagoitia and L. Rauch, "Dark matter direct-detection experiments," *J. Phys.* **G43** no. 1, (2016) 013001, arXiv:1509.08767.
[27] J. F. Navarro, V. R. Eke, and C. S. Frenk, "The cores of dwarf galaxy halos," *Mon. Not. Roy. Astron. Soc.* **283** (1996) L72, arXiv:astro-ph/9610187.
[28] J. Diemand *et al.*, "Clumps and streams in the local dark matter distribution," *Nature* **454** (2008) 735, arXiv:0805.1244.
[29] V. Springel *et al.*, "The Aquarius Project: the subhalos of galactic halos," *Mon. Not. Roy. Astron. Soc.* **391** (2008) 1685, arXiv:0809.0898.
[30] J. Stadel, , *et al.*, "Quantifying the heart of darkness with GHALO - a multi-billion particle simulation of our galactic halo," *Mon. Not. Roy. Astron. Soc.* **398** (2009) L21, arXiv:0808.2981.
[31] M. Vogelsberger, A. Helmi, V. Springel, S. D. White, J. Wang, *et al.*, "Phase-space structure in the local dark matter distribution and its signature in direct detection experiments," *Mon. Not. Roy. Astron. Soc.* **395** (2009) 797, arXiv:0812.0362.
[32] A. M. Green, "Astrophysical uncertainties on direct detection experiments," *Mod. Phys. Lett.* **A27** (2012) 1230004, arXiv:1112.0524.
[33] J. Read, "The Local Dark Matter Density," *J. Phys.* **G41** (2014) 063101, arXiv:1404.1938.
[34] M. C. Smith *et al.*, "The RAVE Survey: Constraining the Local Galactic Escape Speed," *Mon. Not. Roy. Astron. Soc.* **379** (2007) 755, arXiv:astro-ph/0611671.
[35] J. Lewin and P. Smith, "Review of mathematics, numerical factors, and corrections for dark matter experiments based on elastic nuclear recoil," *Astropart. Phys.* **6** (1996) 87.
[36] A. Drukier, K. Freese, and D. Spergel, "Detecting Cold Dark Matter Candidates," *Phys. Rev.* **D33** (1986) 3495.
[37] K. Freese, M. Lisanti, and C. Savage, "Colloquium: Annual modulation of dark matter," *Rev. Mod. Phys.* **85** (2013) 1561, arXiv:1209.3339.
[38] D. N. Spergel, "The Motion of the Earth and the Detection of Weakly interacting massive particles," *Phys. Rev.* **D37** (1988) 1353.
[39] W. R. Leo, *Techniques for Nuclear and Particle Physics Experiments*. Springer-Verlag, Berlin, Heidelberg, Second revised edition, 1994.
[40] G. Heusser, "Low level counting from meteorites to neutrinos," *AIP Conf. Proc.* **785** (2005) 39.
[41] D. Mei and A. Hime, "Muon-induced background study for underground laboratories," *Phys. Rev.* **D73** (2006) 053004, arXiv:astro-ph/0512125.
[42] **XENON100** Collaboration, E. Aprile *et al.*, "The XENON100 Dark Matter Experiment," *Astropart. Phys.* **35** (2012) 573, arXiv:1107.2155.
[43] B. Cabrera, L. M. Krauss, and F. Wilczek, "Bolometric Detection of Neutrinos," *Phys. Rev. Lett.* **55** (1985) 25.
[44] D. Z. Freedman, "Coherent neutrino nucleus scattering as a probe of the weak neutral current," *Phys. Rev.* **D9** (1974) 1389.
[45] **COHERENT** Collaboration, D. Akimov *et al.*, "Observation of Coherent Elastic Neutrino-Nucleus Scattering," *Science* **357** no. 6356, (2017) 1123–1126, arXiv:1708.01294.
[46] L. E. Strigari, "Neutrino Coherent Scattering Rates at Direct Dark Matter Detectors," *New J.*

Phys. **11** (2009) 105011, arXiv:0903.3630.

[47] **EXO-200** Collaboration, J. Albert *et al.*, "Improved measurement of the $2\nu\beta\beta$ half-life of ^{136}Xe with the EXO-200 detector," *Phys. Rev.* **C89** (2014) 015502, arXiv:1306.6106.

[48] G. J. Feldman and R. D. Cousins, "A Unified approach to the classical statistical analysis of small signals," *Phys. Rev.* **D57** (1998) 3873, arXiv:physics/9711021.

[49] S. Yellin, "Finding an upper limit in the presence of unknown background," *Phys. Rev.* **D66** (2002) 032005, arXiv:physics/0203002.

[50] R. Bernabei *et al.*, "First Model Independent Results from DAMA/LIBRAPhase2," *Universe* **4** no. 11, (2018) 116, arXiv:1805.10486.

[51] **DAMA** Collaboration, R. Bernabei *et al.*, "First results from DAMA/LIBRA and the combined results with DAMA/NaI," *Eur. Phys. J.* **C56** (2008) 333, arXiv:0804.2741.

[52] K. Blum, "DAMA vs. the annually modulated muon background," arXiv:1110.0857.

[53] J. H. Davis, "Fitting the annual modulation in DAMA with neutrons from muons and neutrinos," *Phys. Rev .Lett.* **113** (2014) 081302, arXiv:1407.1052.

[54] J. P. Ralston, "One Model Explains DAMA/LIBRA, CoGENT, CDMS, and XENON," arXiv:1006.5255.

[55] **SuperCDMS** Collaboration, R. Agnese *et al.*, "Search for Low-Mass Weakly Interacting Massive Particles with SuperCDMS," *Phys. Rev. Lett.* **112** (2014) 241302, arXiv:1402.7137.

[56] **EDELWEISS** Collaboration, E. Armengaud *et al.*, "Constraints on low-mass WIMPs from the EDELWEISS-III dark matter search," *JCAP* **1605** no. 05, (2016) 019, arXiv:1603.05120.

[57] **CRESST** Collaboration, G. Angloher *et al.*, "Results on light dark matter particles with a low-threshold CRESST-II detector," arXiv:1509.01515.

[58] **DEAP** Collaboration, M. Boulay, "DEAP-3600 Dark Matter Search at SNOLAB," *J. Phys. Conf. Ser.* **375** (2012) 012027, arXiv:1203.0604.

[59] K. Abe *et al.*, "XMASS detector," *Nucl. Instrum .Meth.* **A716** (2013) 78, arXiv:1301.2815.

[60] **XENON** Collaboration, E. Aprile *et al.*, "Dark Matter Search Results from a One Ton-Year Exposure of XENON1T," *Phys. Rev. Lett.* **121** no. 11, (2018) 111302, arXiv:1805.12562.

[61] **PandaX-II** Collaboration, A. Tan *et al.*, "Dark Matter Results from First 98.7 Days of Data from the PandaX-II Experiment," *Phys. Rev. Lett.* **117** no. 12, (2016) 121303, arXiv:1607.07400.

[62] **LUX** Collaboration, D. S. Akerib *et al.*, "Results from a search for dark matter in the complete LUX exposure," *Phys. Rev. Lett.* **118** no. 2, (2017) 021303, arXiv:1608.07648.

[63] **DarkSide** Collaboration, P. Agnes *et al.*, "Low-Mass Dark Matter Search with the DarkSide-50 Experiment," *Phys. Rev. Lett.* **121** no. 8, (2018) 081307, arXiv:1802.06994.

[64] **COUPP** Collaboration, E. Behnke *et al.*, "Spin-Dependent WIMP Limits from a Bubble Chamber," *Science* **319** (2008) 933, arXiv:0804.2886.

[65] **PICO** Collaboration, C. Amole *et al.*, "Dark Matter Search Results from the PICO-60 C_3F_8 Bubble Chamber," arXiv:1702.07666.

[66] **DRIFT** Collaboration, J. Battat *et al.*, "First background-free limit from a directional dark matter experiment: results from a fully fiducialised DRIFT detector," arXiv:1410.7821.

[67] J. Abdallah *et al.*, "Simplified Models for Dark Matter Searches at the LHC," *Phys. Dark Univ.* **9-10** (2015) 8–23, arXiv:1506.03116 [hep-ph].

[68] M. Cirelli, N. Fornengo, and A. Strumia, "Minimal dark matter," *Nucl. Phys.* **B753** (2006) 178–194, arXiv:hep-ph/0512090 [hep-ph].

[69] M. Cirelli, A. Strumia, and M. Tamburini, "Cosmology and Astrophysics of Minimal Dark Matter," *Nucl. Phys.* **B787** (2007) 152–175, arXiv:0706.4071 [hep-ph].

[70] K. Griest and D. Seckel, "Three exceptions in the calculation of relic abundances," *Phys. Rev.* **D43** (1991) 3191–3203.

[71] S. P. Martin, "A Supersymmetry primer," arXiv:hep-ph/9709356 [hep-ph]. [Adv. Ser. Direct. High Energy Phys.18,1(1998)].

[72] M. Drewes *et al.*, "A White Paper on keV Sterile Neutrino Dark Matter," *JCAP* **1701** no. 01,

(2017) 025, arXiv:1602.04816 [hep-ph].

[73] S. Dodelson and L. M. Widrow, "Sterile-neutrinos as dark matter," *Phys. Rev. Lett.* **72** (1994) 17–20, arXiv:hep-ph/9303287 [hep-ph].

[74] X.-D. Shi and G. M. Fuller, "A New dark matter candidate: Nonthermal sterile neutrinos," *Phys. Rev. Lett.* **82** (1999) 2832–2835, arXiv:astro-ph/9810076 [astro-ph].

[75] A. Boyarsky, J. Lesgourgues, O. Ruchayskiy, and M. Viel, "Lyman-alpha constraints on warm and on warm-plus-cold dark matter models," *JCAP* **0905** (2009) 012, arXiv:0812.0010 [astro-ph].

[76] E. Bulbul, M. Markevitch, A. Foster, R. K. Smith, M. Loewenstein, and S. W. Randall, "Detection of An Unidentified Emission Line in the Stacked X-ray spectrum of Galaxy Clusters," *Astrophys. J.* **789** (2014) 13, arXiv:1402.2301 [astro-ph.CO].

[77] A. Boyarsky, O. Ruchayskiy, D. Iakubovskyi, and J. Franse, "Unidentified Line in X-Ray Spectra of the Andromeda Galaxy and Perseus Galaxy Cluster," *Phys. Rev. Lett.* **113** (2014) 251301, arXiv:1402.4119 [astro-ph.CO].

[78] A. Schneider, "Testing the sterile neutrino dark matter paradigm with astrophysical observations," *PoS* **NOW2016** (2017) 093, arXiv:1704.01832 [astro-ph.CO].

[79] G. Grilli di Cortona, E. Hardy, J. Pardo Vega, and G. Villadoro, "The QCD axion, precisely," *JHEP* **01** (2016) 034, arXiv:1511.02867 [hep-ph].

[80] **Particle Data Group** Collaboration, C. Patrignani *et al.*, "Review of Particle Physics," *Chin. Phys.* **C40** no. 10, (2016) 100001.

[81] A. Ringwald, "Alternative dark matter candidates: Axions," *PoS* **NOW2016** (2016) 081, arXiv:1612.08933.

[82] G. G. Raffelt, "Astrophysical axion bounds," *Lect. Notes Phys.* **741** (2008) 51, arXiv:hep-ph/0611350.

[83] **ADMX** Collaboration, N. Du *et al.*, "A Search for Invisible Axion Dark Matter with the Axion Dark Matter Experiment," *Phys. Rev. Lett.* **120** no. 15, (2018) 151301, arXiv:1804.05750.

[84] **PandaX** Collaboration, C. Fu *et al.*, "Limits on Axion Couplings from the First 80 Days of Data of the PandaX-II Experiment," *Phys. Rev. Lett.* **119** no. 18, (2017) 181806, arXiv:1707.07921.

[85] **CAST** Collaboration, V. Anastassopoulos *et al.*, "New CAST Limit on the Axion-Photon Interaction," *Nature Phys.* **13** (2017) 584, arXiv:1705.02290.

[86] P. W. Graham, I. G. Irastorza, S. K. Lamoreaux, A. Lindner, and K. A. van Bibber, "Experimental Searches for the Axion and Axion-Like Particles," *Ann. Rev. Nucl. Part. Sci.* **65** (2015) 485, arXiv:1602.00039.

[87] **ALPS** Collaboration, A. Spector, "ALPS II technical overview and status report," in *Proceedings, 12th Patras Workshop on Axions, WIMPs and WISPs (PATRAS 2016): Jeju Island, South Korea, June 20-24, 2016*, p. 133. 2017. arXiv:1611.05863.

[88] M. Cirelli, G. Corcella, A. Hektor, G. Hutsi, M. Kadastik, P. Panci, M. Raidal, F. Sala, and A. Strumia, "PPPC 4 DM ID: A Poor Particle Physicist Cookbook for Dark Matter Indirect Detection," *JCAP* **1103** (2011) 051, arXiv:1012.4515 [hep-ph]. [Erratum: JCAP1210,E01(2012)].

[89] P. Baratella, M. Cirelli, A. Hektor, J. Pata, M. Piibeleht, and A. Strumia, "PPPC 4 DMν: a Poor Particle Physicist Cookbook for Neutrinos from Dark Matter annihilations in the Sun," *JCAP* **1403** (2014) 053, arXiv:1312.6408 [hep-ph].

[90] **IceCube** Collaboration, M. G. Aartsen *et al.*, "IceCube Search for Dark Matter Annihilation in nearby Galaxies and Galaxy Clusters," *Phys. Rev.* **D88** (2013) 122001, arXiv:1307.3473.

[91] **Super-Kamiokande** Collaboration, K. Choi *et al.*, "Search for neutrinos from annihilation of captured low-mass dark matter particles in the Sun by Super-Kamiokande," *Phys. Rev. Lett.* **114** no. 14, (2015) 141301, arXiv:1503.04858.

[92] F. Kahlhoefer, "Review of LHC Dark Matter Searches," *Int. J. Mod. Phys.* **A32** no. 13, (2017) 1730006, arXiv:1702.02430.

[93] **ALEPH, DELPHI, L3, OPAL, SLD, LEP Electroweak Working Group, SLD Electroweak Group, SLD Heavy Flavour Group** Collaboration, S. Schael *et al.*, "Precision electroweak measurements on the Z resonance," *Phys. Rept.* **427** (2006) 257, arXiv:hep-ex/0509008.

[94] **ATLAS** Collaboration, M. Aaboud *et al.*, "Search for new phenomena in final states with an energetic jet and large missing transverse momentum in pp collisions at $\sqrt{s} = 13$TeV using the ATLAS detector," *Phys. Rev.* **D94** no. 3, (2016) 032005, arXiv:1604.07773.

[95] **CMS** Collaboration, A. M. Sirunyan *et al.*, "Search for dark matter produced in association with a Higgs boson decaying to $\gamma\gamma$ or $\tau^+\tau^-$ at $\sqrt{s} = 13$ TeV," *JHEP* **09** (2018) 046, arXiv:1806.04771.

[96] G. Busoni *et al.*, "Recommendations on presenting LHC searches for missing transverse energy signals using simplified s-channel models of dark matter," arXiv:1603.04156.